universität wien

MASTERARBEIT / MASTER'S THESIS

Titel der Masterarbeit / Title of the Master's Thesis

„Volume and Energy fluxes in the Arctic Ocean -

A comparison between an ocean reanalysis and in-situ observations“

verfasst von / submitted by

Marianne Pietschnig, BSc

angestrebter akademischer Grad / in partial fulfilment of the requirements for the degree of

Master of Science (MSc)

Wien, 2016 / Vienna 2016

Studienkennzahl lt. Studienblatt / degree programme code as it appears on the student record sheet:	A 066 299
Studienrichtung lt. Studienblatt / degree programme as it appears on the student record sheet:	Environmental Sciences
Betreut von / Supervisor:	Ao. Univ.-Prof. Mag. Dr. Leopold Haimberger

Preface

I hereby declare that I have written this master thesis myself using only the resources stated. Whenever a source is cited after the last full stop in a paragraph the citation concerns the whole paragraph (besides the other sources cited therein).

_____ _____

Place, Date Signature

Abstract

This thesis is a comparative study of oceanic heat and volume fluxes into the Arctic Ocean from September 2005 to August 2006. The purpose of this thesis is a comprehensive comparison of the Centro Euro-Mediterraneo sui Cambiamenti Climatici Global Ocean Reanalysis System Global Ocean Reanalysis System (C-GLORS, Version 5, Storto and Masina, 2016b) against observation-based estimates in the four major gateways connecting the Arctic to the Atlantic and Pacific Ocean. Once validated, the reanalysis product can be used for computing oceanic fluxes and their divergence for evaluating Arctic mass (or volume), energy and freshwater budgets and for validation of climate models.

In the course of this thesis reliable methods for comparing ocean reanalyses with observational data are developed. For one, the heat and volume fluxes calculated here are preferable over the fluxes derived during post-processing. Additionally, the choice of points on the model native grid in each gateway seems appropriate since the integrated fluxes and cross-section plots yield satisfactory results.

Overall, the C-GLORS ocean reanalysis performs quite well. However, significant discrepancies are found for the volume and heat transports across Davis Strait and the Barent Sea Opening. The flux patterns and transport estimates for Bering and Fram Strait agree better with observation-based estimates, but this is partly due to differences compensating each other. In this work, several regions which contribute to the differences in the flux estimates are identified in each strait. Based on a literature research, possible explanations for those differences are provided.

Zusammenfassung

Das Ziel der vorliegenden Masterarbeit ist die Validierung einer Ozeanreanalyse durch den Vergleich von arktischen Ozeanflüssen, die zum einen, im Rahmen dieser Arbeit, aus den Reanalysefeldern berechnet werden und zum anderen auf hydrographischen Messungen basieren. Betrachtet wird der zwölfmonatige Zeitraum zwischen September 2005 und August 2006, in dem die beobachtungsbasierten Daten derzeit verfügbar sind. Diese Masterarbeit ist Teil eines größeren Projekts zur Berechnung gekoppelter Energie-, Massen-, und Süßwasserhaushalte der Arktis. Ziel ist es, die einzelnen Komponenten der Haushaltsgleichungen aus aktuellen Reanalysen und anderen Datensätzen - wie etwa Satellitendaten - neu zu berechnen um die arktischen Budgets schließen zu können. Daher ist es wichtig zu erforschen, wie verlässlich die verwendeten Reanalyseprodukte, beziehungsweise wie groß die Unsicherheiten in den Haushaltstermen, sind.

Das Resultat dieser Arbeit ist, dass die Ozeanreanalyse (C-GLORS, Version 5) qualitativ gut mit den Beobachtungsdaten übereinstimmt. Am besten ist die Übereinstimmung in der Bering-, und Fram Straße obwohl sich hier teilweise Diskrepanzen gegenseitig kompensieren. In der Davis Straße und in der Öffnung zur Barents See stimmen die Volums-, und Energietransporte am schlechtesten mit den Schätzwerten der Beobachtungen überein. Im Rahmen dieser Masterarbeit ist es gelungen, die Regionen in jeder der Wasserstraßen zu identifizieren, in denen die Differenzen am größten sind und mögliche Gründe für diese Unterschiede zu finden.

Contents

List of Figures

List of Tables

Acronyms

ADCP = Accoustic Doppler Current Profiler

AG = ARCGATE

AMOC = Atlantic Meridional Overturning Circulation

ASOF = Arctic-Subarctic Ocean Fluxes

AVISO = Archiving, Validation and Interpretation of Satellite Oceanographic data

BIC = Bear Island Current

BSO = Barents Sea Opening

CAA = Canadian Arctic Archipelago

CERA = Coupled Earth Reanalysis system

CERES = Clouds and Earth Radiant Energy System

CG = C-GLORS

C-GLORS = CMCC Global Ocean Reanalysis System

CMCC = Centro Euro-Mediterraneo sui Cambiamenti Climatici

DAMOCLES = Developing Arctic Modelling and Observing Capabilities for Longterm Environment Studies

ECCO/GECCO = Estimating the Circulation & Climate of the Ocean / German ECCO

ECMWF = European Centre for Medium Range Weather Forecasts

EGC = East Greenland Current

ERA = European Reanalysis

ERA-CLIM = European Reanalysis of Global Climate Observations

ERA-Interim = European Reanalysis Interim

ERA 20C = European Reanalysis for the 20^th Century

ESA = European Space Agency

GCM = General Circulation Model

GODAS = Global Ocean Data Assimilation System

HAMSOM = Hamburg Shelf Ocean Model

IASOA = International Arctic Systems for Observing the Atmosphere

ICESat = Ice, Cloud and Elevation Satellite

IGY = International Geophysical Year

IPY = International Polar Year

JRA = Japanese Reanalysis

MIT = Massachusetts Institute of Technology

MOC = Meridional Overturning Circulation

NASA = National Aeronautics and Space Administration

NCAR = National Center for Atmospheric Research

NCEP = National Centers for Environmental Prediction

NCL = NCAR Command Language

NOAA = National Oceanic and Atmospheric Administration

NSF = U.S. National Science Foundation

NWP = Numerical Weather Predictions Model

OGCM = Ocean General Circulation Model

ORAS4 = Ocean Reanalysis System 4 (ECMWF)

RAPID = Rapid Climate-Change programme

RAPID-MOC = Rapid Climate Change - Meridional Overturning Circulation and Heatflux Array

SLA = Sea level anomaly

SONAR = Sound Navigation and Ranging

SSH = sea surface height

SSMIS = Special Sensor Microwave Imager/Sounder

TOA = Top of Atmosphere

VEINS = Variability of Exchanges in Northern Seas

WGS = West Greenland Shelf

WSC = West Spitzbergen Current

1 Introduction

The Arctic - formally defined as the region north of 66.5°N - plays a major role in the global climate system (Serreze and Barry, 2014, p. 23, p. 65): The Arctic acts as the main heat sink of the Northern Hemisphere since radiative energy loss in the polar region leads to strong temperature gradients in the atmosphere and ocean, which evoke northward energy fluxes in both domains (Serreze and Barry, 2014, p. 65).

Over the past few decades the Arctic has become the focus of numerous publications elucidating the adaptation of various components of the Arctic system to global climate change. The most prominent observed change is the anomalously low sea ice cover, especially at the end of the melt season in September (Stroeve et al., 2012; NSIDC, 2016), which has been declining at least since the 1970s (Serreze and Barry, 2014, pp. 19). Mean[1] sea ice thickness has decreased from a peak 3.64 m in the winter of 1980 (submarine measurements) to 1.89 m in 2008 (satellite record) (Kwok and Rothrock, 2009). Sea ice area reached a then-record low in the summer of 2007 ($3.6 \cdot 10^6$ km^2, Comiso et al., 2008) and decreased even further to $3.0 \cdot 10^6$ km^2 in summer 2012 (Parkinson and Comiso, 2013)). Global and Arctic upper and intermediate (0 - 700 m) ocean heat contents have been increasing since the 1970s (Rhein et al., 2013). Total ocean heat contents increased at similar rates at least during the 2000 to 2015 period (Mayer et al., 2016).

Surface air temperatures have been increasing since the middle of the 20^{th} century (Serreze and Barry, 2014, pp. 19). Atmospheric warming near the surface is more pronounced in the Arctic region compared to the global average temperature increase (Serreze et al., 2009). This so called "Arctic amplification" is attributable to the ice-albedo feedback: The Arctic atmosphere is heated due to the greenhouse effect, which means that more energy is available to melt Arctic sea ice. Due to the reduced ice cover, more ocean area (with low albedo) is exposed to incoming solar radiation for a longer period of time, which leads to further warming of the ocean. As a consequence, more heat is transferred from the ocean to the atmosphere - especially during fall - due to delayed ice formation, thus amplifying the initial disturbance of the system.

Observed freshening of the North Atlantic between 1965 and 1995 reported for example by Curry and Mauritzen (2005) is partly linked to higher freshwater exports from the Arctic Ocean in the form of liquid water and sea ice due to sea ice attrition, increased river

[1] Averaged over an irregularly shaped polygon covering about 38% of the area of the Arctic Ocean

runoff and excess precipitation (Peterson et al., 2006; Kwok, 2009). In the North Atlantic, cold and saline waters sink from the surface to the deep ocean (deep water formation) which is seen as a critical part of the Atlantic Meridional Overturning Circulation (AMOC) (Curry and Mauritzen, 2005). It has therefore been debated whether increased freshwater outflow from the Arctic Ocean could weaken the AMOC and modelling studies (e.g. Wadley and Bigg, 2002) suggest that the Arctic exports have the potential of altering the strength of the thermohaline circulation (Curry and Mauritzen, 2005; Beszczynska-Möller et al., 2011; Kwok, 2009). The mentioned mechanisms are just a few of many more reasons why research on and understanding of the Arctic climate system is of high importance especially in the context of global climate change.

1.1 Research Question and Motivation

The aim of this thesis is to compare mass and energy fluxes through the four major Arctic gateways - Davis, Fram and Bering Strait and the Barents Sea Opening (BSO) - from the recent "C-GLORS, Version 5" (Storto and Masina, 2016b) with the same fluxes derived from hydrographic observations of temperature, salinity and velocities in the four sections. These observation-based fluxes are currently being evaluated as part of the "ARCGATE" project (AWI, 2016) for the period 2004 to 2010 (Tsubouchi, 2014), and are at the time of writing already available from September 2005 to August 2006 (henceforth referred to as the "ARCGATE period"). C-GLORS, Version 5 data are available for the period 1979 to 2014 (Storto and Masina, 2016a). The ARCGATE project is the first effort to compile data from all mooring sites in these gateways, which, since 2004, allow monitoring of the complete Arctic Ocean boundary (Tsubouchi et al., 2012).

Such a comparison of reanalysis products against observations is an important tool for validating reanalyses, especially if those observations are not assimilated in the reanalysis (Masina et al., 2011). Finding independent observational data of temperature and salinity for assessing the skill of ocean reanalyses is challenging since most available datasets of adequate quality are incorporated into these analyses (Masina et al., 2011). In contrast, velocity measurements - and directly derived volume transports - are very useful for validation purposes, because they are usually not assimilated (Masina et al., 2011; Balmaseda et al., 2013). Temperature, salinity and velocity fields obtained from

the ARCGATE project represent a valuable source of largely independent[2] data. These can be used to validate reanalysis products such as C-GLORS[3] in the Arctic gateways. The underlying assumption with this method is that if the reanalysis product yields satisfactory results at the boundary, then the product is highly reliable for use in the entire Arctic Ocean.

An ocean reanalyses provides time series of the three-dimensional state of the ocean (Storto et al., 2016), whereas observational data are temporally and spatially limited especially in the Arctic Ocean (see Ch. 1.3). The fields from a reliable ocean reanalysis are valuable for investigating transports of freshwater and energy across the Arctic (Storto et al., 2016), as well as to derive various components of the Arctic energy and freshwater budgets. The latter describes the aim of the greater project which this thesis is part of (Haimberger, 2015).

A short remark on the definition of the research domain: In this thesis "the Arctic" refers to the ocean covered area of the North Pole which is enclosed by the "Arctic boundary" comprising the four major gateways connecting the Arctic Ocean to the Pacific (Bering Strait) and the Atlantic (Davis Strait, Fram Strait and the Barents Sea Opening) and the land masses in between (please refer to Ch. 2.2 for a detailed definition of the Arctic boundary).

1.2 Arctic Ocean Circulation

The following section is based on Beszczynska-Möller et al. (2011) and the other sources cited in the text.

The Arctic Ocean is connected to the Atlantic through Fram Strait, Davis Strait, the Barents Sea Opening and the Canadian Archipelago and to the Pacific Ocean through Bering Strait (see Fig. 1). Volume, heat and freshwater fluxes through those gateways are not homogeneously distributed within the straits and each of the gateways plays a unique role in modifying the state of the Arctic Ocean.

Fram Strait between Greenland and Svalbard is a deep and more than 600 km

[2]Velocity data are definitely independent as explained previously. Temperature and salinity date are believed to be independent in most regions based on www.metoffice.gov.uk/hadobs/en4 (accessed on 28 Oct. 2016)

[3]The algorithms developed during this thesis can then be used to validate other reanalysis products as well, as long as they are based on a similar model.

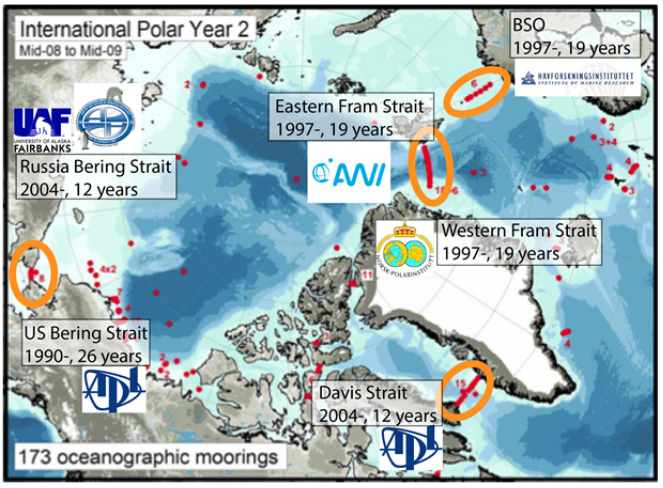

Figure 1: Map of the Arctic Ocean illustrating the locations of the four gateways also containing information on the length of permanently maintained moored observations (Tsubouchi, 2014, Fig. 1, reprinted with permission).

(Tsubouchi et al., 2012) wide gateway with a maximum depth of 2600 m in the central part of the strait. Warm waters enter the Arctic Ocean through the West Spitzbergen Current (WSC) in the eastern part of the strait. Cold water and sea ice leave the Arctic Ocean through the East Greenland Current (EGC) in the western part of deep Fram Strait. Half of the freshwater export from the Arctic Ocean to the Atlantic flows through Fram Strait with almost equal contributions from sea ice and liquid water (Serreze et al., 2006). The total volume flux through Fram Strait is - 2.0 $\pm$ 2.7 Sv[4] (1997 to 2007 average, Schauer et al., 2008) which includes - 8.7 $\pm$ 2.5 Sv export through the EGC (2002 - 2009 average, de Steur et al., 2014) and 6.6 $\pm$ 0.4 Sv import in the WSC (1997 - 2010 avg., Beszczynska-Möller et al., 2012). The net heat flux (1997 to 2009 average) is estimated to be 36 $\pm$ 6 TW[5] (Schauer and Beszczynska–Möller, 2009). In this thesis, positive volume and heat transport values signify net inflow into the Arctic, while negative values mean export.

The second pathway for warm Atlantic waters entering the Arctic Ocean is the **Barents Sea Opening (BSO)** between Svalbard and Norway. This strait is much shallower than Fram Strait with a maximum depth of 500 m and more than half of the strait not reaching deeper than 200 m. Nonetheless, due to its length of about 800 km (Tsubouchi et al., 2012) and net eastward flow, the volume import into the Arctic Ocean is large

[4] 1 Sv = 10^6 m^3/s
[5] 1 TW = 10^{12}W

(1997-2007 average of 2 Sv, Smedsrud et al., 2010). The average heat flux estimated for the same period is approximately 70 TW (Smedsrud et al., 2010) which keeps large areas of the Barents Sea ice free all year. Due to this absence of insulating sea ice about 90 % of the imported heat are lost to the atmosphere in the Barents Sea. Some of the initial inflow of 3.2 Sv is recirculated in the Barents Sea and exits the Arctic Ocean as 1.2 Sv of roughly 2° C colder water (Skagseth, 2008) through the northern part of the BSO (south of Bear Island) (Smedsrud et al., 2010).

Situated between Russia and the U.S. there is a narrow and shallow gateway called **Bering Strait** (max. depth = 50 m, width < 100 km) which represents the major pathway for oceanic freshwater transport into the Arctic Ocean. It is the only gateway to the Pacific. Bering Strait freshwater contributes roughly 30 % to the Arctic freshwater budget alongside non-oceanic imports from river discharge (38 %) and net precipitation (24 %) (Serreze et al., 2006). The fresher Pacific waters generally lie above the waters of Atlantic origin and therefore contribute to the upper ocean stratification in the Arctic. This stratification protects the sea ice from deeper warm waters in winter. However, in summer positive heat transport through this strait leads to significant sea ice melt (Woodgate et al., 2010). Interannual variability of Bering Strait heat flux is large due to the variability in volume transport and temperature (Woodgate et al., 2010). In 2007, when the Arctic sea ice cover was at a record low, as mentioned above, Bering Strait heat flux was exceptionally high - enough to explain 1/3 of that year's Arctic sea ice loss (Woodgate et al., 2010).

As discussed in Woodgate et al. (2005), volume transport through Bering Strait is driven on the one hand by a gradient between the Pacific and Arctic Ocean sea surface pressures which results in northward flow, and on the other hand by atmospheric pressure differences and local winds which are southwest- or westward on an annual mean basis, thus driving Bering Strait outflow. Neglecting the influence of winds on Bering Strait throughflow therefore results in a significant overestimation of volume imports (by about 20 %, Woodgate et al., 2005). The pressure gradient and local winds both show similar variability although on long (multiple months) and short (days to months) timescales, respectively (Woodgate et al., 2010). The total volume and heat fluxes through Bering Strait varied between 0.6 and 1.0 ± 0.1 Sv and 10 - 20 TW, respectively (1991 - 2007 estimates, Woodgate et al., 2010).

Besides freshwater export through western Fram Strait and import of saline waters through eastern Fram Strait and the BSO the **Canadian Arctic Archipelago (CAA)** represents the third freshwater sink for the Arctic Ocean (Serreze et al., 2006). Flow through the channels of the CAA are difficult to monitor due to prevailing sea ice, which poses a threat to submerged instruments, as well as strong currents. Fortunately, almost the entire flow ends up passing through **Davis Strait** along the east coast of Baffin Island, accounting for approximately half of the total freshwater export from the Arctic. Davis Strait is the last gateway connecting the Arctic to the Atlantic Ocean, with a maximum depth of about 1000 m and width of 320 km. On the East side of this wide strait in the West Greenland Shelf (WGS) region the West Greenland Current flows northward above the 100 m deep shelf transporting fresh water of Arctic origin. A bit further to the west the West Greenland Slope Current imports warm, saline water from the North Atlantic to the Arctic Ocean. Together with runoff and meltwater from Greenland and Baffin Island, these waters enter Baffin Bay, where they merge with the southward flowing Baffin Island Current.

Total volume (- 2.3 $\pm$ 0.7 Sv) and heat (20 $\pm$ 9 TW) fluxes through Davis Strait are estimated by Curry et al. (2011) based on one year of permanent moored observations between 2004 and 2005. Similar to Fram Strait and the channels of the CAA, Davis Strait is hydrodynamically wide meaning that in order to accurately estimate the net flux through the strait, the spatial resolution of observations has to be high enough to resolve small-scale eddies. As in the CAA, sea ice cover and icebergs pose big challenges for permanent monitoring of oceanic transports especially close to the surface.

1.3 Observational Data

1.3.1 History of Arctic Observation

The following section is summarised from Serreze and Barry (2014, p. 1-19) unless a different source is cited.

Exploration of the Arctic dates back to the 16^{th} century when the search for a direct sea route from northern Europe to China began. The knowledge gained through expeditions during the following centuries, which aimed at finding such a passage, laid the groundwork for geographical mapping of the Arctic region. Therefore, several features in the Arctic are named after the expedition leaders, for example Hudson Bay, Baffin Island and Baffin

Bay, the Laptev and Barents Sea, and of course Bering and Davis Strait. During those explorations, first meteorological and oceanographic observations of the Arctic polar cap were recorded, with regular reports commencing in the 1850s in most countries.

The First International Polar Year (IPY) in 1882-1883 marks the first time that coordinated expeditions to the Arctic were undertaken with the sole aim of making scientific observations . The First IPY also lead to the establishment of twelve stations scattered across the boundary of the polar cap (70°N) (Wood and Overland, 2016). The outcome of the First IPY are daily data of meteorological variables such as surface air temperature and sea level pressure (Wood and Overland, 2016). During 1932 to 1933 a Second IPY was launched in which roughly 70 more stations were established, but the Second World War resulted in many of the collected data being lost. After the war, the International Geophysical Year (IGY) was held in 1957/1958. The IGY represents one of the major milestones in the global observation of geophysical phenomena in the fields of oceanography, solar activity, meteorology, seismology, glaciology and many more (NAS, 2005). The first operational polar orbiters from 1979 onwards have been another key enhancement of the polar observing system.

1.3.2 Current Observation of the Arctic System

Since 1979 information on surface air pressure and temperature as well as sea ice drift in the central Arctic are available due to the International Arctic Buoy Program (Serreze and Barry, 2014, p. 16). Data from these buoys are sent to satellites and are therefore available in near-real time. Oceanographic data in the Arctic straits obtained from moored buoys, vessel-based measurements, seagliders and upward looking moored SONARS (Sound Navigation and Ranging) which measure ice drift and ice-keel depth are available nowadays due to several efforts such as the Arctic-Subarctic Ocean Fluxes (ASOF, established in 2000[6]) monitoring the fluxes into and out of the Arctic Ocean (Dickson, 2007; Serreze and Barry, 2014, p. 16).

Sea surface height (SSH) and sea level anomalies (SLA) obtained from satellite altimetry are made available through AVISO[7] (Archiving, Validation and Interpretation of Satellite Oceanographic data). Sea ice extent, thickness and velocity are measured by various instruments aboard satellites including the European Space Agency (ESA) CryoSat-2

[6] http://asof.awi.de, accessed on 29 Oct., 2016

[7] http://www.aviso.altimetry.fr/en/home.html, accessed on 29 Oct., 2016

(launched in 2010[8]) or the National Aeronautics and Space Administration (NASA) Ice, Cloud and Elevation Satellite ICESat (2003-2009) and ICESat-2 (launch date: 2017[9]). The advent of passive microwave sensors aboard NASA satellites in 1973 facilitated the monitoring of sea ice extent and concentration during the polar night and under cloudy conditions. The data obtained from the Special Sensor Microwave Imager/Sounder (SSMIS, Wentz et al., 2012) launched in 2005 combined with its precursors have provided daily fields of sea ice conditions for more than 30 years. (Serreze and Barry, 2014, p. 17 - 18)

The last IPY (2007 - 2009) focused on monitoring a full annual cycle of Arctic terrestrial, atmospheric, cryospheric and marine biogeochemical systems (Uttal and coauthors, 2016; Serreze and Barry, 2014, p. 18). The International Arctic Systems for Observing the Atmosphere (IASOA[10]) emerged from the IPY with improved instrumentation, aiming to further develop and coordinate monitoring of the Arctic atmosphere and to facilitate access to pan-Arctic observations (Uttal and coauthors, 2016). The observational network of IASOA consists of ten stations around the Arctic boundary with different instrumentation and scientific focus at each site. Long term monitoring of meteorological parameters, atmospheric composition (aerosols and greenhouses gases, stratospheric ozone, organic and inorganic pollutants), clouds, radiation and surface-atmosphere exchanges is conducted using in-situ and ground-based instruments, radiosondes and flux towers.

Moored Arrays

Oceanographic observation of the U.S. side of Bering Strait has been conducted by moored instruments since 1990, thus representing the longest available record of this kind of Arctic Ocean fluxes. Complete permanent observation of the strait is possible since the deployment of moorings on the Russian side in 2004 (see Beszczynska-Möller et al., 2011 and Fig. 1). High resolution moorings have been maintained in Bering Strait since 2007 as part of U.S. National Science Foundation (NSF[11]) efforts. Moorings were first deployed in Fram Strait and the Barents Sea Opening in 1997 as part of the VEINS (Variability of Exchanges in Northern Seas) project, subsequently under ASOF and DAMOCLES[12] projects

[8] www.esa.int, accessed on 29 Oct., 2016

[9] http://icesat.gsfc.nasa.gov/, accessed on 29 Oct., 2016

[10] http://www.esrl.noaa.gov/psd/iasoa/home2, accessed on 29 Oct., 2016

[11] https://www.nsf.gov/, accessed on 12 Nov., 2016

[12] http://www.damocles-eu.org/, accessed on 12 Nov., 2016

(Beszczynska-Möller et al., 2011). Monitoring of transports through Davis Strait has only been possible continuously since 2004 due to NSF funded programs. Several moorings are located within the Arctic boundary and in the sub-Arctic seas as well (Dickson, 2007, Fig. 29). Flow through the most important channels of the Canadian Arctic Archipelago - Nares Strait, Lancester Sound and Cardigan Strait/Hell Gate - which ultimately (almost entirely) passes through Davis Strait has been measured by moorings since 1998 (Beszczynska-Möller et al., 2011).

A mooring consists of a string attached to an anchor weight on one end and to a floating buoy on the other. Several instruments are attached to the string which measure conductivity (and thereby salinity), temperature and pressure (i.e. depth). In some cases, current meters or Acoustic Doppler Current Profilers (ADCPs) are added to the set of instruments for measuring velocities. One of the major challenges of permanent oceanographic observation of the Arctic Ocean is to obtain near-surface measurements since icebergs are potentially destructive for moored instruments in the upper ocean. Newer types of moorings have been developed which are automatically dragged deeper when currents increase so as to avoid collision with the sea ice. Another method - the ICECAT - is somewhat simpler: It consists of two instruments - one close to the surface and one at a safe depth - with the upper instrument transmitting its data to the lower instrument and the line being snatched in case the upper instrument gets destroyed by sea ice thus protecting the lower instrument and the data stored on it. A third method is to use autonomous seagliders. (Beszczynska-Möller et al., 2011)

Seagliders

Seagliders have been employed in Davis and Fram Strait to obtain high-resolution measurements of salinity and temperature which complement the less-densely located moorings. Seagliders are able to measure close to the ice-ocean interface. These instruments glide through the water column to a maximum depth of 1000 m taking CTD measurements[13] as well as measuring biochemical properties like dissolved oxygen or chlorophyll content. Seagliders stay deployed continuously for several weeks and find ice leads to surface and transmit the obtained data via satellite. (Beszczynska-Möller et al., 2011)

[13] CTD stands for Conductivity, Temperature and Depth and therefore means salinity, temperature and pressure measurements

1.4 Ocean and Atmospheric Reanalyses

Atmospheric and ocean reanalyses (or "retrospective analyses") are essential for studying the climate of the recent past and the assimilating models are similar to Numerical Weather Prediction models (Kalnay et al., 1996; Serreze and Barry, 2014, p. 304). Numerical Weather Prediction models (NWP) calculate short- or medium range weather forecasts for the time t_1 from an initial state of the atmosphere (at time t_0). The accuracy of the forecast atmospheric state is limited by the representation of the initial state of the atmosphere, as well as by model resolution, parametrizations and model physics. Therefore, the forecast is combined with observational data obtained at time t_1 and a new initial state is calculated for the next forecasting step (Serreze and Barry, 2014, p. 276, pp. 302). This process of combining model output and observational data - which are both subject to errors - to obtain an optimum representation of the atmospheric state is referred to as "data assimilation", with the output fields usually named "analyses" (Serreze and Barry, 2014, p. 291, p. 304). A distinct advantage of this method is that the model data can both be used to fill gaps in the observational data, thus increasing data coverage, as well as to calculate quantities which are not easily measured, such as surface fluxes (Serreze and Barry, 2014, p. 291, pp. 303).

Models and data assimilation schemes are constantly being improved in order to obtain better forecasts, therefore making archived data from operational models unsuitable for climate studies due to the occurrence of apparent "climate changes" (Kalnay et al., 1996). Reanalyses differ from operational NWPs in that they use fixed model versions and data assimilation schemes, thus reducing such false climate jumps. However, it is important to note that the amount and quality of assimilated data is nonetheless variable (Serreze and Barry, 2014, p.304). The pioneering atmospheric reanalysis product was developed by the National Centers for Environmental Prediction / National Center for Atmospheric Research (NCEP/NCAR) in 1991 (Kalnay et al., 1996), which is continuously being updated and has since been succeeded by several other reanalysis products including the European Centre for Medium Range Weather Forecasts (ECMWF) product ERA-Interim (Dee and coauthors, 2011) as well as the Japanese Reanalysis JRA-55 (Kobayashi et al., 2015). Most current atmospheric reanalyses cover the period from 1958 or 1979 until present due to the availability of high-quality observational data during more recent years. However, significant effort is being put into retrieving and quality controlling

early 20^{th} century in-situ observations and early satellite data in the currently ongoing international European Reanalysis of Global Climate Observations project coordinated by the ECMWF (ERA-CLIM2, ECMWF, 2016a).

Similar to atmospheric reanalyses, the main purpose of ocean reanalyses is to obtain the optimal representation of the three dimensional oceanic state at regular time intervals (Storto et al., 2016). Ocean reanalyses combine the output from OGCMs (Ocean General Circulation Models) with ocean observations and additionally use atmospheric reanalyses fields as forcing in an attempt to make up for the shortcomings of the ocean observation network (Storto et al., 2016). Current ocean reanalysis products include the CMCC product C-GLORS, Version 5 (Storto and Masina, 2016b), the ECMWF Ocean Reanalysis System ORAS4 (Balmaseda et al., 2013, soon to be followed by ORAS5), the ECCO (Estimating the Circulation & Climate of the Ocean, Forget et al., 2016) and German-ECCO (GECCO, Köhl and Stammer, 2008) products which are based on the Massachusets Insitute of Technology General Circulation Model (MITgcm[14]) as well as the NCEP effort GODAS (Global Ocean Data Assimilation System, Boyin et al., 2010) in association with the National Oceanic and Atmospheric Administration (NOAA). Most of these reanalyses provide fields of oceanic variables from 1979/1980 or later to near-present with few starting earlier (around 1958).

A common problem of using independent assimilation schemes for the atmosphere and ocean is that initial conditions at interfaces (in this case the ocean surface) tend to be inconsistent, which makes those fields unsuitable for initialising coupled atmosphere-ocean models. Therefore, the more recent years have seen increased efforts to produce coupled assimilation schemes, for example the ECMWF Coupled Earth Reanalysis system CERA (Laloyaux et al., 2014), in which observations close to the ocean surface affect both the atmosphere and the ocean for application to climate reanalyses and seasonal or even short-range predictions. (Laloyaux et al., 2016)

As already briefly mentioned in the beginning, one way of assessing the peformance and reliability of ocean reanalysis outputs is to compare certain quantities against (ideally independent) observations in various locations. Storto et al. (2016) for example compare the strength of the AMOC in the C-GLORS Version 4 reanalysis with observation-based estimates obtained from the Rapid Climate Change - Meridional Overturning Circulation

[14]http://mitgcm.org/, accessed on 12 Nov., 2016

and Heatflux Array (RAPID-MOC, Rayner et al., 2011) which monitors the MOC at 26.5°N through a combination of mooring - (measuring salinity and temperature profiles, as well as velocity in some areas) and satellite derived data. Additionally, the authors estimate volume, heat and freshwater transports for the period 1982 - 2012 for several sections across the world oceans and compare them to literature estimates. Similarly, Valdivieso et al. (2014) evaluate the University of Reading ocean reanalysis product (UR025.4, Zuo et al., 2013) by comparing zonal averages of heat and freshwater flux estimates with estimates based on independent hydrographic sections.

Another possibility is to compare different reanalysis products against each other, as done for example in the Ocean Reanalysis Intercomparison Project (ORA-IP, Balmaseda and coauthors, 2014). The aims of this and similar projects are to calculate ensemble means - for example of surface heat flux, sea level and sea ice thickness and extent - and assess the discrepancies between the analysis output fields, thereby quantifying the uncertainty of those means (Balmaseda and coauthors, 2014).

1.5 Coupled Arctic Mass Budget

Availability of flux measurements through the Arctic gateways and of reanalyses allows evaluation of the coupled mass and energy budgets of the Arctic. Here and in the following section, the "Arctic atmosphere" is the atmosphere overlying the Arctic Ocean, which is enclosed by the Arctic boundary $ArcWall$ (defined in the ocean by the locations of permanent moorings in the Arctic gateways, see detailed definition in Chapter 2.2) and the land masses in between. The mass budget of the entire Arctic atmosphere in integral form reads as

$$\frac{1}{g}\iint_{sfc}\frac{\partial p_s}{\partial t}dA = \frac{1}{g}\iint_{ArcWall_A} vdsdp + (E-P) \tag{1}$$

(Trenberth, 1997). The volume of the Arctic atmosphere ($ArcVol_A$, subscript A for atmosphere) is enclosed by the vertical boundary $ArcWall_A$ and the horizontal boundaries sfc (surface of the Arctic Ocean including sea ice) and TOA (top of atmosphere). Horizontal integration is with respect to ds, a length element of the Arctic boundary $ArcWall$. The component of the velocity perpendicular to $ArcWall$ is expressed by v (positive northward). The mass of an atmospheric column is equal to the pressure p_s at sfc scaled by

the gravitational acceleration g ($\frac{p_s}{g}$, Trenberth, 1997). This is due to the hydrostatic balance: For constant density with height, $p(z) = \rho g z$ (see also Eq. 17). Equation 1 expresses the fact that a net import of mass into the Arctic atmosphere either by horizontal transport (first term on right hand side) or by a net upward vertical flux (evaporation E, positive upward, exceeding precipitation P, positive downward) results in an increase of atmospheric mass.

For the liquid Arctic Ocean, the mass balance is expressed similarly by

$$\iiint_{ArcVol_O} \frac{\partial \rho_w}{\partial t} dV = \iint_{ArcWall_O} \rho_w v ds dz - (E - P - R - M) \tag{2}$$

(Bacon et al., 2015). Here, ρ_w is the density of the sea water. The mass of the entire Arctic Ocean (with volume $ArcVol_O$) increases if there is a net horizontal inflow of water through the oceanic boundary $ArcWall_O$, which is not balanced by a net upward surface mass flux. This surface flux is the difference between the upward flux E and the downward fluxes P, river runoff R and ice melt M. On the other hand, the fluxes on the right hand side are balanced under stationary conditions. In this form, the oceanic mass balance equation incorporates the sea ice mass balance.

1.6 Coupled Arctic Energy Budget

Turning now to the more complex energy budget of the Arctic, which is considered here to be split into three components: atmosphere, ocean and sea ice. The Arctic energy budget terms which appear in the equations of this chapter are illustrated in Figure 2. Atmospheric energy convergence into the Arctic (- $\nabla \bullet \mathbf{F_A}$) and the net radiative energy input at the TOA (Rad_{TOA} = incoming shortwave minus outgoing longwave radiation) contribute to changes in the atmospheric energy storage term $\partial A_E / \partial t$. Similarly, energy convergence in the ocean (- $\nabla \bullet \mathbf{F_O}$) and in the form of sea ice export ($\nabla \bullet \mathbf{F_I}$) contribute to $\partial O_E / \partial t$ and $\partial I_E / \partial t$, respectively. These three components are coupled by surface fluxes: Energy from the ocean is lost to the atmosphere in ice-free ocean areas in the form of $\mathrm{F}_S \cdot (1 - \mathrm{f}_{ice})$. Energy is also exchanged between sea ice and the atmosphere ($\mathrm{F}_S \cdot \mathrm{f}_{ice}$) and sea ice and the ocean ($\mathrm{F}_{IB} \cdot \mathrm{f}_{ice}$). The surface flux F_S (positive upward) is equal to

$$F_S = L \cdot E + H_S - Rad_{sfc} \tag{3}$$

(Trenberth, 1997). The latent heat of evaporation (or[15] sublimation) is denoted as L, H_S is the turbulent sensible heat flux at the ocean (or ice) surface and Rad_{sfc} is the net downward radiation through the surface. Technically, the sensible heat flux due to the net mass flux through the surface also contributes to F_S (Businger, 2014).

The energy balance in the atmosphere, ocean and sea ice can be summarized by

$$\frac{\partial A_E}{\partial t} = -\nabla \bullet \mathbf{F_A} + Rad_{TOA} + F_S \tag{4}$$

$$\frac{\partial O_E}{\partial t} = -\nabla \bullet \mathbf{F_O} - F_S \cdot (1 - f_{ice}) + F_{IB} \cdot f_{ice} \tag{5}$$

$$\frac{\partial I_E}{\partial t} = \nabla \bullet \mathbf{F_I} - F_{IB} \cdot f_{ice} - F_S \cdot f_{ice} \tag{6}$$

(Haimberger, 2015; Serreze and Barry, 2014, p. 72-74).

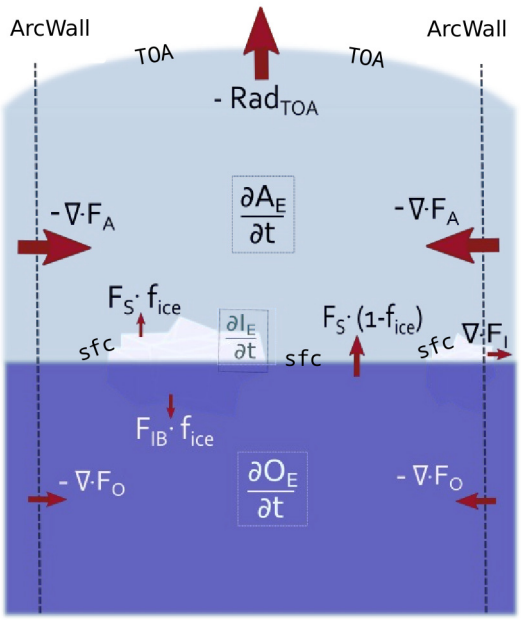

Figure 2: Illustration showing the atmospheric, oceanic and sea ice terms of the Arctic energy budget (adapted from Fig. 3.5 in Serreze and Barry, 2014, p.71 using equations from Haimberger, 2015).

[15] According to Peixoto and Oort (1992, p.308) the latent heat of evaporation $L_e = 2501\ J/g$ is the appropriate term to use in most situations.

Combining slightly different formulations from Peixoto and Oort (1992, p. 320, pp. 353), Trenberth (1997) and Mayer and Haimberger (2012) the energy budget for an atmospheric column (Eq. 7), integrated with respect to pressure p from the top of the atmosphere ($p = 0$) to the surface ($p = p_s$) can be expressed in more detail by

$$\frac{1}{g}\frac{\partial}{\partial t}\int_0^{p_s}(c_pT + k + Lq + \Phi_s)dp = -\frac{1}{g}\int_0^{p_s}[\nabla \bullet (c_pT + k + Lq + \Phi)\mathbf{v_2}]dp + Rad_{TOA} + F_S \quad (7)$$

where the term on the left hand side is the change in atmospheric energy storage $\partial A_E/\partial t$ caused by $\nabla \bullet \mathbf{F_A}$ with $\mathbf{v_2} = (u, v)$ denoting the horizontal wind vector, by Rad_{TOA} and by F_S. The atmospheric energy term (which is per unit mass in this case) consists of four parts: the internal energy (the product of the specific heat at constant pressure (c_p) with the temperature T), the kinetic energy $k = 1/2(u^2 + v^2)$ (which is negligible according to Peixoto and Oort (1992, p.320)), the product of L and specific humidity q, and the potential energy due to the geopotential Φ.

Integrating over the entire Arctic atmosphere and following the works of Peixoto and Oort (1992, pp.353) and Mayer et al. (2016) the equation for the atmospheric energy budget can be written as

$$\frac{1}{g}\iiint_{ArcVol_A}\frac{\partial A_E}{\partial t}dV_p = \frac{1}{g}\iint_{ArcWall_A}(c_pT + k + Lq + \Phi)vdsdp + Rad_{TOA} + F_S \quad (8)$$

Similar to the convention introduced in Chapter 1.5, v denotes the component of the horizontal velocity vector $\mathbf{v_2}$ (positive meaning into the Arctic domain). In this equation, $dV_p = dsdp$ symbolises integration with respect to pressure. Here Gauß' Theorem has been applied to the divergence term from Eq. 7. This theorem reads as

$$\iiint_{Vol}\nabla \bullet \mathbf{F}dV = \oiint_{A}\mathbf{F} \bullet \mathbf{n}dA \quad (9)$$

and states that the volume integral of the divergence of a flux $\mathbf{F}$ is equal to the area integral of the component of $\mathbf{F}$ perpendicular in each point to the area A (positive out of the volume), which completely encloses the volume Vol.

Similar to the atmospheric energy transport, the poleward transport of oceanic energy (without sea ice) across the boundary $ArcWall_O$ is equal to

$$\iint\limits_{ArcWall_O} \rho_w(c_w T + gz + c^2/2 + p/\rho_w) v ds dz \tag{10}$$

(Peixoto and Oort, 1992, p. 341). Neglecting the contribution from kinetic energy ($c^2/2$), assuming a constant density ρ_0 and using the hydrostatic pressure $p = \rho g z + p_0$ the second and fourth term in the integral almost cancel each other leaving only

$$\iint\limits_{ArcWall_O} \rho_w(c_w T) v dA + p_0 \iint\limits_{ArcWall_O} v dA. \tag{11}$$

The first term in this equation is the transport of heat and the second term is equal to zero if there is no net transport of mass into or out of the Arctic Ocean boundary $ArcWall_O$ (Peixoto and Oort, 1992, p. 341).

Applying the above simplifications, the energy budget for the entire Arctic Ocean including sea ice can be written as

$$\frac{\partial}{\partial t} \iiint\limits_{ArcVol_O} [T_w \rho_w c_w + \rho_i (T_i c_i - L_m)] dV = \iint\limits_{ArcWall_O} [\rho_w c_w T_w v_w + \rho_i v_i (c_i T_i - L_m)] ds dz - F_S \tag{12}$$

which is again a combination of previous formulations by Peixoto and Oort (1992, pp. 353), Trenberth and Fasullo (2008) and Haimberger (2015). The first term of this equation is the change of oceanic energy content including sea ice ($\partial(O_E + I_E)/\partial t$), where the energy content terms are approximated by heat content terms of the ocean water (subscript w) and sea ice (subscript i). The first term on the right hand side is the transport of energy by water (F_O) and sea ice (F_I) across the closed boundary $ArcWall_O$ of the Arctic Ocean volume $ArcVol_O$ which includes sea ice. L_m is the latent heat of melting (Peixoto and Oort, 1992, p. 348), v_w and v_i represent the velocity components of water and ice, respectively, which are orthogonal to $ArcWall_O$. More precisely, this "energy " transport occurs in the form of sensible heat for ocean water and latent (plus sensible) heat for sea ice (Peixoto and Oort, 1992, p. 356).

According to Schauer and Beszczynska–Möller (2009) the energy budget of the liquid Arctic Ocean should be written as

$$\frac{\partial}{\partial t} \iiint\limits_{ArcVol_O} (T - T_{ref}) \rho_w c_w dV = \oiint\limits_{ArcWall_O + sfc} [\rho_w c_w (T - T_{ref}) v_3] ds dz - F_S^* \tag{13}$$

This equation expresses the fact that a change in oceanic heat content can only be due to an imbalance between incoming and outgoing fluxes. The subscript in v_3 is used to symbolise that in this context, the velocity normal to the entire Arctic Ocean boundary ($ArcWall_O + sfc$) is meant and not just the horizontal transport. Therefore, F_S^* denotes the surface energy flux without the contribution from the volume flux through the surface. Without splitting up into boundary and surface fluxes and applying Gauß' Theorem the above equation can be rewritten as

$$\frac{\partial}{\partial t} \iiint\limits_{ArcVol_O} (T - T_{ref}) \rho_w c_w dV = - \iiint\limits_{ArcVol_O} \nabla \bullet [\rho_w c_w (T - T_{ref}) \mathbf{v_3}] dV - F_S^* \tag{14}$$

Setting ρ_w constant, splitting the divergence term up and taking advantage of the fact that T_{ref} is constant yields

$$\frac{\partial}{\partial t} \iiint\limits_{ArcVol_O} T dV = - \iiint\limits_{ArcVol_O} \mathbf{v_3} \bullet (\nabla T) dV - \iiint\limits_{ArcVol_O} T (\nabla \bullet \mathbf{v_3}) dV + T_{ref} \iiint\limits_{ArcVol_O} (\nabla \bullet \mathbf{v_3}) dV - \frac{F_S^*}{\rho_w c_w} \tag{15}$$

If there is no net transport of volume into or out of the Arctic Ocean (so when surface and oceanic fluxes cancel each other) $\iiint\limits_{ArcVol_O} (\nabla \bullet \mathbf{v_3}) dV$ disappears. In this case, the change in the heat content of the Arctic Ocean is independent of the choice of T_{ref}. Whenever integrating along a section or during a period of time where the net flux does *not* disappear, the choice of reference temperature (or temperature scale) as well as the volume flux "imbalance" determine the magnitude of the change in oceanic heat content or the heat flux through the considered cross section. Therefore, a comparison between absolute values of heat fluxes through partial sections is not possible unless the same T_{ref} is used in the calculations (Schauer and Beszczynska–Möller, 2009).

It should also be mentioned at this point that the oceanic energy equations are often formulated using the potential temperature (usually denoted by θ) (see for example Schauer and Beszczynska–Möller, 2009; Mayer et al., 2014; Bacon et al., 2015), whereas others use the in-situ temperature (T) (Trenberth and Fasullo, 2008; Peixoto and Oort, 1992, p. 341, pp. 353). The potential temperature is the temperature a fluid particle would have if it were brought from its pressure level p to a standard pressure level p_0 adiabatically (without the exchange of heat or matter) and it is related to the in-situ temperature T via

$$\theta(z) = T(z) - \int_{p_0}^{p(z)} (\frac{\partial T}{\partial p})_{ad} dp \tag{16}$$

(Peixoto and Oort, 1992, p. 55; Kundu et al., 2012, p. 20). To be in accordance with the more recent literature the potential temperature will be used for the comparisons and a reference temperature of $\theta_{ref} = 0°$ C is chosen. The difference between using θ and T is checked by calculating the heat transport through each of the Arctic gateways and the net flux exemplary for the year 2005. The net flux average is 130 $\pm$ 40 TW for that year both for the θ and T - based calculations, with a root mean square error (RMSD) of 0.4 TW or 0.3% between the two. The RMSD is less than 2% for all straits.

Schauer and Beszczynska–Möller (2009) state that it is wrong to define the "heat flux" through a cross section like Fram Strait where the volume is not conserved. However, the focus of this work is on identifying differences between two datasets and therefore the terms "heat flux" and "heat transport" will be used throughout even though this may be somewhat misleading in a more general context. Taking the above into consideration, differences in the heat fluxes between C-GLORS and ARCGATE can be due to differences in the deviation of θ from θ_{ref} or due to differences in the volume fluxes, so that disagreement in the monthly heat fluxes will be difficult to interpret. Therefore, in order to keep misinterpretations to a minimum, the potential temperatures will be referenced to $\theta_{ref} = 0°$ C for both C-GLORS and ARCGATE.

1.7 Arctic Seasonal Cycle

The following chapter is summarised from Serreze and Barry (2014, p. 76 - 84) who discuss the seasonal cycle of the various components of the Arctic energy budget terms based on an earlier work by Serreze et al. (2007). In this earlier work the atmospheric budget components are calculated from two atmospheric reanalysis products (ERA-40, Uppala and coauthors, 2005 and NCEP/NCAR, see Ch. 1.4) and from satellite data (Clouds and Earth Radiant Energy System, CERES[16]). Oceanic energy storage change is derived from a hydrographic climatology data set (PHC, 2005), sea ice export through Fram Strait is taken from Vinje et al. (1998) and oceanic heat convergence is estimated based on model output from the global Parallel Ice-Ocean Model POIM (Zhang and Rothrock,

[16] https://ceres.larc.nasa.gov/, accessed on 13 Nov., 2016

2003). Quantifications of atmospheric budget terms in this chapter are derived from Tab. 1 in Serreze et al. (2007) and are for the polar cap (north of 70°N). Oceanic budget terms are calculated from Tab. 2 (Serreze et al., 2007) and are for the "Arctic Ocean domain" (similar to the definition of the Arctic adopted in this thesis except that in this case the boundary is defined by the northern border of the Canadian Archipelago and not by Davis Strait). Absolute values are not as important in this section as a general overview of the annual changes in the Arctic energy budget terms. "Uncertainties" represent the standard deviation of monthly means from the respective period average.

Serreze et al. (2007) report that the atmospheric energy storage change is close to zero when considering the annual mean but detect considerable variation on an intra-annual basis, with values increasing from - 27 W/m^2 in September to a maximum of 25 W/m^2 in April. This seasonal cycle is driven by the changing solar flux. During most of the year there is a net loss of radiative energy from the Arctic atmosphere to space of - 168 $\pm$ 16 W/m^2 (monthly average from September to March) with the exception of June and July, when there is a small (23 and 11 W/m^2, respectively) input of radiative energy at the TOA. Most of this loss of energy is compensated by the atmospheric transport of energy from the lower latitudes into the north polar regions, with - $\nabla \bullet \mathbf{F_A}$ being large throughout the year (monthly average for Sept. - Mar. = 109 $\pm$ 3 W/m^2 with a minimum of 66 W/m^2 in May). Additionally, the atmosphere is heated by the Arctic Ocean in the form of sensible heat and through the formation of sea ice, which releases latent heat to the atmosphere and ocean during winter. The surface flux remains positive from September to April, with a monthly average of 43 $\pm$ 16 W/m^2 during this period and a minimum in July (- 85 W/m^2). The oceanic heat content thus decreases throughout all seasons except for the summer months May to August, when the surface flux turns negative so that a substantial amount of energy is transferred from the atmosphere to ocean and sea ice with the ice melt peaking in July. Unlike the atmosphere, the ocean only transports a small amount of energy from the lower latitudes into the Arctic Ocean domain with an annual mean of 2.75 $\pm$ 0.45 W/m^2.

Now having described the state of the Arctic energy budget, the remaining part of the thesis focuses on the performance of the ocean reanalysis (C-GLORS, Version 5) in order to evaluate its potential for deriving oceanic energy budget terms. In Chapter 2 the two datasets and the methods developed in this work are presented, followed by the results

and their discussion in Chapter 3. In the last chapter the findings are summarised and ideas for future research are proposed.

2 Methods and Data

2.1 C-GLORS

The CMCC Global Ocean Reanalysis System C-GLORS is based on the NEMO ocean model, version 3.2.1 (Madec, 2016) in its ORCA025 configuration (Storto et al., 2016). "025" refers to the coarsest resolution of 1/4° at the equator (equivalent to approximately 30 km grid spacing) with resolution increasing towards higher latitudes (roughly 10 km in the Arctic) (Barnier et al., 2006). The model native grid is tripolar, which means that there are three poles - one on the geographical South Pole and two in the Northern Hemisphere in Canada and Siberia (Barnier et al., 2006; Bacon et al., 2015). The reason for using three poles, which are all located on land, instead of two is that this way there are no poles located on the ocean domain. Otherwise there would be numerical difficulties when running an ocean model due to the singularity at the North Pole (Murray, 1996). The new model grid is still a regular spherical latitude/longitude grid from 90°S to 20°N, but north of this latitude the grid circles are progressively turned into ellipses oriented along the line connecting the two north poles (Barnier et al., 2006; Murray, 1996).

This construction results in a curvilinear, orthogonal grid meaning that the grid lines are bent so that zonal gridlines intersect meridional lines perpendicularly (Madec and Imbard, 1996; Madec, 2016, pp. 297). An additional constraint in the grid construction is that the zonal and meridional spacing should be equal to each other wherever possible (Madec, 2016, pp. 297). The resulting grid has 1442 "longitudes" and 1021 "latitudes", with the grid being irregular so that holding the "latitude" index (j) constant and varying the "longitude" index (i) does not follow a geographical latitude. There are 50 vertical levels with highest resolution in the upper ocean and increasing level thickness with depth (Storto et al., 2016; Barnier et al., 2006).

The ocean model NEMO uses the hydrostatic and Boussinesq approximations to solve the equations governing fluid flows. Due to the latter, the density is set constant everywhere in the governing equations except when the density is multiplied by the gravitational acceleration g (Bacon et al., 2015; Kundu et al., 2012, p. 135). Therefore, the density is not constant in the hydrostatic equation (Eq. 17), which states that the pressure at a certain depth z (with the z-axis positive downward) results only from the weight of the water column above it plus the atmospheric pressure at the sea surface p_0 (Bacon et al.,

2015; Kundu et al., 2012, p. 11).

$$p(z) = p_0 + \rho g z \tag{17}$$

Due to the Boussinesq approximation the continuity equation - or conservation of mass - (Eq. 18) reduces to the incompressibility equation (Eq. 19) because the material derivative of ρ becomes zero (Kundu et al., 2012, p. 98, p. 135). This means that the ocean model actually conserves volume instead of mass (Bacon et al., 2015).

$$\frac{1}{\rho}\frac{D\rho}{Dt} + \nabla \bullet u = 0 \tag{18}$$

$$\nabla \bullet u = 0 \tag{19}$$

In C-GLORS, the ocean model NEMO is coupled to the Louvain-La-Neuve Version 2 sea ice model (LIM2, Fichefet and Morales Maqueda, 1997; Bouillon et al., 2009). In-situ observations of temperature and salinity are taken from the Met Office EN3v2a dataset (Ingleby and Huddleston, 2007) before 2012 and from the EN4 (Good et al., 2013) dataset afterwards (Storto and Masina, 2016a). Satellite derived sea level anomalies (SLA) are taken from the AVISO dataset (Storto and Masina, 2016a). The objective of the data assimilation scheme is to minimize the difference between the observed state of the ocean and the background or "first guess" (ECMWF, 2016b). For computing the first guess the ocean model is forced with atmospheric fields of heat, momentum and freshwater fluxes (ECMWF, 2016b). In the case of C-GLORS atmospheric forcing fields are taken from the ERA-Interim reanalysis, the data assimilation window is seven days with the analysis being performed every seven days as well (Storto et al., 2016).

Scalar quantities such as temperature, salinity, or SSH and vector variables like meridional and zonal velocity and vorticity in the NEMO model are arranged on a "staggered" grid which is adapted for three dimensional application from the Arakawa C grid (Madec, 2016, pp. 297). "Staggered" means that the variables are not calculated in the same positions on one grid but on several separate grids which are shifted relative to each other by half a grid cell (Collins et al., 2013, p. 117 - 119). A schematic of the staggered grid can be found in Figure 10 showing the four different grids - T for the scalar properties (T, S, SSH and so on), u for zonal and v for meridional velocity and related transports (for example meridional or zonal heat transport) and the f-grid for vorticity. Therefore

special attention needs to be drawn to using the correct fields of depth or vertical level thickness vectors (d and dz, respectively) as well as the correct horizontal grid lengths (dx and dy) and geographical coordinates when using these different grids.

The output fields are interpolated from the model native tripolar grid to a regular latitude/longitude grid. While handling of the fields is easier on the interpolated grid, the interpretation of results becomes more difficult since it is not clear whether unexpected features for example in heat transport fields are attributable to the interpolation scheme or to the reanalysis itself. The substantial differences between using the interpolated fields versus the fields on the tripolar grid is shown and discussed in Chapter 2.3.1, Figs. 6 and 7.

2.2 ARCGATE

The ARCGATE project aims at calculating Arctic Ocean surface fluxes from oceanic volume, heat and freshwater transports through the four main Arctic gateways for the period 2004-2010 (Tsubouchi et al., 2016; AWI, 2016). The oceanic fluxes are calculated based on in-situ observations from moored instruments in those gateways. These moored observations of temperature, salinity and velocity have only been available permanently in all straits since 2004. The method of computing oceanic fluxes from the output of this observation network is explained in detail in Tsubouchi et al. (2012). The approach is to treat the Arctic Ocean as a box which is enclosed on its sides by the "Arctic boundary" - a combination of land masses (Greenland, Eurasia, North America and Svalbard) and the four major gateways connecting the Arctic Ocean to the world oceans (see Fig. 1):
Near-longitudinal sections:

- Davis Strait - West Coast of Greenland to the Canadian Baffin Island (66.66 - 67.31°N, 61.23 - 53.99°W)
- Fram Strait - East Coast of Greenland to Svalbard (78.82 - 78.84°N, 20.59°W - 11.61°E)
- Bering Strait - Alaska to Siberia (65.99 - 65.71°N, 170.07 - 168.07°W)

Near-latitudinal section:

- Barent Sea Opening - going south from Svalbard to Norway (77.46 - 69.75°N, 18.09 - 20.43°E)

There is one tiny gap in this vertical Arctic boundary, namely Fury and Hecla Strait in the Canadian Achipelago. These straits are not included in the box model directly, but the transports estimated from a six-week measurement period during spring 1972 are added to the overall uncertainty of the flux estimates. The top of the box is the ocean surface (or the upper surface of sea ice (Tsubouchi et al., 2016)) which allows the exchange of heat and freshwater in the form of precipitation, evaporation and runoff. The bottom of the box is the impermeable[17] seabed. In this Arctic Ocean box Tsubouchi et al. (2012) assume stationarity of salinity-anomaly and volume which means that no storage of freshwater or volume is permitted.

The locations of the moored instruments in each strait are shown in Figure 3. There are 41 mooring sites with a total of 138 instruments each observing one or more of the following variables: temperature (T), salinity (S) and velocity (v) (Tsubouchi et al., 2016). In the BSO, data from nine full-depth hydrographic sections between August 2005 and October 2006 are combined with velocity measurements at the bottom. The lack of moorings on Bjørnøya Bank - which lies between Svalbard and Bear Island - is partly compensated by adding vessel-based hydrographic data which are obtained nearly monthly between August 2005 and October 2006. Additionally, output from the NEMO model in its 1/12° resolution are added to the data in this area, as well as in the shallow, western part of Fram Strait (Belgica Bank) and above the shallowest instruments (located between 50 and 100 m depth) in all straits. The model data in this case are available to Tsubouchi et al. (2016) at 5-day resolution with 75 vertical levels. The in-situ observational data are projected onto the model grid and a common temporal resolution is established.

The entire cross section of each strait is filled with data by a combination of linear vertical and horizontal interpolation with slightly different methods applied for each parameter in the individual straits. In Davis Strait for example, velocities are interpolated from the velocity measured by the deepest instrument at 500 m to zero velocity at the bottom and temperatures and salinities below this depth are set constant to the deepest measured values. In Fram Strait where salinity measurements are sparse, the data from two full depth and six upper-ocean salinity profiles are interpolated horizontally. Generally, the method to fill the entire grid with data is to interpolate horizontally at the

[17] According to Peixoto and Oort (1992, p. 356) geothermal heating is usually negligible in the Arctic polar cap.

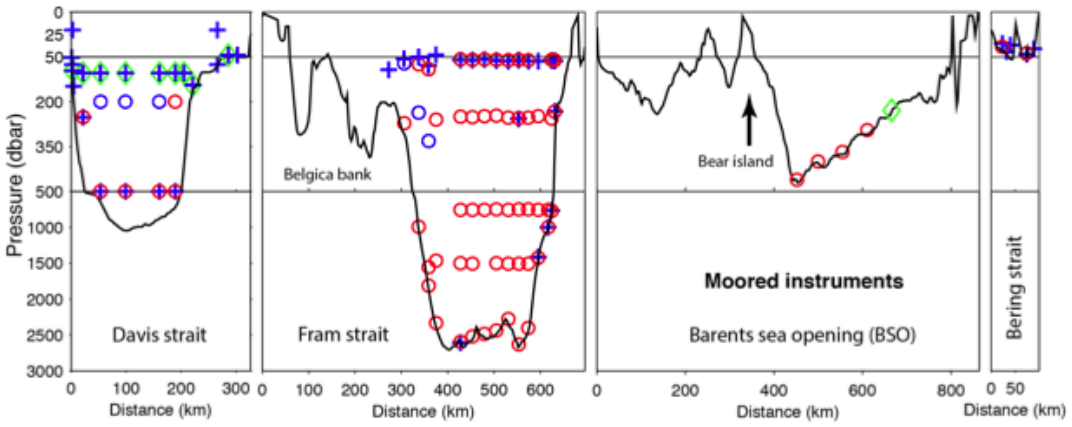

Figure 3: Locations of moored instruments in each strait: Blue crosses symbolise instruments measuring T and S. Red (and blue) circles show positions of current meters measuring velocity, T (and S). Green diamonds shows ADCPs which measure velocity profiles (Tsubouchi et al., 2016, Fig. 2, reprinted with permission).

individual standard instrument depths for each strait, vertically at each mooring site to gain full depth information and finally horizontally at all depths between the mooring sites. The T, S and v data from the instruments are filtered to remove tidal signals and to discard instrumental records with too low temporal coverage. The obtained five-day fields are then averaged to give monthly data. Those data are used as initial values to calculate velocities that comply with mass and salinity conservation constraints in the Arctic ocean box. (Tsubouchi et al., 2016)

Tsubouchi et al. (2016) calculate volume, heat and freshwater transports across each of the sections from those monthly T, S and v data using the mean temperature and salinity across the Arctic boundary as T_{ref} and S_{ref}, respectively (Tsubouchi et al., 2012). In Tsubouchi et al. (2016) the authors compute heat and freshwater fluxes referenced to their definition, as well as to reference values found in the literature to compare their results. For Davis Strait and the BSO the resulting heat flux estimates agree with the respective literature within their uncertainty ranges. In the Eastern Fram strait the WSC heat flux seems to be overestimated compared to literature values, whereas both heat and freshwater fluxes are underestimated in Bering Strait.

The ARCGATE dataset comprises monthly data of potential temperature, salinity and velocity sections in each strait for the 12-month period from September 2005 to August 2006, henceforth refered to as the "ARCGATE period". The ARCGATE "grid" is made up

of 2714 vertical levels with one dbar spacing[18], 643 temperature and salinity stations and 639 velocity stations with slightly different coordinates for T and S stations compared to the v stations. The monthly estimates of volume, heat and freshwater fluxes are included in the dataset.

2.3 Data Comparisons

In order to compare the ocean reanalysis data from C-GLORS with the observational data from ARCGATE, both datasets are investigated in the same areas - namely, the cross sections through the four main Arctic gateways. For this purpose, points from the C-GLORS native grid are chosen which lie as close as possible to the ARCGATE points. Due to the nature of the tripolar grid and because the ARCGATE line of points crosses several of the C-GLORS grid lines, the resulting line of points from the C-GLORS dataset is irregular. This means that neither i- nor j- indices of the C-GLORS points stay constant for any of the four cross sections. Figure 4 shows the ARCGATE points in green and the chosen C-GLORS points in red, exemplary for the cross section through Davis Strait. The grid lines show the C-GLORS "v-grid". Therefore the points on the grid lines are points in which the meridional velocity is given, whereas points between the grid lines lie on the "u-grid" on which the zonal velocity is known. It becomes obvious from looking at this graph that the spatial resolution in the cross sections is much higher from the ARCGATE data than from the C-GLORS data. The grid lines are slightly bent due to the fact that the lines converge at the poles of the tripolar grid in Canada and Siberia, whose locations are visualized by the two dents in the red line in Fig. 5).

For calculating mass and energy fluxes through this irregular line of chosen points the volume or mass and heat fluxes through each point and at each depth are required.

2.3.1 Calculating Ocean fluxes

Even though fields of volume and heat fluxes are available on the model native grid in daily resolution from C-GLORS, those fluxes are calculated directly from the daily fields of temperature (T) and meridional (v) and zonal (u) velocities. This might seem like an unnecessary step at first. However a comparison between the C-GLORS post-processed fields and the fields calculated from daily T, u and v data for a section across 70 °N(see

[18] 1 dbar = 10^4 Pa (Kundu et al., 2012)

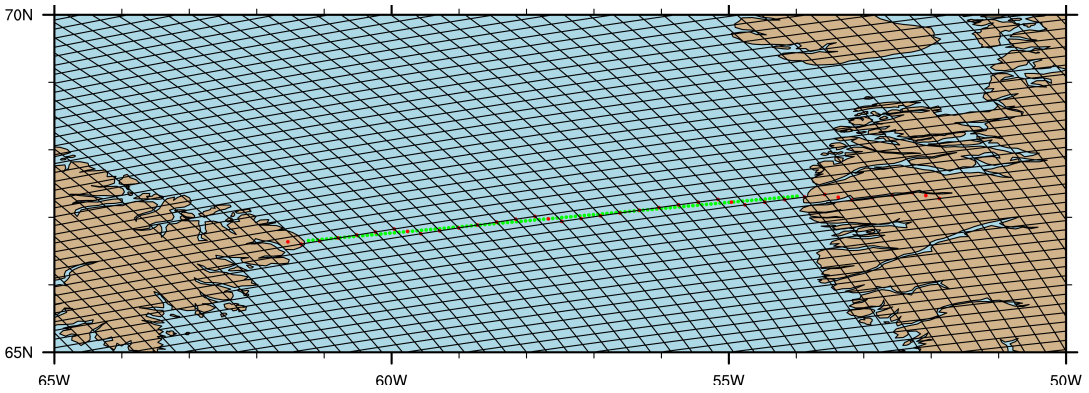

Figure 4: ARCGATE grid (green) for Davis Strait and chosen C-GLORS points (red) closest to ARCGATE points. Black lines show the model-native grid lines for the v-grid.

Fig. 5) reveal that this step yields more accurate results, as will be explained.

First, the method of computing monthly mass and heat fluxes on the model native grid shall be outlined. Computation of the volume flux is straightforward: In each model grid point (both on the u and on the v grid) the daily velocities are multiplied by the respective dz-vector (dz_u for u velocities and dz_v for v velocities). Then the monthly average of this product is calculated[19] and summed up over all depth levels, yielding the depth integral of the monthly velocity at each grid point from the ocean bottom to the surface (without SSH). The monthly means of meridional and zonal volume fluxes for the v and u grid points are obtained by multiplication with the corresponding fields of dx_v and dy_u, respectively.

The heat flux computation requires a bit more caution, since daily in-situ temperature fields are available on the T-grid, but potential temperature fields are required on the u- and v- grids. First the in-situ temperature fields are interpolated linearly, along constant j indices to get T on the u-grid, and along constant i indices to get T on the v-grid. This method is preferred over bilinear interpolation (the average of the four closest points) in this case, because the variables are arranged such that temperature points always lie "left" and "right" of u-points, and "above" and "below" v-points (see Fig. 10). These interpolated daily in-situ temperature fields are converted into daily fields of potential temperature using the NCAR Command Language (NCL) function "potmp_insitu_ocn" which requires the input of salinity, temperature, and pressure at

[19] It would be more efficient to calculate the monthly average first and then compute the depth integral, however the daily product of velocities with dz are required for the heat flux calculations.

the respective points. Therefore, also the salinity needs to be interpolated from the T-grid onto the u- and v-grids. The pressure is calculated from the depth at each grid point using the NCL function "depth_to_pres " .

The potential temperature fields on the u-grid (θ_u) and on the v-grid (θ_v) are then multiplied by the product of u with dz_u and v with dz_v, respectively. In this case, the reference temperature (θ_{ref}) has been set to 0° C (see Ch. 1.6) - otherwise θ_{ref} would have to be subtracted prior to this multiplication. Now the monthly averages and depth integrals can be calculated which are finally multiplied with dx_v and dy_u. The heat flux in W is obtained by multiplication of this product by the constants $\rho_0 = 1026$ kg/m^3 and $c_w = 3990$ J/kg·K.

In order to estimate the influence of changes in sea surface height, the SSH values (which lie on the T-grid) are interpolated to the u- and v-grids in the same way as the temperatures are. The resulting daily fields of SSH_u and SSH_v are then multiplied with the daily u- and v-velocities of the uppermost layer, respectively. Similar to the heat flux calculation, those products are then either averaged over the time dimension to get the monthly volume flux in the SSH layer or multiplied by the constants ρ_0 and c_w as well as the temperatures at each grid point before calculating the monthly means of the heat flux in the SSH layer.

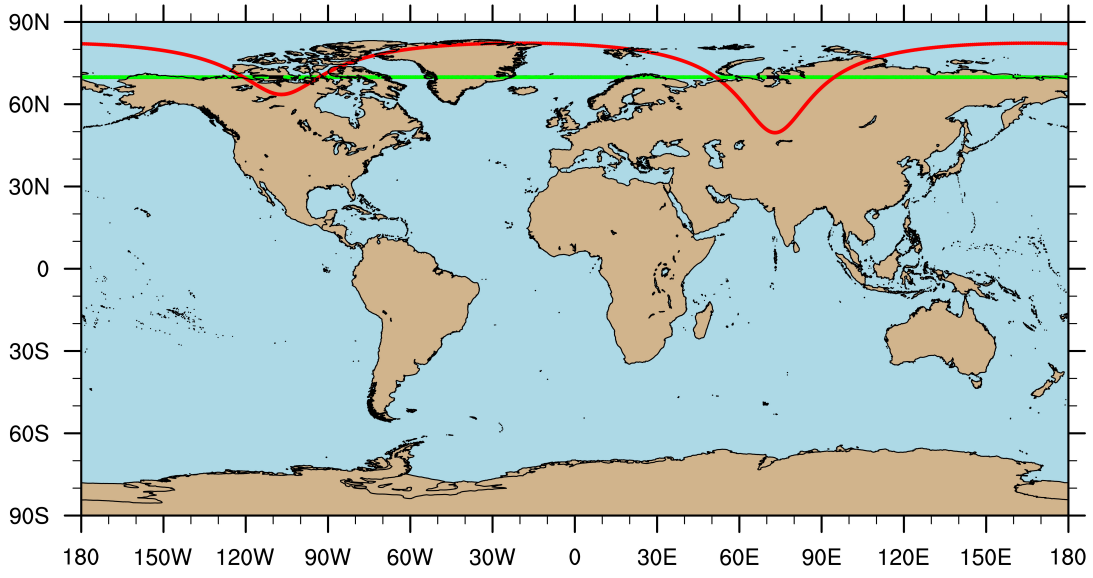

Figure 5: Points for 70°N: Green points show the chosen C-GLORS points, red points demonstrate a line of constant j index. The green points are selected using the same algorithm as for the sections through the Arctic gateways.

Figures 6 and 7 show the smoothed[20] monthly anomalies of the volume and heat transports across 70°N for the period from January 2000 to 2013. The heat fluxes in this graph are based on the in-situ temperatures T and not on θ. The transports are calculated once using the post-processed fields from C-GLORS (green line) and twice derived from daily fields of T, u and v (orange and black lines). The only difference between the orange and black line is that they show the transports including (orange) and neglecting (black) the contribution from changes in the SSH. Additionally, the fluxes through 70°N taken from the interpolated fields on the regular lat/lon grid is shown in red. The oceanic transports (black, orange, green and red lines) are positive towards the North representing an inflow of water into the Arctic Ocean for the volume transports, and an inflow of water with a higher temperature than T_{ref} for the heat transports. In the plot for the volume transports (Fig. 6), a blue line is given as a reference. This line shows the total freshwater flux through the Arctic Ocean's surface ($F_{S,FW}$), which is taken positive upward in this case and is the difference between evaporation (E) and the sum of precipitation (P), icemelt (M) and river runoff (R). The freshwater flux is given on the interpolated grid. It has the units kg/s and is divided by $\rho_{FW} = 1000$ kg/m^3 to get the volume flux.

Figures 6 and 7 show that both flux anomalies calculated based on the velocity fields show a much weaker variability, and therefore less noise, than those derived from the C-GLORS post-processed fields, which is a strong argument for using the former instead of the latter. Another supporting argument for recalculating the fields is that the average fluxes for the period 2000 to 2013 (- 0.14 ± 0.18 Sv and 180 ± 40 TW (both have the same mean values including and neglecting SSH)) agree much better with the observational estimates presented in Tsubouchi et al. (2016) for the transports into the Arctic Ocean (although not across 70°N) during the ARCGATE period (- 0.15 ± 0.06 Sv and 154 ± 44 TW) than the averages calculated from the C-GLORS post-processed fields (+ 0.3 ± 8.9 Sv and 240 ± 110 TW).

Additionally, Figure 6 reveals a much better agreement between the fluxes derived from daily T, u and v fields and the freshwater flux through the surface than between the fluxes from post-processed or interpolated fields and the surface freshwater flux. Assuming stationary conditions the oceanic freshwater flux into the Arctic Ocean should be equal

[20] 12-month running average

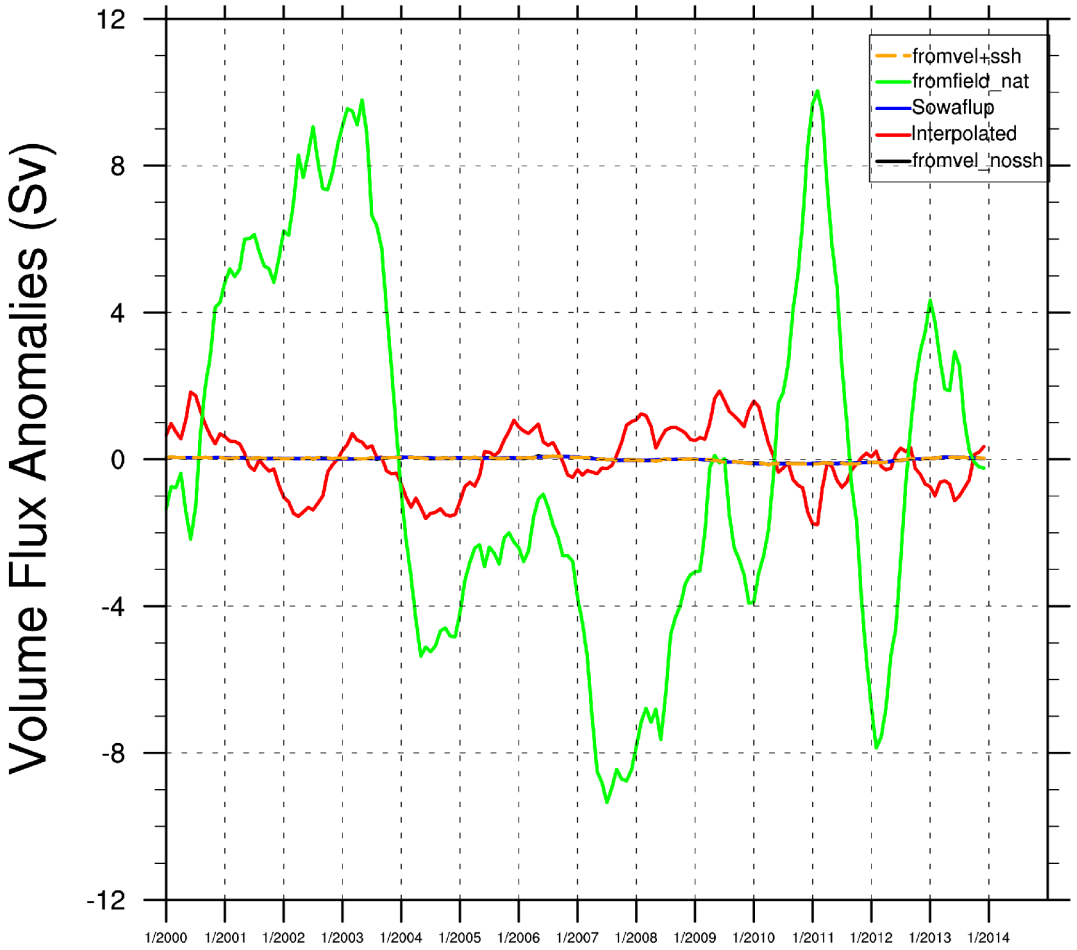

Figure 6: Volume flux anomalies from monthly climatology for the period 01/2000 - 12/2013 in Sv. Orange line ("fromvel + ssh") = Flux calculated from velocity fields including SSH. Green line ("fromfield_nat") = Flux obtained from C-GLORS post-processed fields on native grid. Blue line ("sowaflup") = Freshwater flux through surface (positive upward, expressed as volume flux using ρ_0 =1026 kg/m^3). Red line ("Interpolated") = Flux obtained from C-GLORS post-processed fields on regular grid. Black line ("fromvel_nossh") = Flux calculated from velocity fields without influence of SSH.

to the (upward) freshwater flux through the surface ($F_{S,FW}$)(Serreze et al., 2006). The oceanic freshwater flux (F_{FW}) can be calculated from the total oceanic volume flux (F_T) with

$$F_{FW} = F_T(1 - \frac{S}{S_{ref}}) \tag{20}$$

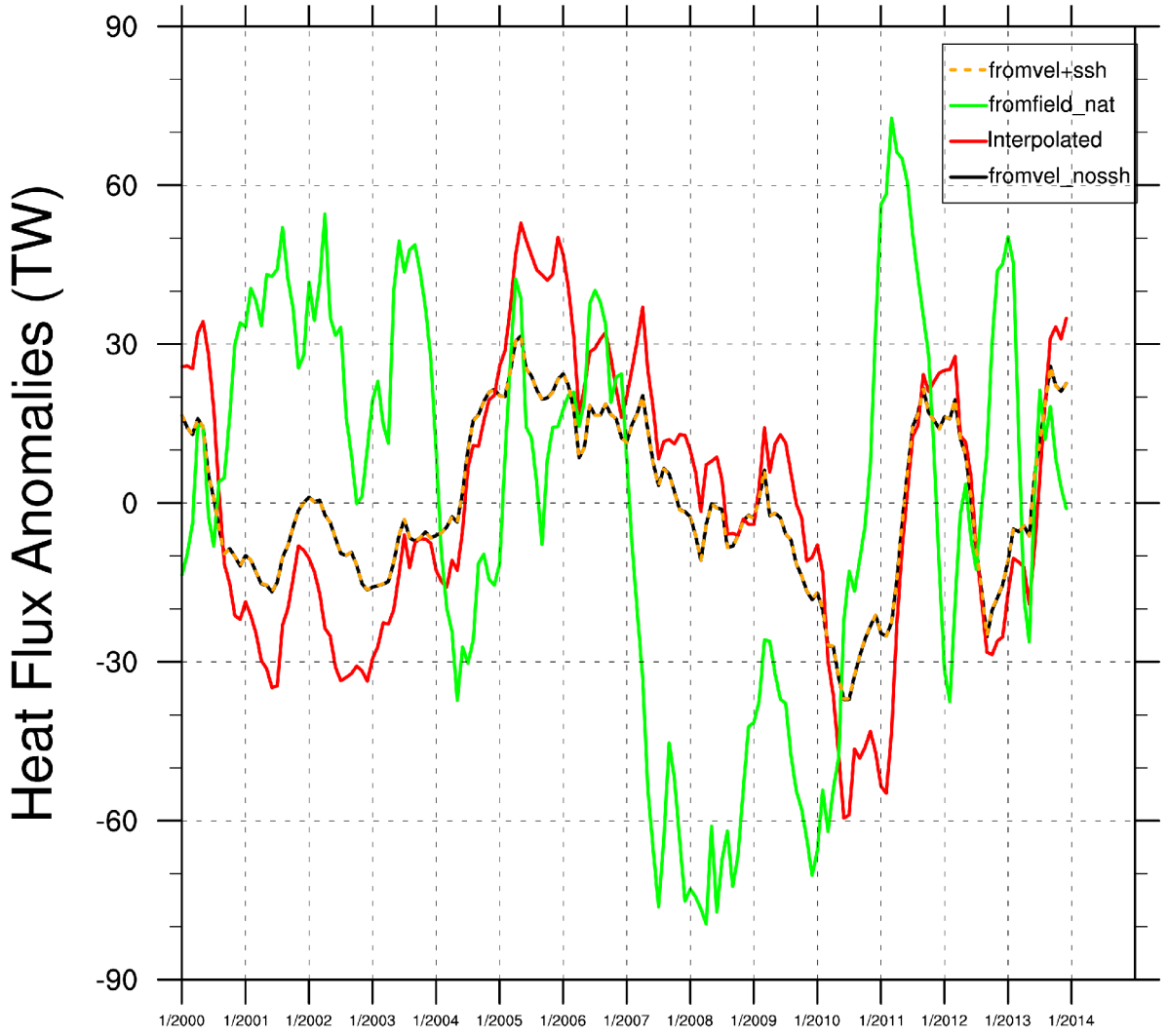

Figure 7: Heat flux anomalies from monthly climatology for the period 01/2000 - 12/2013 in TW. Line colouring similar to Fig. 6.

where S is the bulk salinity of F_T and S_{ref} is the reference salinity[21] (Serreze et al., 2006). Since the fluxes are calculated for a closed boundary through which the net oceanic volume flux must be zero under stationary conditions the only contribution to the volume flux is due to $F_{S,FW}$ (Tsubouchi et al., 2012).

The figures also clearly show that it is preferable to use the fields on the model native grid instead of using the interpolated fields. The interpolated fields are much more noisy and the difference between the 2000-2013 averages (- 0.8 $\pm$ 2.3 Sv and 246 $\pm$ 65 TW) and the literature values (see above) is also greater than for the fields calculated in this work.

Figures 8 and 9 show only the volume and heat fluxes, respectively, which are obtained

[21] S_{ref} is often set to the volume mean salinity of 34.8 PSU for the Arctic (Tsubouchi et al., 2012)

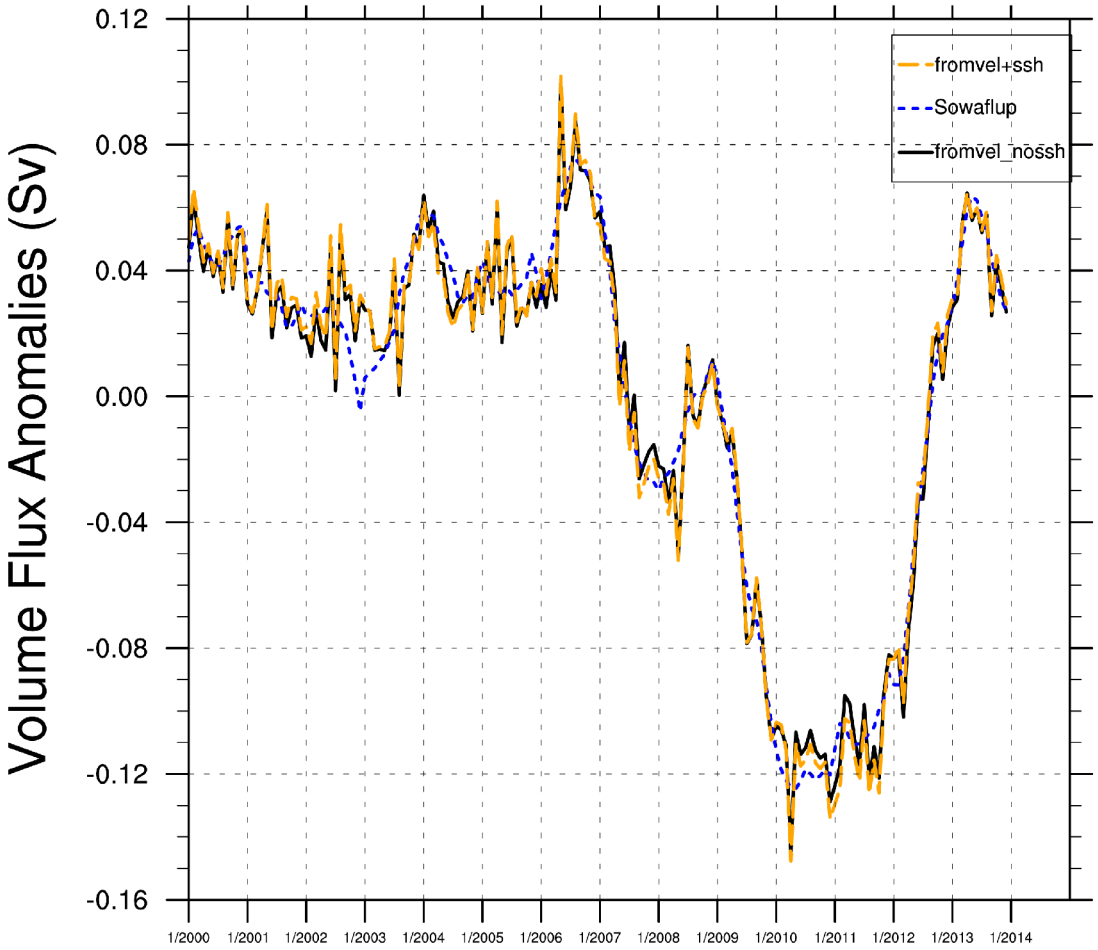

Figure 8: Volume flux anomalies from monthly climatology for the period 01/2000 - 12/2013. Line colouring similar to Fig. 6.

from the daily fields including and neglecting the influence of SSH, as well as the freshwater flux through the surface for the volume flux plot. It is clear from both figures that the contribution from SSH fluxes is small in the Arctic region (on average + 0.03 Sv and - 0.6 TW) and that the discrepancies between the fluxes derived from the C-GLORS post-processed fields versus the computed fluxes based on daily temperature and velocity fields are not attributable to fluxes through the SSH layer.

There is a small difference between the surface flux timeseries (blue, average = - 0.13 $\pm$ 0.12 which is perfectly consistent with the 1997-2010 average surface flux estimate of - 0.14 $\pm$ 0.0 Sv presented by Valdivieso et al. (2014)) and the fluxes derived from T, u and v fields (black and orange lines) which could be attributable on the one hand to the contribution of sea ice melt to $F_{S,FW}$, because sea ice is not included in the oceanic

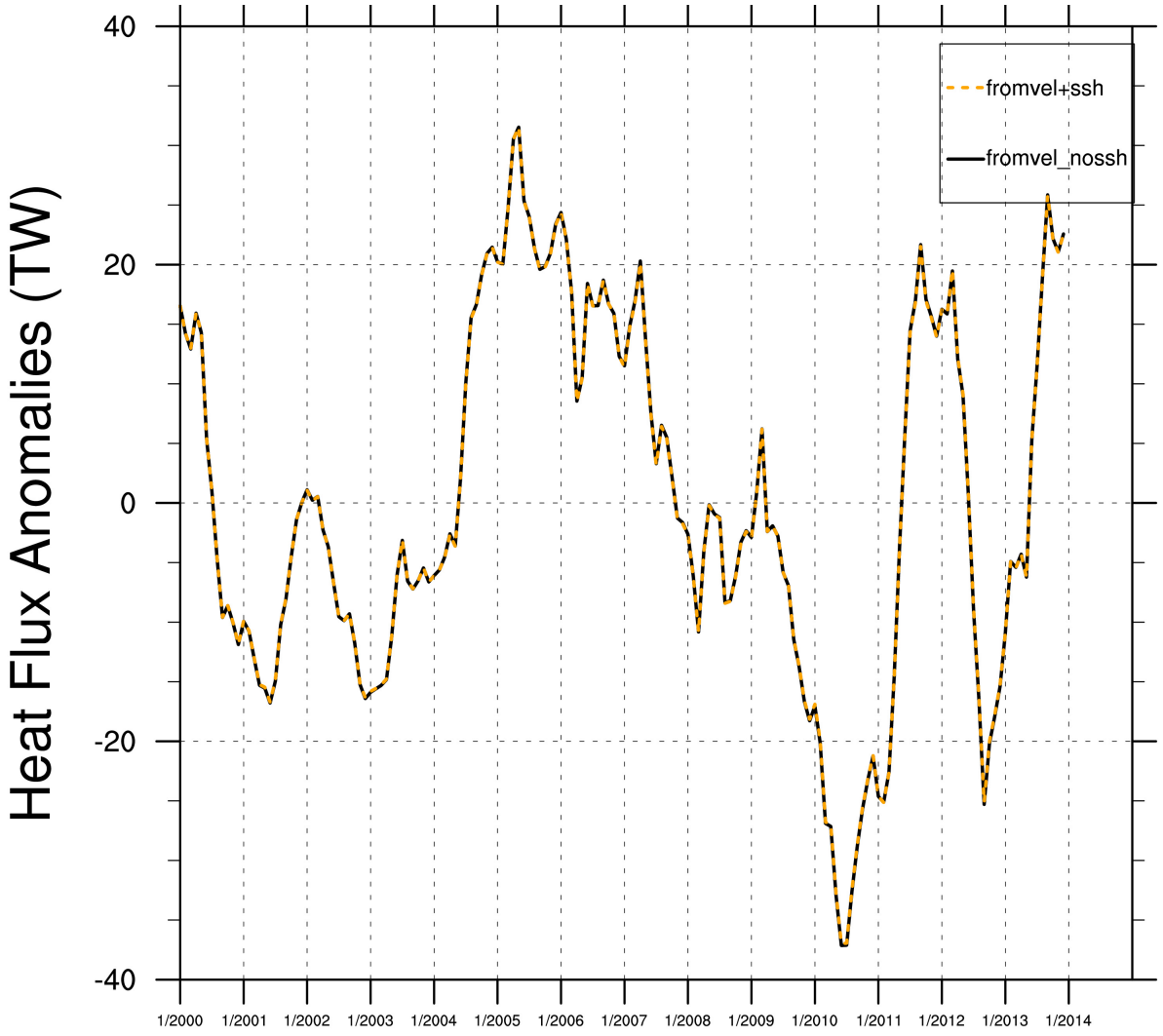

Figure 9: Heat flux anomalies from monthly climatology for the period 01/2000 - 12/2013. Line colouring similar to Fig. 6.

volume fluxes (black or orange curves). More importantly, the blue curve is taken from the interpolated grid (regular latitude/longitude grid) whereas the other curves are calculated directly from the native grid. However it is clear that overall the curves align very well, which also supports the employed method for finding the appropriate points on the model native grid and for calculating the fluxes.

Albeit a similar comparison between the transports based on the C-GLORS post-processed fields and those derived directly from T, u and v yields somewhat less obvious differences in the case of the sections through the four Arctic gateways, all of the following calculations are carried out using the velocity based fields and not the ones available from C-GLORS.

2.3.2 Comparing Time Series

Even though heat and volume flux timeseries are available from the ARCGATE dataset, the heat fluxes need to be calculated from the given monthly temperature and velocity data so that the same reference temperatures and constants can be used as for the C-GLORS calculations. Otherwise a direct comparison of the two datasets is not possible. For this purpose the monthly temperature data are linearly interpolated from the 643 temperature and salinity grid points to the 639 velocity grid pairs. Again the heat flux is computed from velocity, temperature, ρ_0 and c_w. Then the depth integral is computed for each ARCGATE point, which is then multiplied by the spherical distance between the temperature grid points to the left and right of the respective velocity grid point, since the velocity points are in between two temperature points.

The total monthly heat flux ($\overline{Tv}$) at each point can be decomposed into the contribution from transient eddies ($\overline{T'v'}$) and the contribution from the stationary circulation ($\bar{T}\bar{v}$) (Peixoto and Oort, 1992, p. 324). The bar denotes the temporal mean and the apostrophe stands for the temporal deviation from this mean. For comparison purposes, the depth integrated C-GLORS heat fluxes need to be calculated again, this time based on the product of monthly potential temperature and monthly velocity fields ($\bar{T}\bar{v}$) since the ARCGATE fluxes are also based on monthly data.

These fluxes are integrated along the irregular line of points (see Fig. 4) in each of the four gateways. The meridional and zonal velocities are perpendicular to this irregular line in each point. In order to capture the total volume or heat flux passing through a cross section perpendicularly, the depth integrated fluxes in all the points along the irregular line are added up, being careful to choose the zonal transports in the u-grid points and the meridional transports in the v-grid points with the correct signs. This is done for each gateway, resulting in time series of fluxes through the individual sections and of the net flux.

The timeseries thus obtained from the ARCGATE and C-GLORS datasets can now be compared. The assumption for this comparison is that the oceanic flux perpendicular to the irregular line and the oceanic flux perpendicular to the ARCGATE line are similar. The difference between C-GLORS and ARCGATE derived timeseries are quantified by comparing averages over the ARCGATE period and computing cross correlations and Root Mean Square Deviations (RMSDs).

2.3.3 Comparing Cross Sections

A method for a qualitative comparison of the two datasets is to plot cross sections for velocity, heat flux (in W/m^2) and temperatures through each gateway along the ARCGATE line. This approach is especially useful for analyzing which parts of the sections contribute most to possible dissimilarities between the time series. Preparing the datasets for those cross sections is not straight forward and the methodology shall therefore be explained in detail in this section.

The first part of the preparation is to project the velocities from the C-GLORS data onto the normal vector of the ARCGATE line ($\mathbf{n}_{AG}$). Figure 10 illustrates the following algebraic considerations using an exemplary u-grid point ($u_{i,j}$): The C-GLORS velocity (u^u) in each u-grid point is actually the component of the C-GLORS velocity vector $\mathbf{v^u}_{CG}$ parallel to the vector $\mathbf{e_{1,u}}$ in the same point. There is no information directly available on the velocity component in the direction of $\mathbf{e_{2,u}}$ in the u-point (v^u). This component of $\mathbf{v^u}_{CG}$ is obtained by interpolating the velocities from the v-grid to the u-grid in a bilinear fashion using the built-in NCL function "ESMF-regrid". The three dimensional base vectors $\mathbf{e_{1,u}}$ and $\mathbf{e_{2,u}}$ are calculated in cartesian coordinates as the vectors between $T_{i,j}$ and $T_{i+1,j}$ for $\mathbf{e_{1,u}}$ and the vector between $f_{i,j-1}$ and $f_{i,j}$ for $\mathbf{e_{2,u}}$, each divided by the length of the respective vector to obtain unit vectors. The cartesian coordinates of the T- and f- grid points are computed on a unit sphere using the NCL function "css2c". The three dimensional velocity vector in the u-grid point $u_{i,j}$ expressed in cartesian coordinates is calculated as follows:

$$\mathbf{v^u}_{CG} = u^u \cdot \mathbf{e_{1,u}} + v^u \cdot \mathbf{e_{2,u}} \tag{21}$$

Of course the velocity vector in each v-grid point is calculated in a similar manner, using the coordinates of the appropriate T and f points to calculate the base vectors and interpolating the u velocities onto the v-grid.

The next step is to define a segment of the ARCGATE line for each C-GLORS point on the irregular line and to find the appropriate normal vector $\mathbf{n}_{AG}$ onto which $\mathbf{v}_{CG}$ in the corresponding point shall be projected. Figures 11 - 14 show the ARCGATE and C-GLORS points chosen in this step for each gateway: The points in the ARCGATE array (black) are detected which lie closest to the chosen C-GLORS points (red), finding one ARCGATE point for each C-GLORS point. Additionally, the ARCGATE points closest

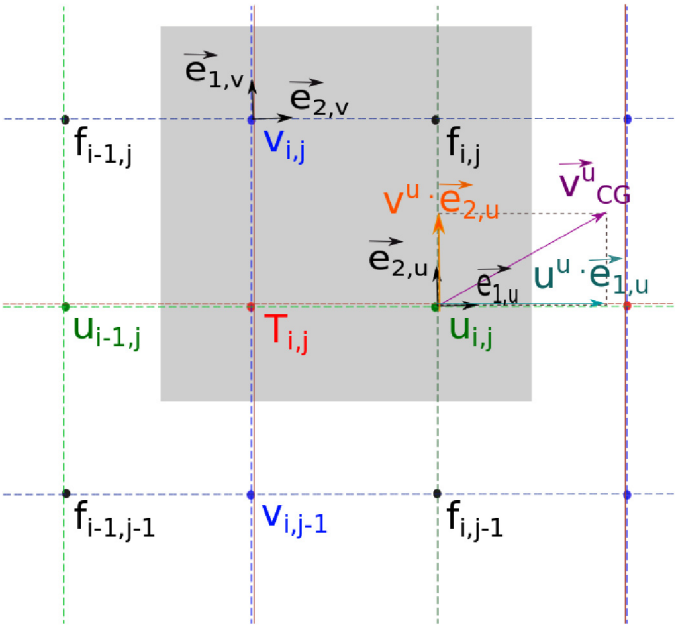

Figure 10: Schematic of the staggered NEMO grid with T-grid and points in red, the same for u in green, v in blue and f in black. The shaded area shows the four grid points with the same indices (i,j). The graphic also includes the unit vectors $\mathbf{e_{1,u}}$ and $\mathbf{e_{2,u}}$, vector components and velocity vector $\mathbf{v^u}_{CG}$ at a u-grid point. Base vectors are included for a v-grid point as well ($\mathbf{e_{1,v}}$ and $\mathbf{e_{2,v}}$). Adapted from Madec (2016, p. 52).

to the corresponding f-grid points (not shown) are found (green). Those points are used to calculate both the distance and direction ($\mathbf{e}_{AG}$) of the ARCGATE line segment for each C-GLORS point, again using the conversion from latitude/longitude to cartesian coordinates. The 3D normal vector $\mathbf{n}_{AG}$ is equal to the cross product of the vector $\mathbf{e}_{AG}$ with the vector from the origin of the coordinate system to the respective ARCGATE point, divided by the length of the resulting vector. Finally, the projection CG_p of the velocity vector from C-GLORS in each chosen point (red) onto the respective normal vector is simply the scalar product

$$CG_p = \mathbf{v}_{CG} \bullet \mathbf{n}_{AG} \tag{22}$$

It is ensured that the angle between $\mathbf{v}_{CG}$ and $\mathbf{n}_{AG}$ does not exceed 90° so that the sign of CG_p is correct. These daily velocity projections are then averaged over time to give monthly values for velocity cross sections. The heat fluxes should be calculated by multiplying daily projected velocities and potential temperatures with each other.

However, in order to compare ARCATE and C-GLORS heat fluxes the monthly means of daily projected velocity and potential temperature fields are multiplied with each other, and finally scaled by ρ_0 and c_w.

Now the ARCGATE velocities and heat fluxes are prepared for the cross section plots. The depth-resolved monthly velocities are available from the dataset and the monthly heat fluxes at each depth have already been calculated in preparation for the time series (see Ch. 2.3.2). The fluxes from the entire ARCGATE array are averaged in between the green "ARCGATE-grid" points (see eg. Fig. 11) to get one representative value in each black point (closest ARCGATE to chosen C-GLORS point) in order for the horizontal resolution to be equal to that of the C-GLORS field (red points). Similarly, the C-GLORS depth levels are interpolated vertically to match the depth levels of the ARCGATE array. Matching the C-GLORS depths to the ARCGATE depths is straightforward whereas the other way around is more complicated, because the C-GLORS depth vector is different in each point. A minor adaptation is necessary as the C-GLORS depth levels are given in meters while the ARCGATE depth levels are actually pressure levels. Therefore, the NCL function "depth_to_pres" is applied to the C-GLORS depth vector in each point. The heat flux is plotted in each point at each depth level with the units "W/m^2" instead of TW for better interpretability of the plots.

The assumption with this method is that the projected C-GLORS velocities in each of the red points is equal to what the C-GLORS velocity would be in the corresponding black point. This is not really an approximation in most cases since the red and black points are very close to each other except in the Barents Sea Opening, where the ARCGATE and C-GLORS points only overlap in few places and for the first two points in Western Fram Strait, because the ARCGATE coverage is limited in this area (see Figs. 11 - 14). In a few of the stations in the BSO and Bering Strait the C-GLORS f-grid points share exactly the same green ARCGATE points, which means that there is no segment on the ARCGATE line onto which the C-GLORS velocity vector should be projected. Those areas initially appear as fill values in the cross section plots for both the C-GLORS and ARCGATE, but are filled through horizontal interpolation.This method is deemed appropriate because there is always only one missing column in between two columns with values, with the exception of one single occurrence in the BSO where there are two missing columns next to each other.

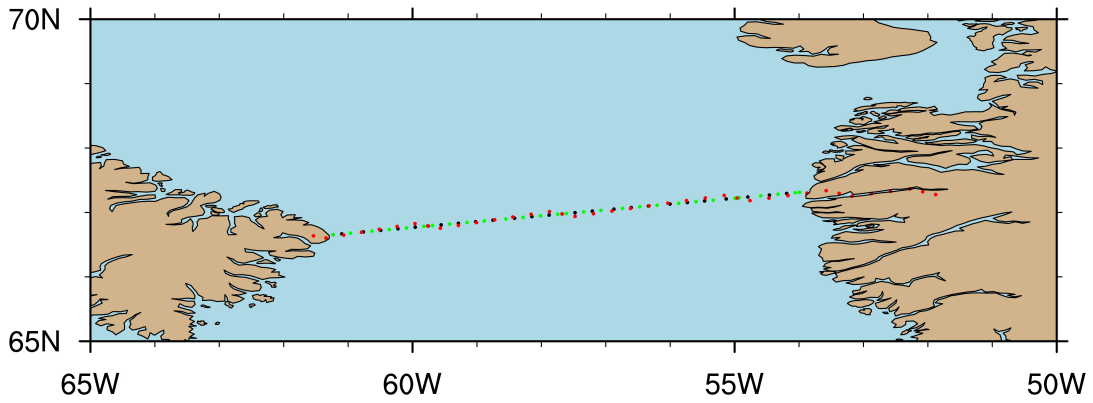

Figure 11: Davis Strait points. Chosen C-GLORS points (red) and ARCGATE points closest to C-GLORS points (black). The green points show the points form the ARCGATE array which define the line segment for the corresponding C-GLORS point.

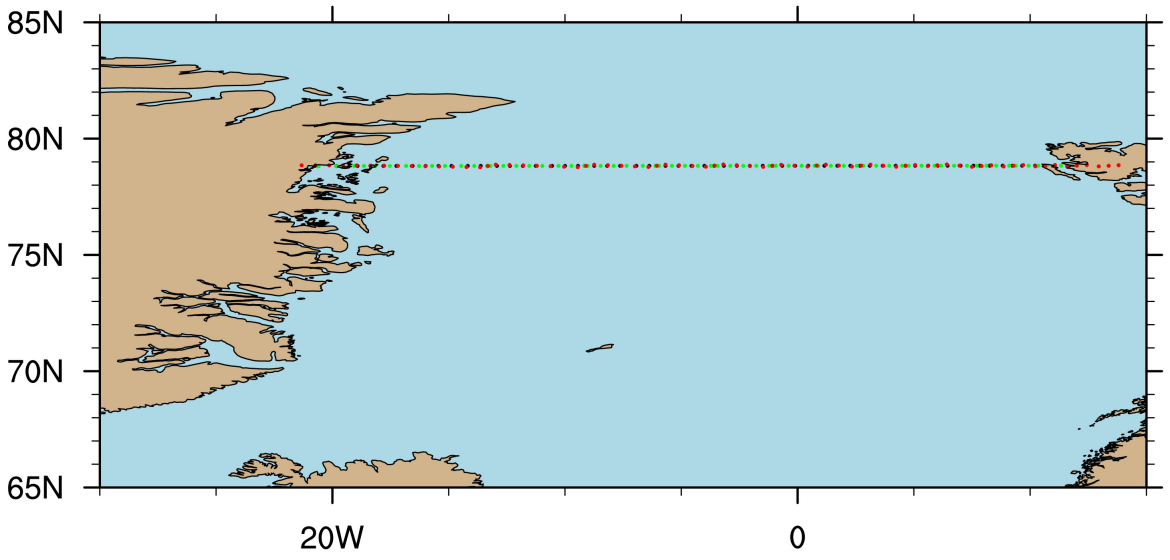

Figure 12: Fram Strait points.

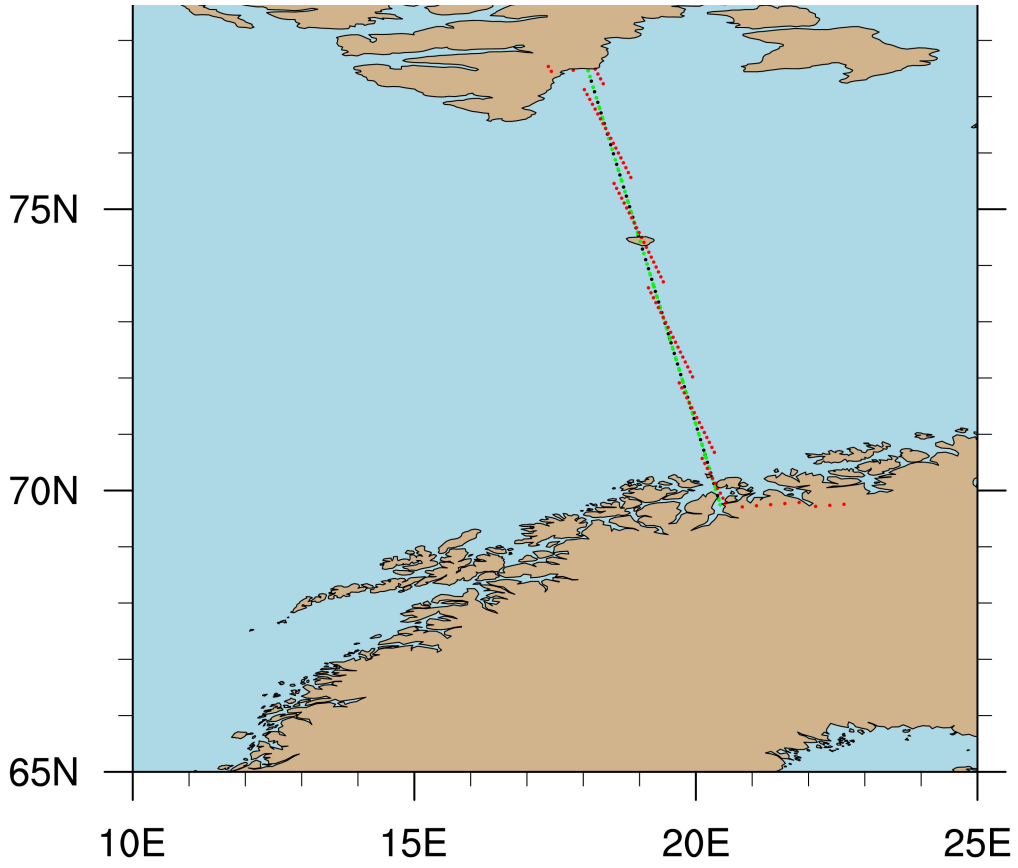

Figure 13: Points in the Barents Sea Opening.

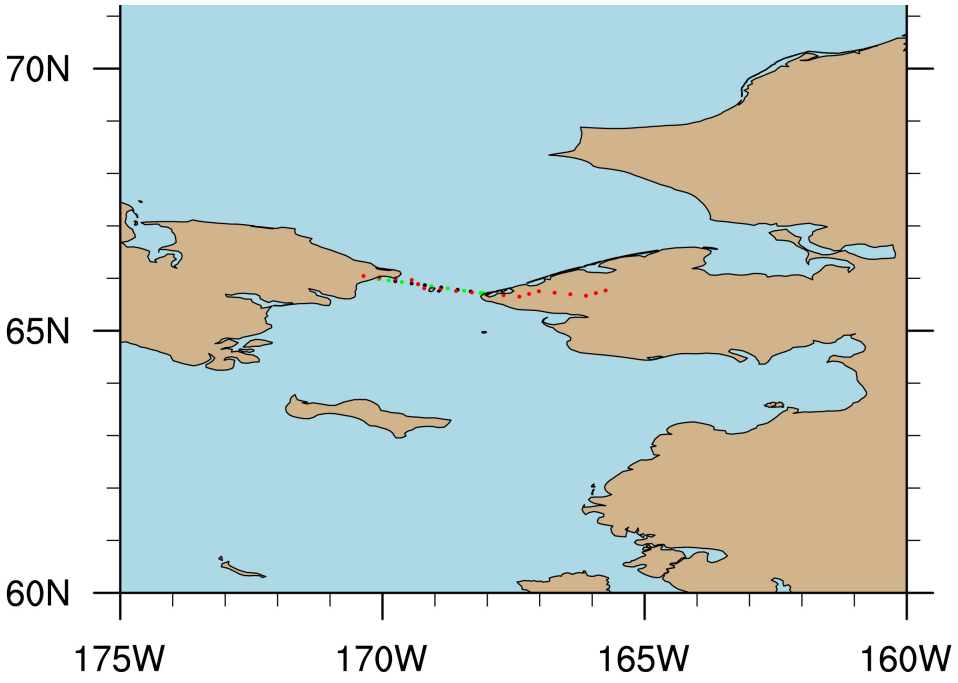

Figure 14: Bering Strait points.

3 Results and Discussion

In this chapter the ARCGATE and C-GLORS timeseries and cross sections are shown, qualitatively discussed and quantitatively compared. Additionally, the estimates obtained in this work are compared with literature estimates. Similarities and differences between the reanalysis and the observations are highlighted and discussed, attempting to find possible explanations for the discrepancies.

3.1 Time Series

3.1.1 Volume Transports

First, the time series of volume fluxes for both C-GLORS and ARCGATE are shown for the ARCGATE period. As discussed in Chapter 2.3.2, the C-GLORS fluxes through the ARCGATE sections are calculated based on monthly averages of the velocities given on the model-native tripolar grid. The ARCGATE volume fluxes are available from the dataset. Figure 15 shows the volume fluxes through each strait as well as the net volume flux (sum of all straits) from C-GLORS and ARCGATE. Period averages, zero-lag cross correlations between the timeseries and RMSDs are given in Table 1. Uncertainties are temporal standard deviations of the monthly values from the period averages.

Qualitatively, the contributions of each strait to the net volume transports into or out of the Arctic Ocean are captured well by the reanalysis, both compared to the theory (described in Ch. 1.2) and to ARCGATE. As expected, the main contribution to volume transport into the Arctic Ocean is the Barent Sea Opening and the largest outflow occurs in Davis Strait. Also, the net flux is close to zero with an average volume export of - 0.05 $\pm$ 0.22 Sv (- 0.14 $\pm$ 0.06 Sv from ARCGATE, see Tab. 1) out of the Arctic Ocean, which - assuming stationary conditions - is due to precipitation, ice melt and river runoff exceeding evaporation in the polar cap by approximately 0.15 Sv (see Ch. 2.3.1).

The net volume flux (black) from C-GLORS is in good agreement with that from ARCGATE, especially from April to July 2006. The volume fluxes through Fram Strait (green) and Bering Strait (cyan) are also similar between C-GLORS and ARCGATE for the whole period. However, there is a considerable difference for the flux through the BSO (blue) and even more so for Davis Strait (red).

The monthly volume import is overestimated by the C-GLORS reanalysis in the BSO

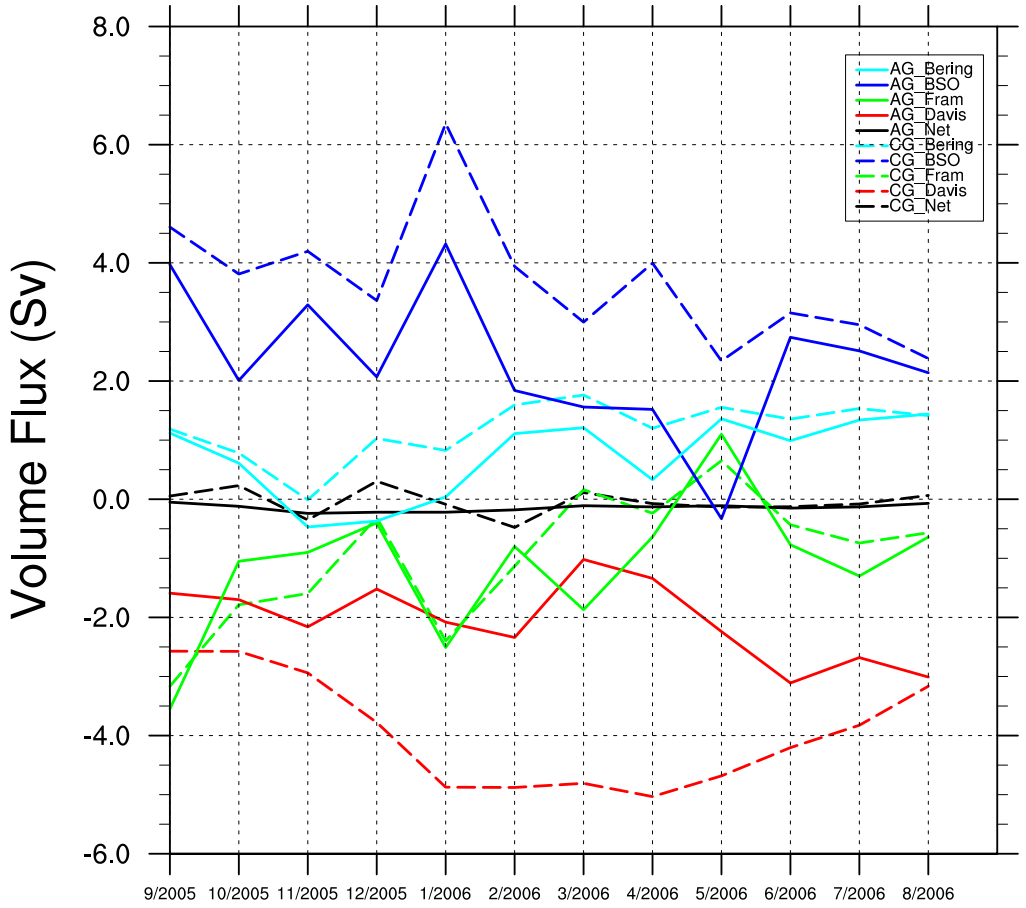

Figure 15: Volume Flux in Sv through Davis, Fram, Bering Strait, the BSO and net flux into the Arctic for C-GLORS (short: CG, dashed line) and ARCGATE (short: AG, solid line) for the ARCGATE period.

throughout the entire period compared to the ARCGATE observations. The volume export through Davis Strait is also overestimated in the C-GLORS data, which balances the surplus in the BSO resulting in an accurate representation of the net flux. The average difference between the ARCGATE and C-GLORS net fluxes is - 0.1 $\pm$ 0.2 Sv.

The agreement in all straits is good for the two months at the beginning and end of the ARCGATE period (September 2009 and August 2006). There is a remarkably good agreement in Fram Strait in December 2005 and January 2006 with absolute differences of only - 0.09 and - 0.11 Sv in those two months.

The reanalysis-based averages for Bering and Fram Strait as well as for the net flux agree with the ARCGATE averages within the standard deviation. The BSO average from the reanalysis is only slightly outside of this range. The best agreement is clearly found in Fram Strait and for the net flux. The fact that the cross correlation is high in Fram

Strait	C-GLORS AG period	ARCGATE AG period	r	RMSD	C-GLORS 2004-2010
Davis	- 3.9 ± 0.9	- 2.1 ± 0.7	- 0.10	2.20	- 3.7 ± 0.9
Fram	- 1.0 ± 1.1	- 1.1 ± 1.2	0.79	0.72	- 1.0 ± 1.0
BSO	3.7 ± 1.1	2.3 ± 1.2	0.74	1.59	3.3 ± 1.0
Bering Strait	1.2 ± 0.5	0.7 ± 0.7	0.82	0.60	1.3 ± 0.4
Net	- 0.05 ± 0.22	- 0.14 ± 0.06	0.32	0.22	- 0.1 ± 0.2

Table 1: Average volume fluxes in Sv for C-GLORS and ARCGATE for the ARCGATE period (AG period) and for 2004-2010 for C-GLORS. Positive flux values represent Arctic inflow. Correlation coefficient r and RMSD between C-GLORS and ARCGATE timeseries during the ARCGATE period are given. The "uncertainties" are simply the standard deviation from the mean and therefore due to variability between the months. All units are Sv except for r (unitless).

Strait, the BSO and Bering Strait implies an accurate representation of the seasonal cycle in the reanalysis compared to ARCGATE during the ARCGATE period. It is obvious from Figure 15 that the correlation in Davis Strait is low, even negative, due to the large discrepancy throughout the entire period with the exception of the last month.

Figure 16 shows the seasonal cycle of volume transports through each strait obtained from the C-GLORS dataset for the period 2004 - 2010. The seasonal cycle presented here is in perfect agreement with the seasonal cycle obtained also for the C-GLORS, Version 5 reanalysis by Iovino et al. (2016), which adds high confidence in the methods employed in this thesis.

3.1.2 Comparison with literature estimates

Davis Strait

The largest discrepancy between the ARCGATE and C-GLORS timeseries is found in Davis Strait. This calls for a comparison with other volume flux estimates found in the recent literature. Curry et al. (2011) estimate the volume flux to be - 2.3 ± 0.7 Sv based on moored observations (in the same locations as in the ARCGATE array) between 2004

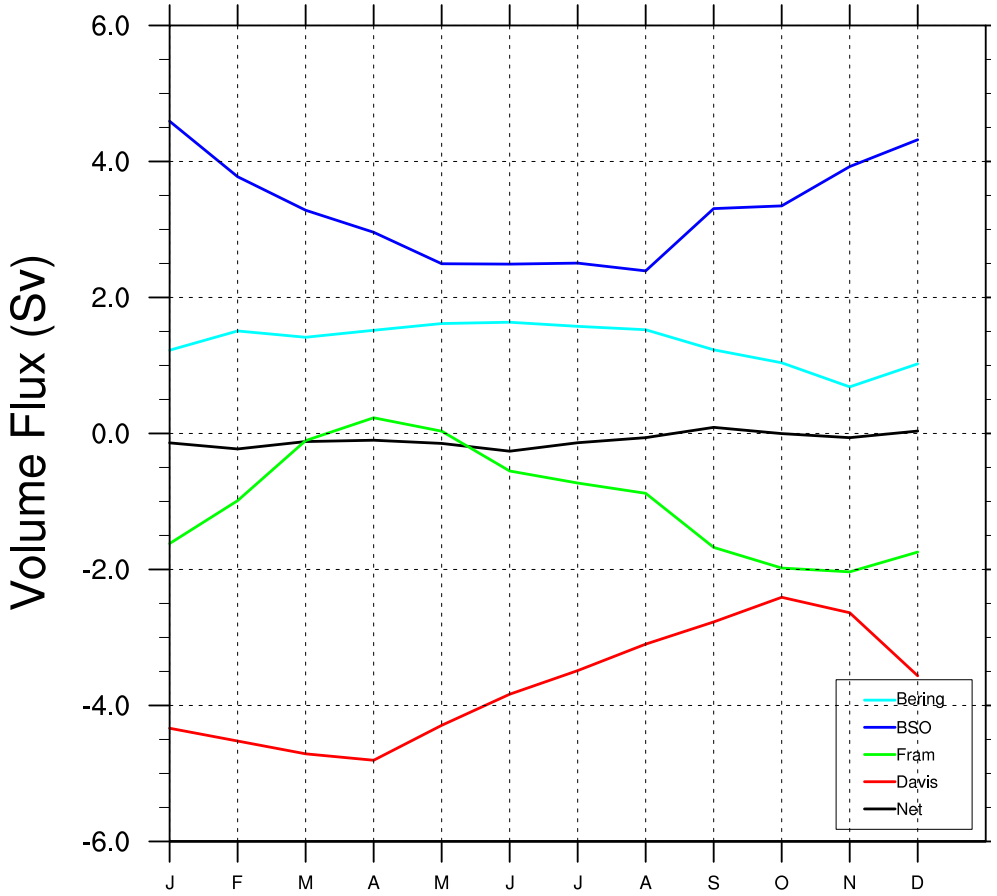

Figure 16: Seasonal cycle of the net volume transport and individual transports through each Arctic gateway obtained from C-GLORS for the period 2004-2010.

and 2005. It should be mentioned though that Curry et al. (2011) calculate their flux estimates using only data from the ocean surface to the depth of the sill (640 m) to the south of the mooring line, because observations suggest that deeper waters from Baffin Bay do not pass this barrier. The literature value is close to the ARCGATE estimate (-2.1 Sv) which suggests that export of volume through Davis Strait is likely overestimated by the reanalysis, although the estimates are based on the same moored array. This might be explained by an inadequate velocity structure in the upper 100 m which account for roughly 40% of the total flux with the WGS contributing a northward transport of 0.4 Sv (Curry et al., 2011). Observation of the upper layer and therefore also the WGS is difficult due to the ice cover and icebergs and has only started in 2004 (Beszczynska-Möller et al., 2011). Therefore, studies using moored observations of previous years were limited to extrapolating fluxes to the upper 150 m, which resulted in volume flux estimates ranging from - 3.3 to - 2.6 Sv (Curry et al., 2011). The cross section plots (Ch. 3.2) will

reveal whether the flux patterns in Davis Strait are represented correctly in the reanalysis or whether an overestimation of southward velocities in the surface ocean can, at least partially, explain the discrepancy between the reanalysis and the observations.

Comparing the seasonal cycle for Davis Strait for the period 2004-2010 (Fig. 16) with the monthly fluxes for October 2004 to September 2005 in Curry et al. (2011, Fig. 4) actually shows a better agreement than the comparison to the ARCGATE period time-series. The maximum export in the reanalysis is found in April (- 4.8 Sv), which is close to the June value in the literature (close to - 5 Sv). The minimum is reached in October in the reanalysis-cycle and in November in the literature, albeit this minimum is close to zero in Curry et al. (2011) as opposed to - 2.5 Sv in the reanalysis.

The long-term estimate (2004 - 2010) for Davis Strait volume export is - 3.7 $\pm$ 0.9 Sv, which is in perfect agreement with the long term estimate (2005 - 2014) of - 3.74 Sv presented by Iovino et al. (2016) for the C-GLORS Version 5 reanalysis. This gives high confidence in the method developed in the framework of this thesis for integrating the volume flux along the irregular line of points (and that appropriate points on the grid are chosen), at least for the case of Davis Strait.

Fram Strait

Although the agreement between ARCGATE and C-GLORS derived timeseries and averages is very good (r = 0.79 and averages of - 1.0 $\pm$ 1.1 Sv versus - 1.1 $\pm$ 1.2 Sv), a short review of the recent literature on Fram Strait shall be presented here, thereby also discussing some interesting features of the circulation in Fram Strait. For Fram Strait, observations date back further in time than in Davis Strait, so that the observation-based seasonal cycle can be compared with the reanalysis based cycle.

Volume fluxes through (parts of) Fram Strait have been estimated for example by Beszczynska-Möller et al. (2012); Fieg et al. (2010); Schauer and Beszczynska–Möller (2009) or Fahrbach et al. (2001) for different periods in time based on moored instruments, vessel-based CTD measurements and model outputs. Fieg et al. (2010) compare volume fluxes based on model output to estimates obtained from a moored array in a similar location as the moorings from the ARCGATE project for the period 1995 to 2005, with fewer instruments before 2002. The authors' estimates of the Fram Strait volume transport for this period are - 1.75 $\pm$ 5.01 Sv based on the moorings, -2.0 $\pm$ 1.26 Sv from a

1/12° resolution model with 50 vertical levels and - 2.16 ± 1.09 Sv from a 1/4° resolution model with 30 vertical levels. Compared to the averages in Table 1 those estimates are lower than the ones calculated both for C-GLORS (short- and long-term) and ARCGATE, but do lie within the uncertainty ranges. The difference between the literature estimate and the average fluxes obtained in this work could partly be explained by the fact that Fieg et al. (2010) calculate volume fluxes directly from velocity measurements by interpolating monthly means of the measured velocities onto a regular grid and multiplying by the grid box area. Thus, there is no constraint in this study concerning pan-Arctic volume conservation.

It is noteworthy that the locations of the moorings in the EGC were shifted southward in 2002 from 79° N to 78.50° N (Fieg et al., 2010). This relocation was necessary because approximately 50% (or 2.6 ± 0.1 Sv) of the total northward transport in the WSC (6.6 ± 0.4 Sv, Beszczynska-Möller et al., 2012) are recirculated just north of 78.50° N. Due to this recirculation the average outflow at 78.50° N is roughly 1.5 Sv larger than at 79° N (de Steur et al., 2014).

Fieg et al. (2010) also study the influence of the model resolution and vertical spacing on the volume flux calculations, finding that the vertical - rather than the horizontal - resolution determines the accuracy of the results. This is based on investigating the difference between subsampling the 1/12° model only at the locations of the moorings but keeping the full vertical resolution (giving a mean flux of -2.04 ± 1.31 Sv) versus limiting the horizontal and vertical resolution to mooring locations and instrument depths, respectively (giving - 3.40 ± 1.42 Sv on average).

The reanalysis based seasonal cycle of Fram Strait volume transport has a maximum in April (roughly 0.3 Sv) and a minimum in October/November (approximately - 2 Sv). The seasonal cycle is weaker than a combination of the observation-based seasonal cycles presented in Beszczynska-Möller et al. (2012) for the WSC for 1997-2010 and in de Steur et al. (2014) for the EGC for 2002-2009. The literature cycle has a minimum export of about 1 Sv during March to May which is mainly driven by high import in the WSC. The export is largest in February (high export in EGC offsetting high imports in WSC by about 4 Sv) and July (low import and low export, again roughly 4 Sv difference).

A tentative explanation for the smaller and temporally shifted extremes compared to the literature is that the reanalysis is not eddy resolving whereas the moorings located (at

best) 7 km apart in WSC are able to capture such signals, at least in this part of Fram Strait (Fieg et al., 2010). The inability of the moorings to capture eddies in the deep part of Fram Strait (distance between moorings up to 30 km) result in large uncertainties of total volume fluxes through the entire strait (Beszczynska-Möller et al., 2011).

Iovino et al. (2016) estimate a net volume flux through Fram Strait of - 0.88 Sv (2005 - 2014 average), which is in good agreement with the long term estimate (2004 - 2010) of - 1.0 ± 1.0 Sv obtained for C-GLORS in this work.

Barent Sea Opening

The BSO volume transport is overestimated in the reanalysis by roughly 1.4 Sv throughout the entire ARCGATE period but the timeseries quite closely resembles that from ARCGATE (r = 0.74). As far as the average is concerned, the ARCGATE average is close (2.3 ± 1.2 Sv) to the estimate from Smedsrud et al. (2010) (2 Sv with a variability[22] of 0.4 Sv) for the period 1997-2007. For the same period, the annual cycle is calculated to have a maximum transport into the Arctic Ocean of 2.8 Sv in January reaching a minimum of 1.3 Sv in April. This annual cycle is qualitatively similar to the reanalysis-based cycle in Figure 16 in that the maximum here is also reached in January. However, the "minimum" is rather a plateau from May to September, whereas Smedsrud et al. (2010) find a non-monotonic increase from April to January. As far as the average is concerned, the long-term average (3.3 ± 1.0 Sv) from the reanalysis is closer to the literature estimate than the short-term average (3.7 ± 1.1 Sv), but still more than one Sverdrup too large.

As pointed out in Smedsrud et al. (2010) the inflow into the Barents Sea is actually 3.2 Sv, but 1.2 Sv exits the BSO through the Bear Island Channel (BIC) (observation based estimate from 09/1978 - 01/1979 from Blindheim, 1989) of which 0.9 Sv flow through the Bear Island Trough (observation based estimate for 2003 - 2005 from Skagseth, 2008). A possible explanation for the overestimation of the net flow through the BSO therefore is that the reanalysis does not capture this outflow current sufficiently well (see Ch. 3.2).

The long-term estimate for the volume flux through the BSO obtained in this work (3.3 ± 1.0 Sv) agrees very well with the 3.40 Sv estimated by Iovino et al. (2016) for C-GLORS Version 5.

[22] Calculated from Smedsrud et al. (2010, Tab. 1).

Bering Strait

Similar to Fram Strait, Bering Strait timeseries and averages yield satisfactory results compared to the ARCGATE derived estimates, but still a literature review gives interesting insight in details of Bering Strait transports and also allows for a comparison between observation- and reanalysis based seasonal cycles.

Woodgate and Aagaard (2005) estimate an annual average of the volume transport through Bering Strait based on long-term measurements between 1990 and 2004 in one mooring site in the center of the strait. The flow through this mooring site is believed to capture the combined flows through the western and eastern channels of the Bering Strait sufficiently well to calculate representative volume and heat flux estimates for the entire strait. The mean annual volume flux estimate is 0.8 Sv with roughly 25% uncertainty (i.e. 0.2 Sv). This uncertainty accounts for the fact that the entire column transport is estimated from one measurement location 9 m above the bottom, as well as for the neglect of boundary currents. The C-GLORS annual average for the ARCGATE period is higher (1.2 ± 0.5 Sv) than this literature value even though the two values agree with each other within their uncertainty ranges. It is reassuring, if not surprising, that the ARCGATE estimate is close (0.7 ± 0.7 Sv) to the literature estimate. The ARCGATE estimates are based on the two mooring sites in the eastern and western channel and estimates in Woodgate and Aagaard (2005) are based on the mooring in the center which is said to capture the combined flux through the two other moorings.

Woodgate and Aagaard (2005) also calculate the climatological annual cycle of volume transports through Bering Strait from the same measurements. The authors estimate that the volume flux increases steadily from 0.4 Sv in January to 1.3 Sv in June and then decreases again, although non-monotonically, to 0.5 Sv in December (Woodgate and Aagaard, 2005, Tab. 1). The seasonal cycle of Bering Strait volume transports derived from C-GLORS (Fig. 16) qualitatively resembles the seasonal cycle from the literature. However, the minimum is reached already in November (0.7 Sv), increasing from then on to the maximum in June (1.63 Sv).

Woodgate et al. (2010, Fig. 3) show transports through the same mooring site as described above for years of extreme heat fluxes, namely extremely low flux years (2001 and 2005) and extremely high flux years (2004 and 2007). Comparing the volume transport during the five months (September 2005 to January 2006) at the end of 2005 to

the first five months in Figure 15 reveals good agremment in the general behaviour until November, but afterwards the C-GLORS flux increases while the observation-based flux stays negative at least until January 2006. Again, it is not surprising that the ARCGATE timeseries during those five months shows a similar behaviour to the literature.

The 1.3 $\pm$ 0.3 Sv long-term estimated from C-GLORS in this work are in very good agreement with the 1.4 Sv estimate (for the period 1982 - 2012) presented in Storto et al. (2016, Fig. 13) and the 1.29 Sv (2005 - 2014 average) estimated by Iovino et al. (2016) for C-GLORS Versions 4 and 5, respectively.

3.1.3 Heat Transports

Second, the time series of heat fluxes referenced to $\theta_{ref} = 0°$ C from C-GLORS are compared with time series of ARCGATE-derived heat fluxes, which are based on monthly θ and velocity fields using the same constants and reference temperatures as for C-GLORS. As explained in Chapter 1.6, the same reference temperature needs to be used, even for the net heat flux through the Arctic gateways, because the surface volume flux is not equal to zero (i.e. the oceanic fluxes through the straits do not compensate each other).

Figure 17 shows the heat fluxes through each strait and the net heat flux for C-GLORS and ARCGATE. The "stationary" C-GLORS heat fluxes ($\bar{T}\bar{v}$) are based on monthly temperature and velocity fields. The "eddy" C-GLORS heat fluxes ($\overline{T'v'}$) are the difference between the total heat flux ($\overline{Tv}$, calculated form daily temperature and velocity fields and then averaged for each month) and the "stationary" heat flux.

There seems to be very good agreement between Bering Strait heat fluxes from C-GLORS and ARCGATE, with the averages (see Tab. 2) even being equal to each other and a high correlation of 0.91 and RMSD = 6 TW. The net heat transport is also captured well by the reanalysis, with C-GLORS averages falling within the ARCGATE uncertainty range and a correlation of 0.87. The largest discrepancy is found in Davis (RMSD = 25 TW) and Fram Strait (RMSD = 30 TW), the latter being somewhat surprising considering the good agreement between the observation- and reanalysis-based volume transports in Fram Strait. This might be explained through differences in the temperature cross sections in Fram Strait. The BSO heat flux seems to be overestimated by the reanalysis, while the transports through Fram and Davis Strait are apparently underestimated.

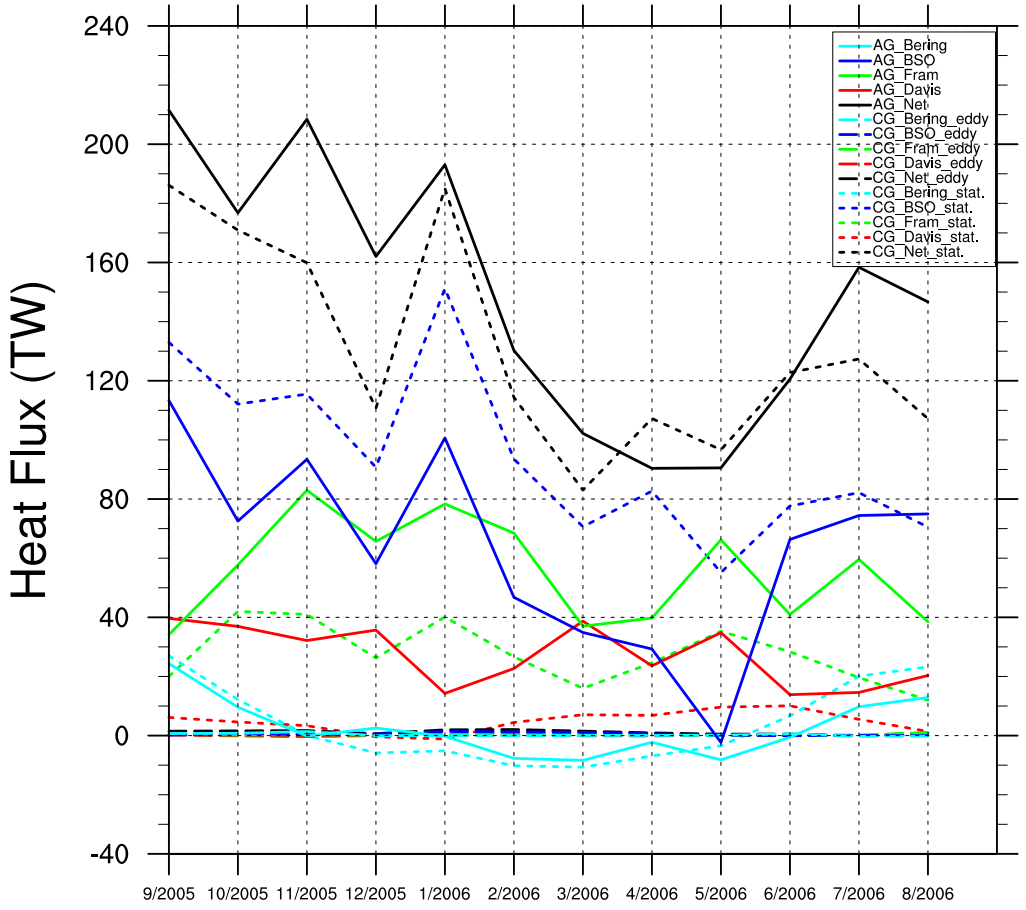

Figure 17: Heat Flux in TW through Davis, Fram, Bering Strait, the BSO and net flux into the Arctic for C-GLORS and ARCGATE for the ARCGATE period. C-GLORS "stationary" heat fluxes (dotted line) and C-GLORS "eddy" heat fluxes (dashed line) are shown. The sum of those two would give the total heat flux.

The absolute values of the net heat fluxes can actually be compared - although with some caution - since the total volume flux is almost zero (avg = - 0.1 Sv) through all four straits both in C-GLORS and ARCGATE. However, since the monthly volume fluxes do differ and are unequal to zero, even the net heat flux depends on the choice of the reference temperature. The comparison of temperature and velocity cross sections will give a better insight into agreements and discrepancies between the C-GLORS and ARCGATE heat fluxes for the individual gateways.

Figure 17 and Table 2 reveal that the contribution of transient eddies to the total heat flux is small (less than 10% in each strait). Heat transports at those high latitudes are therefore dominated by the stationary circulation and stationary eddies. This conclusion is in line with the findings presented in Valdivieso et al. (2014). The largest absolute

Strait	C-GLORS AG period ("stationary")	ARCGATE AG period	C-GLORS AG period ("eddy ")	r	RMSD	C-GLORS 2004-2010 ("stationary")
Davis	5 ± 4	27 ± 10	-0.0 ± 0.1	0.10	25	5 ± 4
Fram	28 ± 10	56 ± 17	0.4 ± 0.3	0.73	30	24 ± 10
BSO	95 ± 28	64 ± 33	0.5 ± 0.5	0.80	36	80 ± 25
Bering	4 ± 14	3 ± 10	0.3 ± 0.5	0.91	6	5 ± 15
Net	131 ± 35	149 ± 43	1.2 ± 0.7	0.87	28	114 ± 30

Table 2: Average heat fluxes in TW for C-GLORS and ARCGATE for the ARCGATE period (AG period) and for 2004-2010 for C-GLORS. The contribution of transient eddies to the total heat flux (not shown here) is quantified as well for the ARCGATE period. Cross correlation coefficient r and RMSD between C-GLORS and ARCGATE timeseries during the ARCGATE period. "Uncertainties" are standard deviations from the averages and are solely due to variability. All units are TW except for r (unitless).

contribution is found in the BSO and the largest relative contribution in Bering Strait (< 7 %).

3.2 Cross Sections

As explained previously in Chapter 2.3.3 heat flux cross sections for C-GLORS and ARCGATE are calculated based on monthly potential temperature and velocity fields, because no higher temporal resolution is available from the ARCGATE dataset. Distances in the cross section plots are calculated from the coast to the latitude/longitude of the black ARCGATE points in Figures 11 - 14 for each strait. Positive velocities signify Arctic inflow and point into the paper.

The time series plots in this section are based on the cross section plots: Monthly heat and volume transports are the sums over the entire cross section of heat flux (in W/m^2) and velocity each multiplied by the length of the ARCGATE section corresponding to each black point in Figures 11 - 14 (effectively, those are the distances between the green points to the left and right of each black point) and theoretically by the vertical level thickness, which is 1 dbar in this case. Due to zero length corresponding to some points in the BSO

and Bering Strait (see Ch. 2.3.3) those values can not be included in the cross section sum, thus representing one possible error in the calculations. Additionally, those sums are based on horizontally interpolated values for ARCGATE and vertically interpolated values in C-GLORS which adds another possible source of error to the integrated heat and volume transports. However it should be pointed out that these interpolations do not change the patterns of the cross sections. A third error might be introduced by interpolating C-GLORS u velocities onto the v-grid and vice versa and by subsequently projecting the C-GLORS velocity vector onto the ARCGATE-line normal vector.

The net C-GLORS volume flux integrated along the irregular line (as done for the timeseries plots in Chapter 3.1) is - 0.05 $\pm$ 0.22 Sv while the net flux derived from the cross-section sums is - 0.38 $\pm$ 0.31 Sv. Both are averaged over the ARCGATE period and uncertainties are the standard deviation of monthly averages from this mean. As a comparison, the given net volume flux from ARCGATE and the one obtained by summing over all cross sections are - 0.14 $\pm$ 0.06 Sv versus - 1.06 $\pm$ 0.24 Sv with the main discrepancy in Fram Strait (- 1.1 $\pm$ 1.2 Sv versus - 1.8 $\pm$ 1.2 Sv) due to the fact that the westernmost part of the strait with strong northward volume transport all year round is almost "lost" to the horizontal interpolation. Bearing in mind that the focus in this chapter is not on the absolute values of heat and volume transports but rather on investigating the patterns of those fluxes (which are not affected by any attempt to correct the volume flux) the difference between the two net fluxes is not added to the cross section sums.

Davis Strait

The strait with the largest discrepancy in volume and heat transports is Davis Strait. Figures 18 - 20 show the cross section plots of temperature (° C), velocity (in m/s) and heat flux (in 10^6 W/m^2) averaged over the period December 2005 to April 2006 and the differences between the respective fields (ARCGATE minus C-GLORS). Figs. 21 - 23 show similar plots for the remaining months of the ARCGATE period. The ARCGATE year is separated into "winter" and "summer - fall" during which temperature and velocity patterns are similar but with large differences in between the two periods. Distances (x-axis of the plots) are calculated with respect to 66.6 °N and 61.3 °W. Quantification of volume (Sv) and heat (in TW) fluxes, which are the sums over the entire cross section, as well as cross-section average temperatures and the anomaly pattern correlations between

ARCGATE and C-GLORS can be found in Table 3 for three different periods.

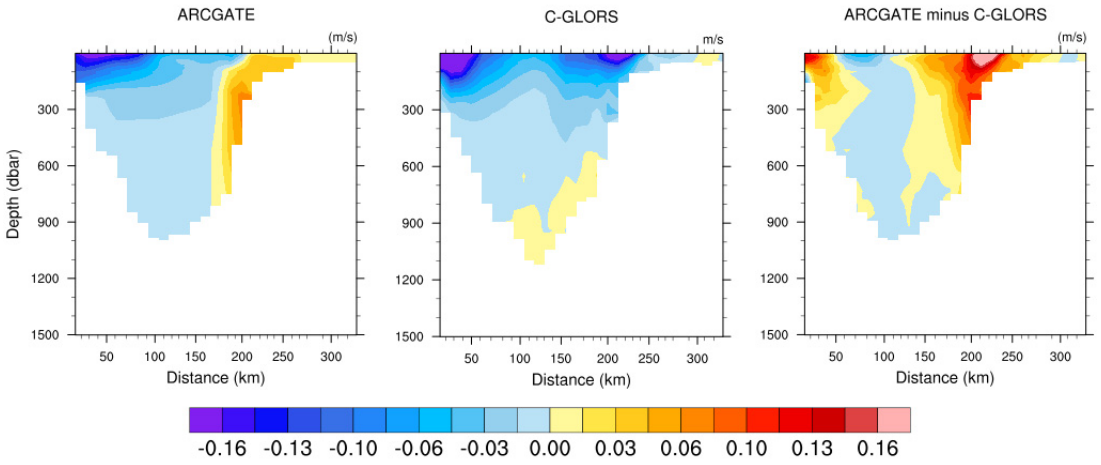

Figure 18: Davis Strait velocity cross sections averaged over December 2005 to April 2006 (winter period) for ARCGATE and C-GLORS.

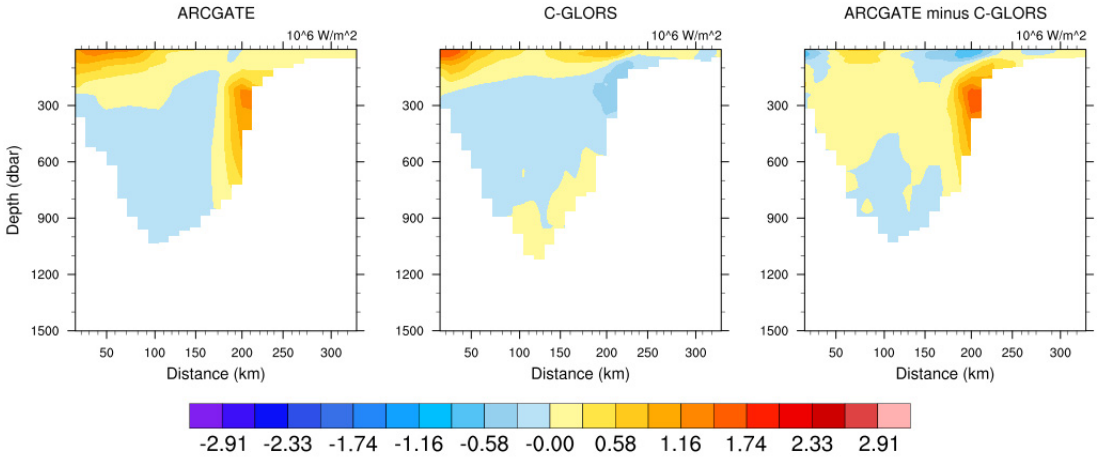

Figure 19: Davis Strait heat flux cross sections for the winter period. Both are derived from monthly potential temperature and velocity fields, referenced to $\theta_{ref} = 0\,^{\circ}C$.

Considering the heat flux (or temperature transport) distribution across Davis Strait from ARCGATE and C-GLORS datasets shows a qualitatively good agreement of the patterns especially for the summer-fall period. The anomaly pattern correlation is low due to the uniformity of heat transports in the deeper part of the strait in ARCGATE while there is some pattern in C-GLORS leading to a negative correlation in this area

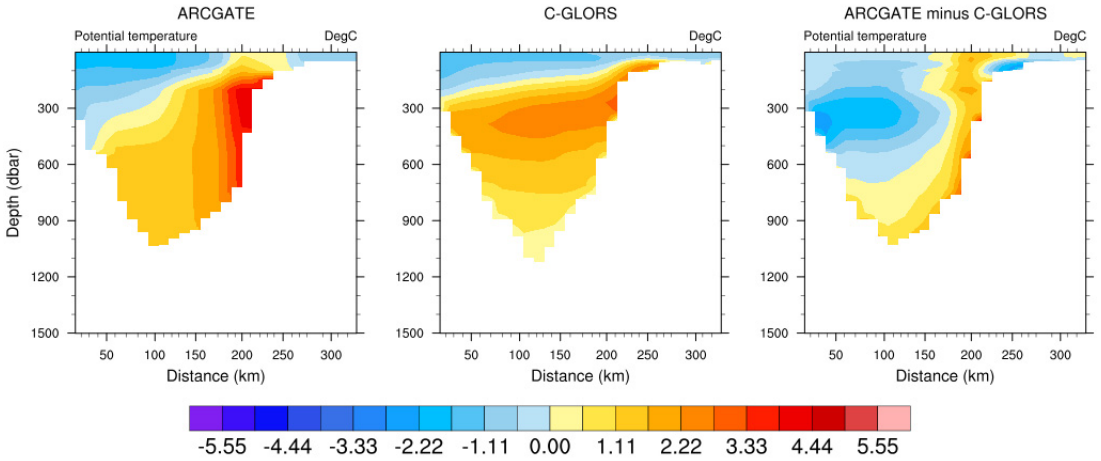

Figure 20: Davis Strait potential temperature cross sections for the winter period.

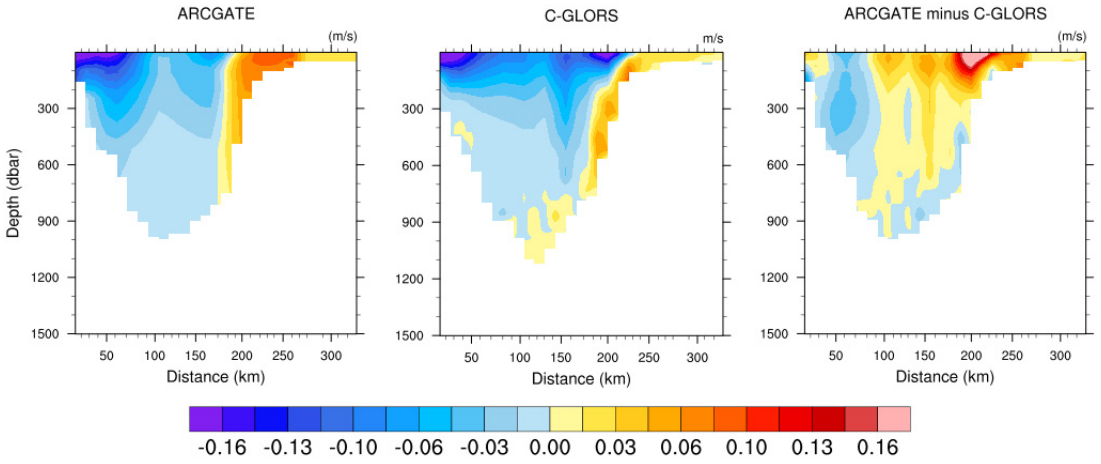

Figure 21: Davis Strait velocity cross sections averaged over May 2006 “to“ November 2005 (summer - fall period) for ARCGATE and C-GLORS.

(similar to Bering Strait temperature correlation, see below). There is a heat import over the West Greenland Shelf (WGS) and along the slope in both datasets during this time, although this transport is less pronounced in C-GLORS and disappears during the winter period while it prevails in ARCGATE throughout the year. The heat transport patterns in central and western Davis Strait are similar in C-GLORS and ARCGATE for both periods.

Figure 24 shows the monthly cross-section average temperatures as well as volume and

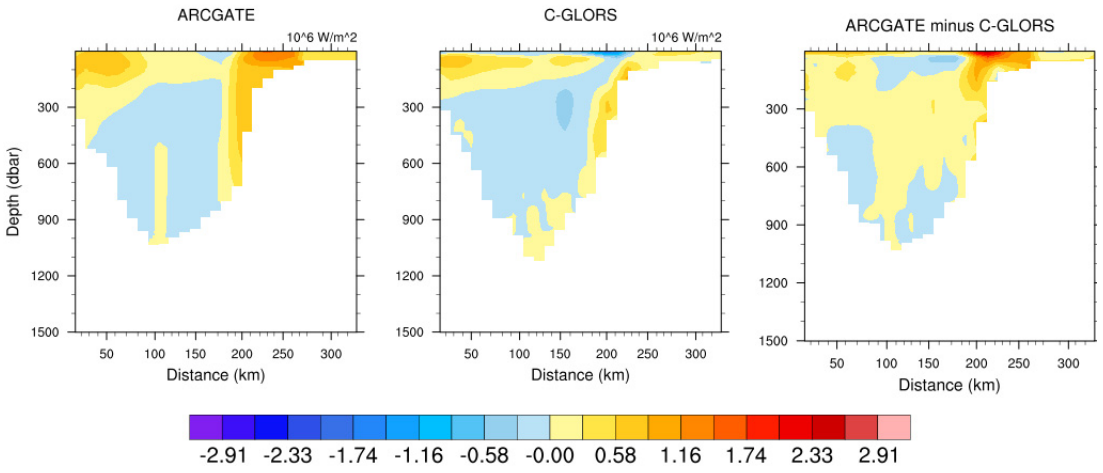

Figure 22: Davis Strait heat flux cross sections for the summer - fall period.

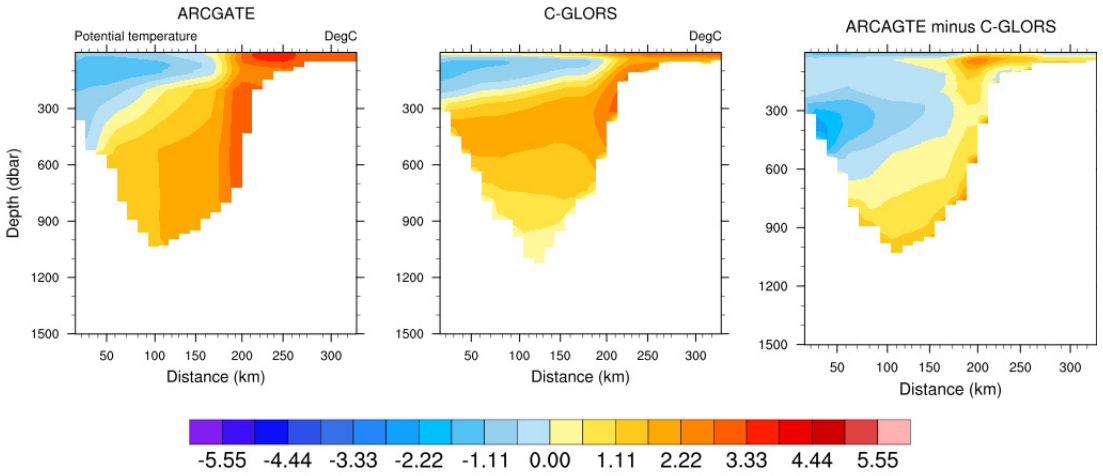

Figure 23: Davis Strait potential temperature cross sections for the summer - fall period.

heat fluxes for C-GLORS and ARCGATE. This plot suggests that the main discrepancy in heat fluxes is attributable to differences in the total volume transport through Davis Strait, since average temperatures agree quite well. However, the total heat flux does not only depend on the cross section average but on the distribution of temperature and velocities across the section.

There is good agreement between the C-GLORS and ARCGATE temperature and heat flux distributions for both periods with better agreement for the summer-fall period. One can see from the ARCGATE temperature plots that temperatures are set constant to the value at 500 m down to the ocean bottom due to the lack of data. The WGS region

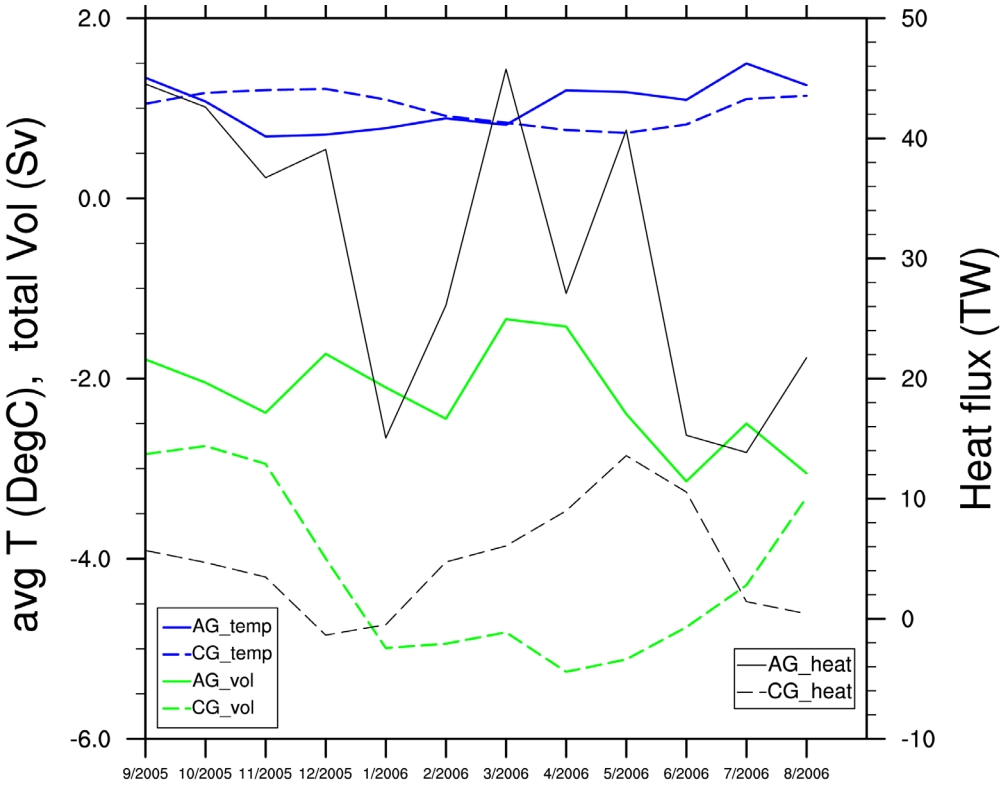

Figure 24: ARCGATE period averages of integrated volume (green) and heat (black) fluxes for Davis Strait for C-GLORS (dashed) and ARCGATE (solid). Cross-section averages of potential temperatures are shown in blue. The timeseries presented here (and also for the followig straits) are similar to those in Figures 15 and 17.

and the majority of the deep waters (below 300 m) is warm, more so in ARCGATE than C-GLORS. A cold region starting from Baffin Island and reaching roughly 200 km into the strait is found both in the reanalysis and observation based datasets for the summer-fall period. In the same area there are strong southward currents in both datasets resulting in a positive heat flux in this area. Additionally, there is a strong southward current at around 200 km distance in C-GLORS in a region of positive temperatures, resulting in a strong negative heat flux whereas ARCGATE has warm water and northward currents in the region. The volume flux difference in this area partly explains the heat flux discrepancy during the summer-fall period. Aside from that, temperatures and velocities are smaller in C-GLORS than in ARCGATE especially in the WGS region (including the slope), so that the overall heat flux is underestimated by the reanalysis. The average volume flux for the summer-fall period from 200 km distance to the eastern end of Davis Strait is 1.4 ± 0.7 Sv in ARCGATE and 0.3 ± 0.4 Sv in C-GLORS which reflect the contribution

of the negative velocities at 200 km and of the overall smaller positive velocities in the WGS region. This C-GLORS estimate for the entire shelf region including the slope is as small as the estimate of 0.4 Sv given by Curry et al. (2011) for only the shelf without the slope, further supporting the hypothesis that the reanalysis underestimates northward volume transport in the eastern part of Davis Strait.

In the winter period, the entire upper 100 m are cold in C-GLORS, while there is clearly an area of warm waters in the ARCGATE dataset at around 200 km distance. In this region there is a northward current in ARCGATE, resulting in a positive heat transport. The C-GLORS dataset also shows a positive heat flux here during winter, but in this case it is the result of a strong southward current and negative temperatures. Therefore, the differences in temperature and velocity between C-GLORS and ARCGATE compensate each other in this area. However due to the positive temperatures below 100 m in the entire strait except for the westernmost regions combined with the negative volume transports, heat transports are negative in C-GLORS in the WGS region (including the slope), while the opposite is true for ARCGATE due to positive velocities and warm water in this area. From 200 km to the coast of Greenland the average ARCGATE volume flux in the winter period is 1.0 $\pm$ 0.5 Sv contrasting the - 1.1 $\pm$ 0.5 Sv C-GLORS estimate.

A test for the methods used in this thesis is to compare the ARCGATE period average fluxes calculated from the cross sections to the averages given in Tsubouchi et al. (2016): Davis Strait volume transport is - 2.1 $\pm$ 0.7 Sv for the entire strait due to - 3.2 $\pm$ 0.6 Sv outflow west of 58°W and 1.2 $\pm$ 0.8 Sv inflow east of 58°W in the literature. In this thesis the ARCGATE estimate of the Baffin Island Current to the west of 57°W (west of 200 km distance) is - 3.4 $\pm$ 0.7 Sv and east of this point in the WGC the estimate is 1.2 $\pm$ 0.7 Sv resulting in a total transport of - 2.2 $\pm$ 0.6 Sv all of which are in perfect agreement with the literature estimates. As far as the heat flux is concerned, Tsubouchi et al. (2016) present an estimate of 29 $\pm$ 10 TW referenced to - 0.1° C, which is almost equal to the heat flux estimate from this work (31 $\pm$ 12 TW).

As an additional validation, the monthly cross section plots for temperature and velocity (not shown here) from C-GLORS and ARCGATE are compared (qualitatively) with the plots for October 2004 to August 2005 in Curry et al. (2011). The temperature plots from both datasets are similar to those found in the literature, but velocity structures from ARCGATE are clearly more like those in Curry et al. (2011) than the C-GLORS

velocity profiles are. This is mainly due to the aforementioned region of southward currents in C-GLORS located at approximately 200 km distance. This feature shifts to the west from 200 - 250 km between September and March to 150 - 200 km for the rest of the ARCGATE period.

	1) ARCGATE Period			**RMSD**		
	AG	**CG**	Pattern C.	**1)**	**2)**	**3)**
Heat (TW)	31 ± 12	5 ± 5	0.38 ± 0.15	28	29	28
Vol (Sv)	- 2.2 ± 0.6	- 4.2 ± 1.0	0.51 ± 0.13	2.2	3.1	1.5
T (°C)	1.0 ± 1.5 (0.3)	1.0 ± 1.1 (0.2)	0.68 ± 0.09	0.3	0.3	0.3
	2) Dec. - Apr.			**3) May. - Nov**		
	AG	**CG**	Pattern C.	**AG**	**CG**	Pattern C.
Heat (TW)	31 ± 12	4 ± 4	0.32 ± 0.16	31 ± 13	6 ± 5	0.41 ± 0.14
Vol (Sv)	- 1.8 ± 0.5	- 4.8 ± 0.5	0.52 ± 0.15	- 2.5 ± 0.5	- 3.7 ± 1.0	0.51 ± 0.12
T (°C)	0.9 ± 1.5	1.0 ± 1.2	0.64 ± 0.08	1.2 ± 1.4	1.0 ± 1.1	0.70 ± 0.08
T var (°C)	(0.2)	(0.2)		(0.3)	(0.2)	

Table 3: Davis Strait heat and volume fluxes (sum over cross section) for the averages over 1) ARCGATE period, 2) Dec. - Apr. and 3) May - Nov. In the temperature row, period averages of the monthly spatial cross section average are given. For temperature, the uncertainties are period-averages of the standard deviation from the monthly spatial average and values in brackets are stddev of the temporal variability. For heat and volume fluxes the "uncertainties" are standard deviations of monthly averages from the period-average. For each quantity the average of monthly anomaly pattern correlations ± temporal standard deviations are given as well, including the temporal standard deviations. Additionally, RMSDs for each period are given.

Fram Strait

Figures 25 - 27 show the ARCGATE period average cross section plots for velocity, heat flux (W/m^2) and temperature for C-GLORS and ARCGATE. Distances are calculated with respect to 78.82 °N and 20.6 °W. Figure 28 shows the cross-section average temperature, volume flux and heat flux for each month of the ARCGATE period. This plot suggests that most of the heat flux discrepancy can be attributed to differences in the

volume fluxes. Since temperature, velocity and heat flux patterns do not show any clear seasonality and do not vary considerably throughout the ARCGATE period the cross section plots are only shown for the average over the entire period.

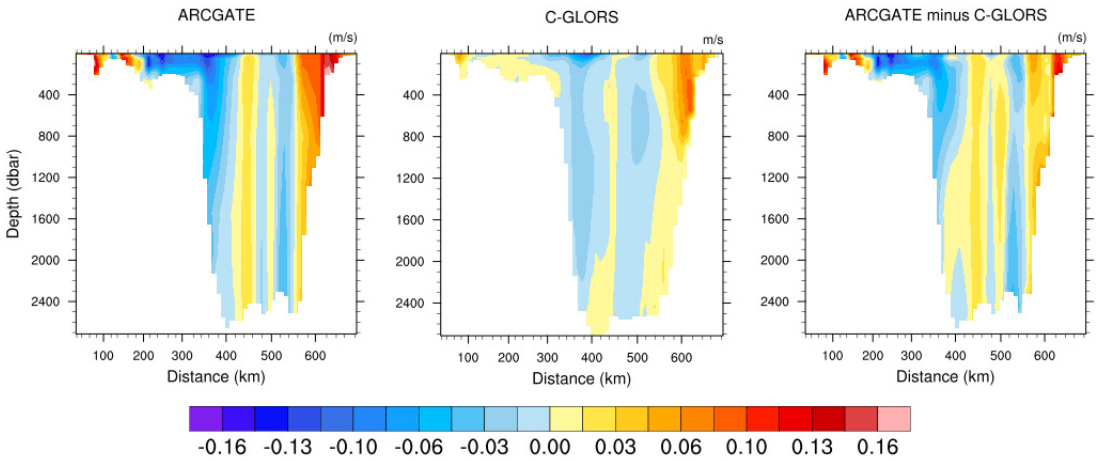

Figure 25: Fram Strait velocity cross sections averaged over the entire ARCGATE period for ARCGATE and C-GLORS.

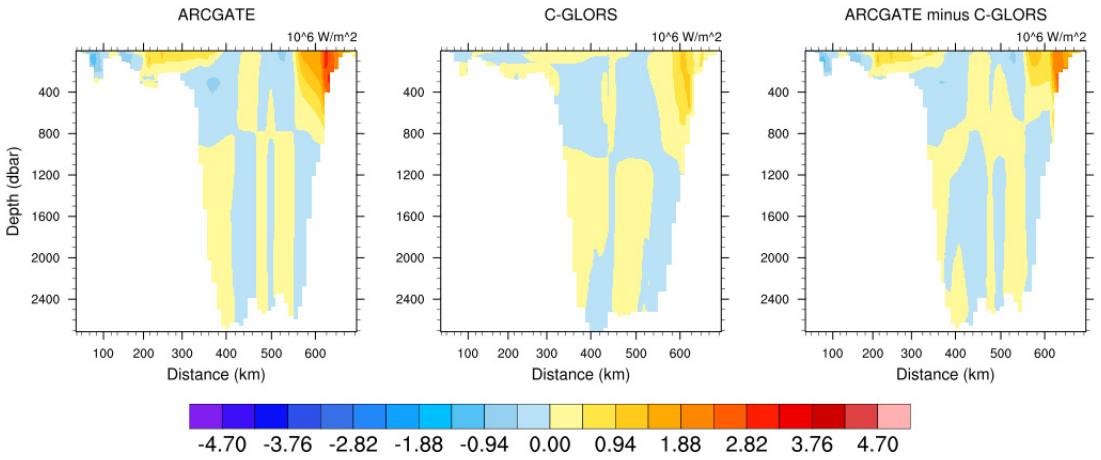

Figure 26: Fram Strait heat flux cross sections averaged over the entire ARCGATE period.

Temperature anomaly pattern correlations are high in Fram Strait and intermediate for heat flux and velocity patterns (see Table 4). The cross section temperature pattern is therefore very similar in the two datasets, but temperature extremes are greater in

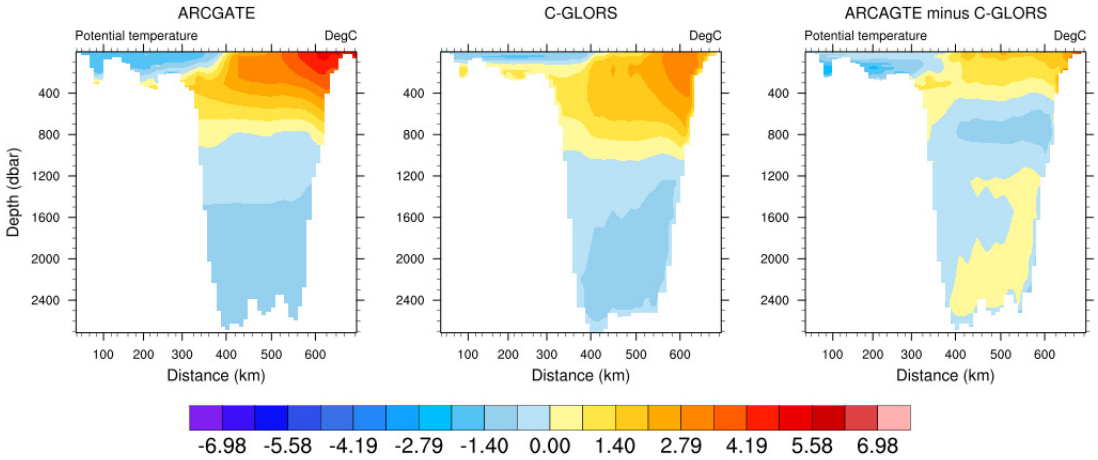

Figure 27: Fram Strait potential temperature cross sections averaged over the entire ARCGATE period.

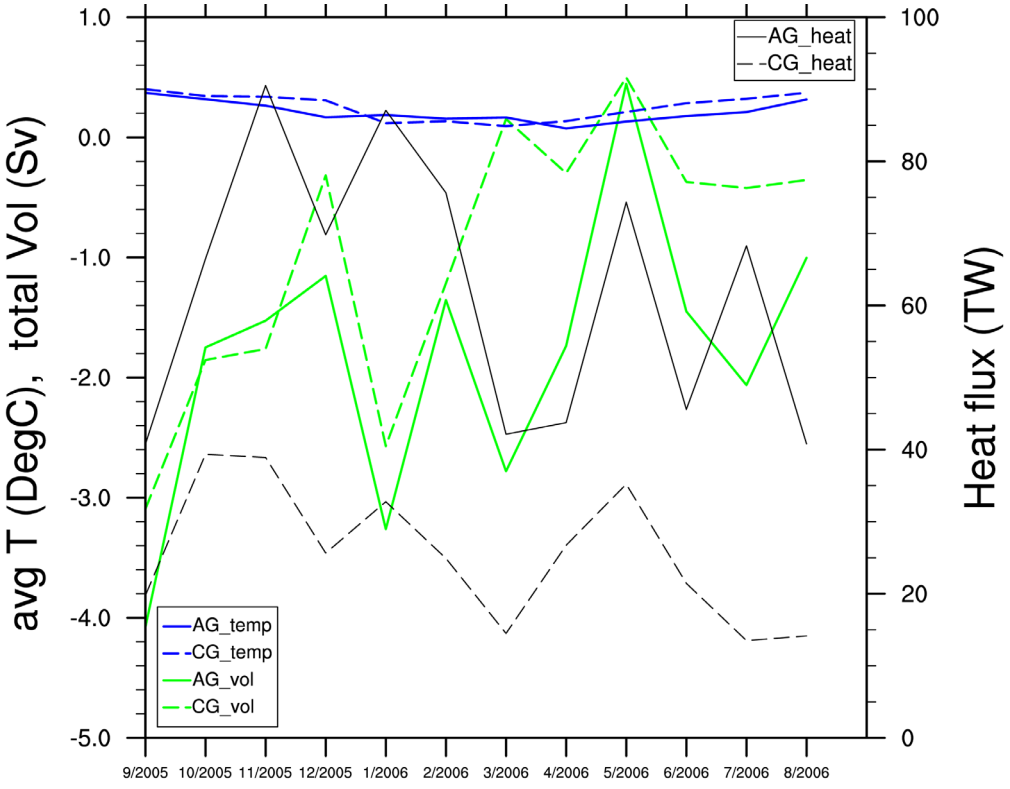

Figure 28: ARCGATE period averages of integrated volume (green) and heat (black) fluxes for Fram Strait for C-GLORS (dashed) and ARCGATE (solid). Cross-section averages of potential temperatures are shown in blue.

ARCGATE than C-GLORS. Average temperatures are very similar in C-GLORS and ARCGATE throughout the year both for the whole cross section and for the three parts of deep Fram Strait (see Table 4). The only difference in the temperature patterns is that cold waters cover a greater area over Belgica Bank in ARCGATE than in C-GLORS. Cross section average temperatures are stable throughout the year and so is the spatial distribution of warm ($\theta > 0°$ C) and cold ($\theta < 0°$ C) waters.

	Fram Strait				**Bel. B.**	
	AG	**CG**	Pattern C.	RMSD	**AG**	**CG**
H (TW)	62 ± 19	26 ± 9	0.57 ± 0.15	39	0.6 ± 2.2	- 0.50 ± 0.46
V (Sv)	- 1.8 ± 1.2	- 1.0 ± 1.1	0.53 ± 0.15	1.2	- 0.55 ± 0.44	0.21 ± 0.14
T (°C)	0.2 ± 1.5 (0.09)	0.3 ± 1.2 (0.11)	0.90 ± 0.01	0.1	- 1.18 ± 0.05	0.43 ± 0.02
	EGC		**CEN**		**WSC**	
	AG	**CG**	**AG**	**CG**	**AG**	**CG**
H (TW)	- 3 ± 6	2 ± 1	- 2 ± 9	- 4 ± 4	67 ± 12	28 ± 10
V (Sv)	- 6.1 ± 1.2	- 2.77 ± 0.97	- 1.6 ± 2.0	- 1.79 ± 0.97	6.43 ± 0.94	3.4 ± 1.1
T (°C)	-0.02 ± 0.10	0.03 ± 0.06	0.15 ± 0.09	0.08 ± 0.11	1.00 ± 0.19	0.77 ± 0.14

Table 4: Heat and volume fluxes averaged over the ARCGATE period for the entire Fram Strait and the partial sections over Belgica Bank, EGC, Central Fram Strait (CEN) and the WSC. Uncertainties are standard deviations of monthly means from the period average. (Partial) cross-section average temperatures are given with spatial standard deviations, and temporal standard deviations in brackets. For the entire Fram Strait, temperature, heat and velocity pattern anomaly correlations are given including temporal stddevs as well as the RMSDs.

Overall there is good agreement between C-GLORS and ARCGATE velocity and heat flux structures in Fram Strait with import of warm waters on the eastern end of the strait in the region of the WSC (550 - 685 km or east of 5°E) and export of cold waters in the western part of deep Fram Strait in the EGC (305 - 400 km or 6.5°W to 2°W). However, both northward and southward volume transports are each roughly 3 Sv stronger in ARCGATE than in C-GLORS so that the differences largely compensate each other (see Table 4). In central Fram Strait (410 - 540 km, 2°W to 5°E) the volume fluxes are very similar although slightly more negative on average in ARCGATE than in C-GLORS. The

discrepancy between the volume transports is mainly attributable to the difference in velocities over Belgica Bank (0 - 300 km, west of 6.5°W). While ARCGATE velocities are negative throughout the year in the eastern and middle parts of the shelf, C-GLORS velocities are close to zero or positive in this region. ARCGATE heat fluxes are positive due to export of cold waters, whereas C-GLORS heat fluxes are slightly positive over the entire bank.

The larger heat flux in ARCGATE compared to C-GLORS and the differences in the volume fluxes can probably partly be attributed to the higher horizontal resolution of the ARCGATE array, especially in the WSC, compared to the model grid. In the EGC, the reanalysis might not capture the entire wind driven recirculation (see Chapter 3.1) thus resulting in a smaller export.

Again, as a means of validating the methods used in this thesis the ARCGATE fluxes given in Tsubouchi et al. (2016) are compared to the ones calculated in this work. The literature estimates for the ARCGATE period are - 6.2 ± 1.2 Sv for the EGC, 7.4 ± 1.0 Sv for the WSC, - 0.4 ± 0.5 Sv over Belgica Bank and a total volume transport of - 1.1 ± 1.2 Sv through Fram Strait. With the same definitions of EGC, WSC and Belgica Bank, the ARCGATE estimates obtained from this work are - 6.1 ± 1.2 Sv, 6.4 ± 0.9 Sv, - 0.6 ± 0.4 Sv and - 1.8 ± 1.2 Sv in the same order as before. For most parts the agreement is very good between those estimates which supports the results from this work. The difference in the total transport has already been explained in the beginning of this chapter. The fact that the import by the WSC is underrepresented in this work compared to the literature might be due to the horizontal interpolation of ARCGATE data in the course of preparing the cross sections and to a slightly different choice of the limits chosen to define the WSC[23]. Tsubouchi et al. (2016) present a heat flux (or rather, temperature transport) estimate for the WSC of 58 ± 10 TW referenced to 0.1° C, which is lower than the 67 ± 12 TW calculated in this thesis. However, both volume and heat flux estimates agree with the literature values within the uncertainty range. It should be pointed out that the "uncertainty range" of the estimates from this work are actually standard deviations of the monthly means whereas the literature uncertainties are uncertainties based on the method, simplifications and instrumental uncertainties. Additionally, ARCGATE

[23] Close to 550 km or 5°E there is a strong shear between northward and southward currents, so that if in the literature the western limit of the WSC is set a bit further to the East than in this work, this can yield a much larger northward flux.

velocity and temperature cross sections are in perfect agreement with the plots presented by Beszczynska-Möller et al. (2012, Fig. 2) for the 2002 to 2008 period.

Barents Sea Opening

Figure 33 shows the C-GLORS and ARCGATE temperature cross sections averaged over the ARCGATE period. Due to seasonal differences in the velocity pattern heat flux and velocity cross sections are averaged over the period from January to June (Figs. 29 and 30) and from July to December (Figs. 31 and 32). Distances in the plots are calculated with respect to 77.53 °N, 18.09 °E. Quantification of the fluxes and average temperatures for the BSO are found in Table 5.

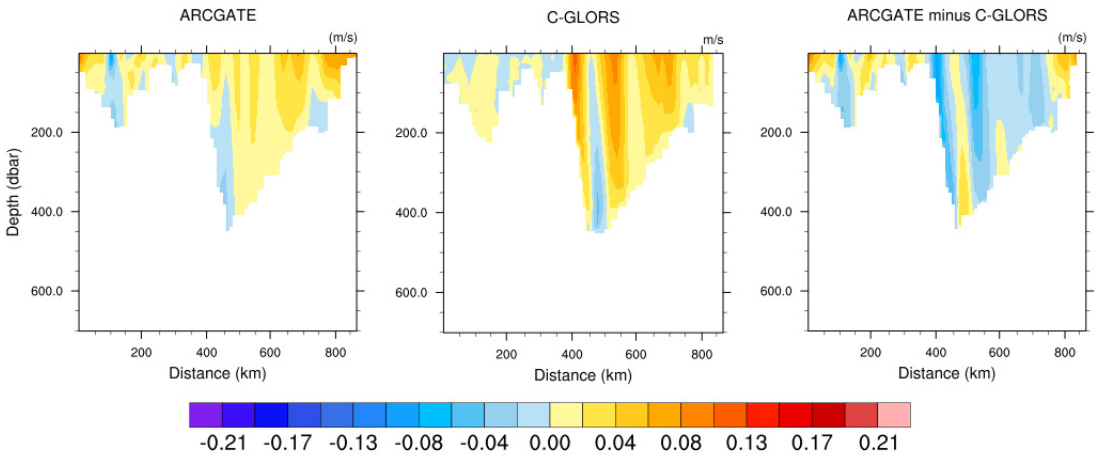

Figure 29: Barents Sea Opening velocity cross sections averaged over January 2006 to June 2006 for ARCGATE and C-GLORS.

Figure 34 suggests that the main discrepancy in the heat fluxes can be explained by the difference in the volume fluxes rather than by differences in the temperature distribution. This is in line with Årthun et al. (2012) who find that about 70 % of anomalously high heat transport through the BSO in 2005 (and 2008) are attributable to anomalously high volume transports and the rest to anomalous temperatures. The C-GLORS volume flux is overestimated for all months except for July and August whereas the cross section averages of temperatures are similar in ARCGATE and C-GLORS (see Table 5). Temperature anomaly pattern correlations are very high for the entire ARCGATE period.

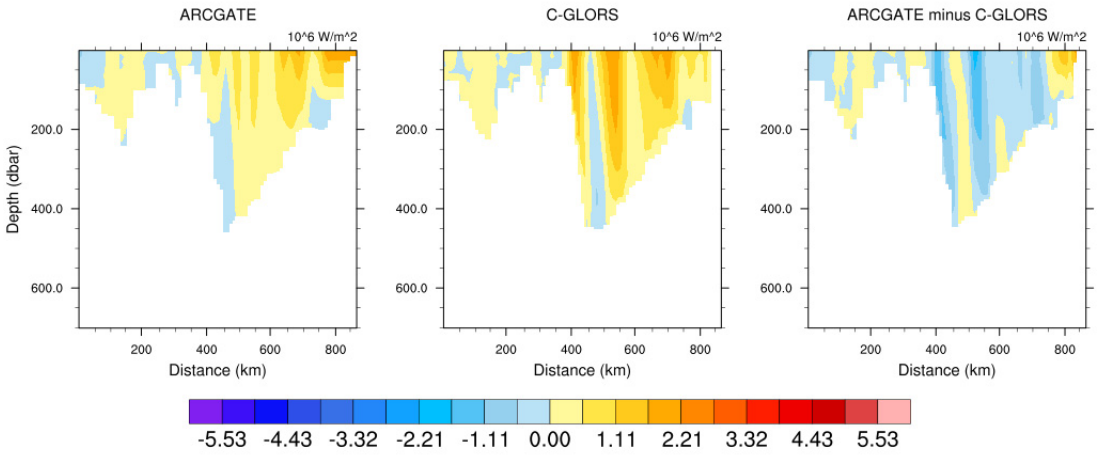

Figure 30: Barents Sea Opening heat flux cross sections averaged over January 2006 to June 2006. Both are derived from monthly potential temperature and velocity fields, referenced to $\theta_{ref} = 0\ ^{\circ}C$.

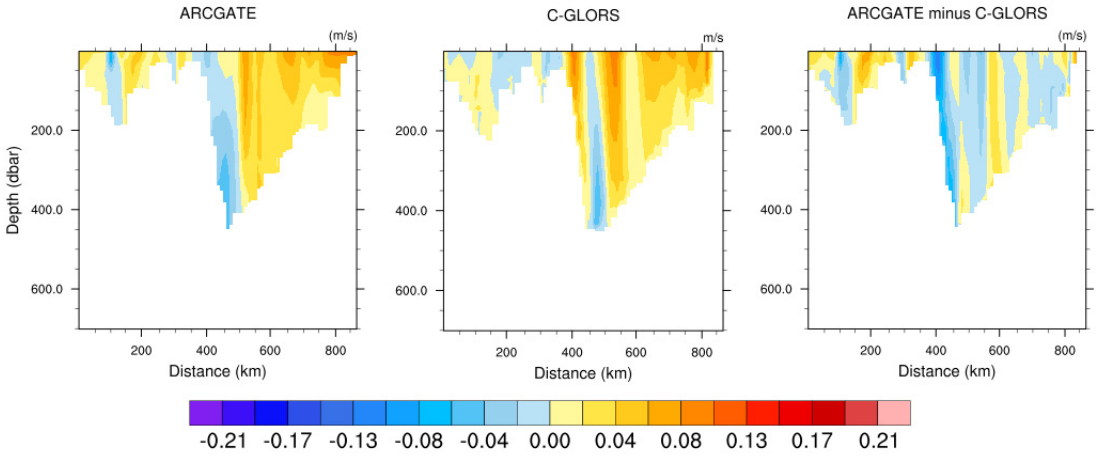

Figure 31: Barents Sea Opening velocity cross sections averaged over July 2006 “to“ December 2005 for ARCGATE and C-GLORS.

The velocity cross sections (Figs. 29 and 31) show good agreement of the general velocity pattern for most of the strait but higher import in the reanalysis in both periods. Especially in the Bear Island Current (BIC = 360 - 470 km, 74.3°N to 73.4°N) at around 400 km distance there is a strong northward flux in the reanalysis which prevails throughout the entire ARCGATE period. At 450 km distance, velocities are negative

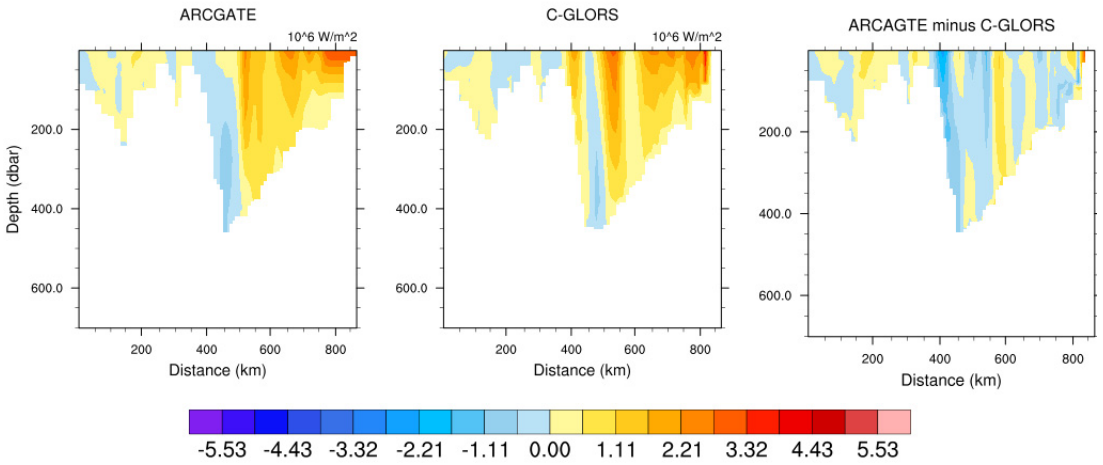

Figure 32: Barents Sea Opening heat flux cross sections averaged over July 2006 "to" December 2005.

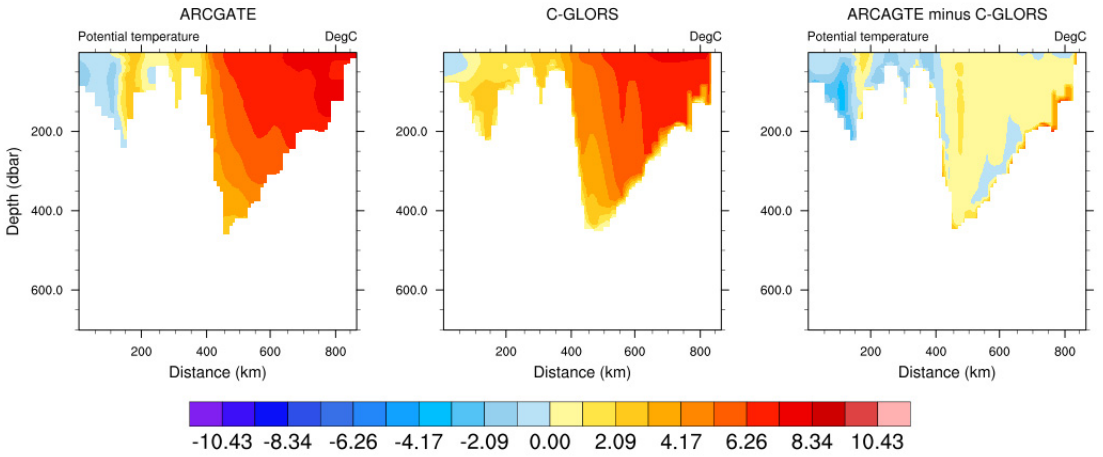

Figure 33: Barents Sea Opening potential temperature cross sections averaged over the ARCGATE period for ARCGATE and C-GLORS.

in the entire water column in the reanalysis in both periods. ARCGATE velocities between 400 and 450 km distance are variable throughout the year, with negative velocities between July and December and a weaker positive velocity structure between January and June. Averaged over the July to December period, the contribution from the BIC to the BSO volume transport is 0.33 ± 0.28 Sv from C-GLORS versus - 0.62 ± 0.56 Sv for ARCGATE. From January to June the volume flux through the BIC is 0.64 ± 0.25 Sv in C-GLORS and - 0.06 ± 0.55 Sv in ARCGATE. This results in an ARCGATE period average heat flux of - 7 ± 13 TW (AG) and 9 ± 5 TW (CG) in the BIC. The southern

	1) ARCGATE Period			RMSD		
	AG	**CG**	Pattern C.	**1)**	**2)**	**3)**
Heat (TW)	67 ± 35	91 ± 26	0.54 ± 0.19	31	40	20
Vol (Sv)	2.3 ± 1.2	3.6 ± 1.1	0.38 ± 0.17	1.5	2.0	0.9
T (°C)	4.5 ± 2.8 (0.5)	4.3 ± 2.3 (0.5)	0.90 ± 0.02	0.3	0.3	0.3
	2) Jan.-June			**3) July - Dec.**		
	AG	**CG**	Pattern C.	**AG**	**CG**	Pattern C.
Heat (TW)	48 ± 37	84 ± 30	0.42 ± 0.21	86 ± 21	97 ± 23	0.66 ± 0.06
Vol (Sv)	1.9 ± 1.5	3.8 ± 1.5	0.28 ± 0.18	2.7 ± 0.8	3.5 ± 0.8	0.49 ± 0.06
T (°C)	4.2 ± 2.8	3.9 ± 2.2	0.90 ± 0.01	4.9 ± 2.8	4.7 ± 2.4	0.90 ± 0.02
T var (°C)	(0.3)	(0.2)		(0.3)	(0.2)	

Table 5: Heat and volume fluxes through the Barents Sea Opening and cross-section average temperatures for 1) ARCGATE period, 2) Jan. - June and 3) July - Dec. See Tab. 3 for more detail on quantities and uncertainty ranges.

BSO (from 470 km to Norway) contributes 71 ± 31 TW (AG) and 81 ± 25 TW (CG) to the overall heat flux, leaving only roughly 3 TW (AG) and 1 TW (CG) of the total heat flux attributable to the part north of Bear Island (at approx. 350 km). It is not surprising that the ARCGATE cross sections show the expected volume flux export because one of the moorings is located exactly at the bottom of the BIC at 450 km (see Fig. ARCGATE mooring locations and Ch. 1.2). It is interesting that the reanalysis captures this negative transport at 450 km, but still has a prevalent positive transport further north at 400 km distance.

As already mentioned in Chapter 3.1, the contribution of transient eddies ($\overline{T'v'}$) to the total heat flux ($\overline{Tv}$) is small. Speaking in absolute values, the difference between the total heat flux and the stationary heat flux ($\bar{T}\bar{v}$) is largest in the BSO between January and March (see Fig. 17). Figure 35 shows total and stationary heat fluxes as well as the eddy contribution (the difference between the two) exemplary for the BSO averaged from January to March 2006. Please note the different scales with values being about one order of magnitude smaller for the eddy contribution than for the stationary and total heat fluxes. Averaged over this three month period, the "eddy" transport contributes 5 ± 0 TW to the total heat flux of 105 ± 0 TW, which is clearly dominated by stationary

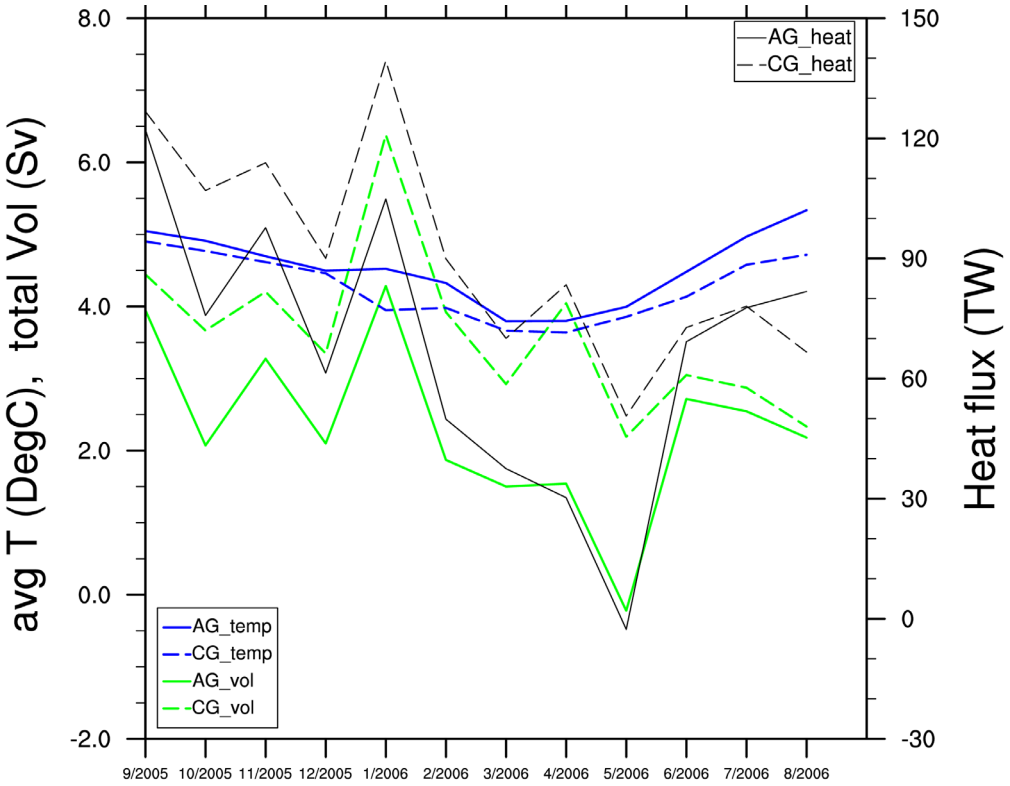

Figure 34: ARCGATE period averages of integrated volume (green) and heat (black) fluxes for the Barents Sea Opening for C-GLORS (dashed) and ARCGATE (solid). Cross-section averages of potential temperatures are shown in blue.

circulation patterns (100 $\pm$ 0 TW). Uncertainties are standard deviations from the three-month average.

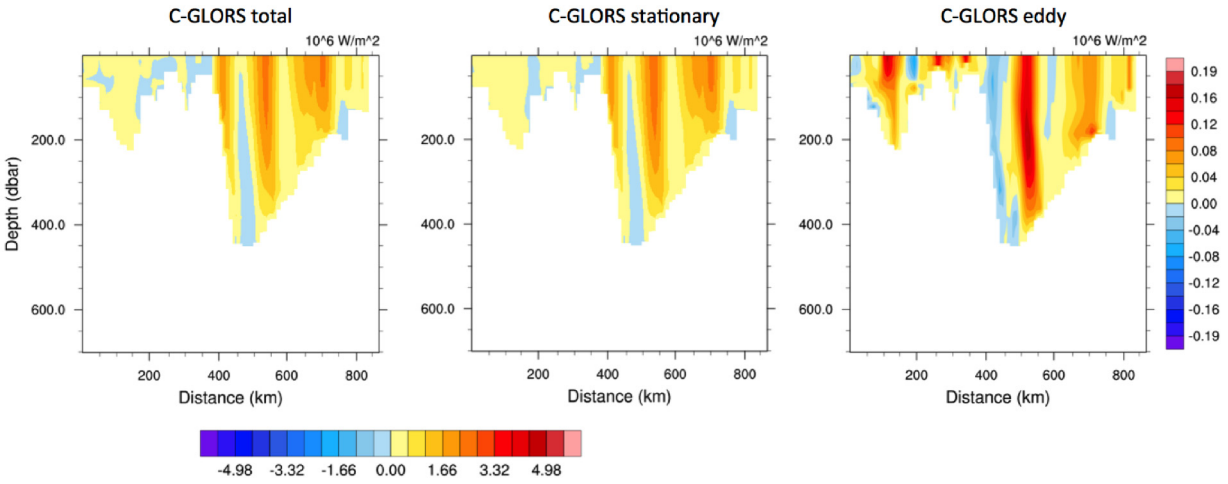

Figure 35: Total heat flux decomposed into contributions from stationary patters and transient eddies, averaged over the three month period from January to March 2006.

Årthun et al. (2012) use a regional coupled ice-ocean model HAMSOM (Hamburg Shelf Ocean Model, Schrum and Backhaus, 1999) in a configuration which has 7 km x 7 km horizontal resolution in the Barents Sea and 16 vertical levels (Årthun and Schrum, 2010) to estimate heat fluxes for the period 1998 - 2009. In a comparison between the seasonal cycle of the heat flux through the BSO obtained from their model and from in-situ observations Årthun et al. (2012) show that the model based heat fluxes are higher than the observation based estimates for all months except for May and June. Restricting model flux calculations to grid points in the locations of the moorings reduces the average heat flux and increases the agreement between the model and observation-based cycles (Årthun et al., 2012, Fig. 3). Similarly, the fact that the horizontal (and vertical) resolution of C-GLORS is higher than the spatial coverage of the moorings might partially explain the higher heat flux in the reanalysis compared to ARCGATE.

The ARCGATE estimates from this thesis are almost equal to Tsubouchi et al. (2016) who estimate 2.3 $\pm$ 1.2 Sv volume and 64 $\pm$ 33 TW temperature transport referenced to 0.0° C through the BSO during the ARCGATE period.

Bering Strait

Figures 37 and 38 show the cross section plots of average heat fluxes and temperatures for June 2006 "to" November 2005 and Figures 39 and 40 for December 2005 to May 2006. In this analysis the Bering Strait temperature and heat fluxes are investigated in two periods: December to May with predominantly negative temperatures and heat export versus June to November with positive temperatures and net heat import (see Fig. 34). Since the velocity distribution is similar for those two periods Figures 36 shows the ARCGATE period average velocities[24]. Distances are calculated towards 66.0 °N and 170.19 °W. Table 6 summarises the average heat and volume fluxes as well as cross-section averages of the temperatures for the two periods and for the entire ARCGATE period.

The ARCGATE period average velocity structure is similar in C-GLORS and ARCGATE but C-GLORS velocities are higher than ARCGATE velocities in all months. The

[24]The ARCGATE velocity plot has a lower vertical coverage than the temperature and heat flux plots. This is attributed to the fact that temperatures and velocities are not given in exactly the same points in the ARCGATE "grid" and that temperatures are interpolated to the velocity points. Thus, if there is a temperature value but no velocity value at a certain depth, this will affect the temperature and heat flux plots but not the velocity plots

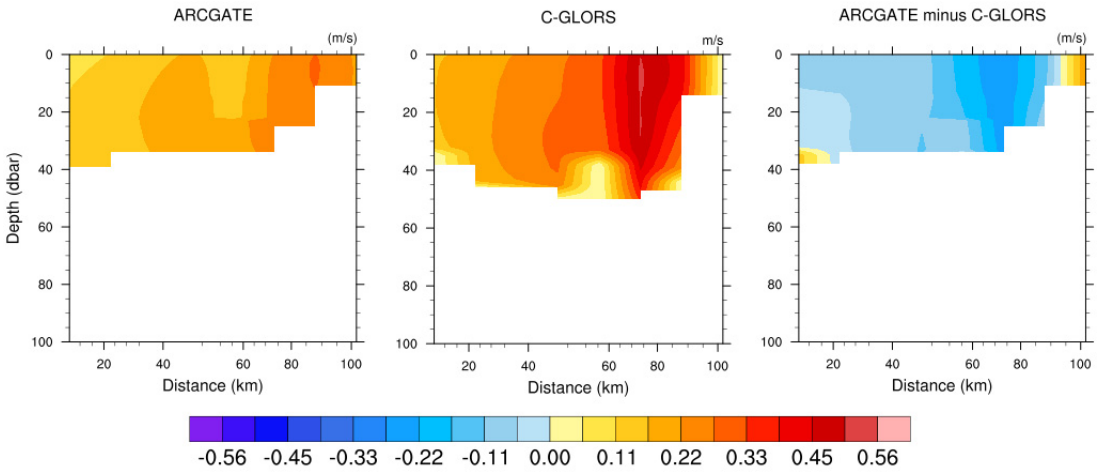

Figure 36: Bering Strait velocity cross sections averaged over the entire ARCGATE period for ARCGATE and C-GLORS.

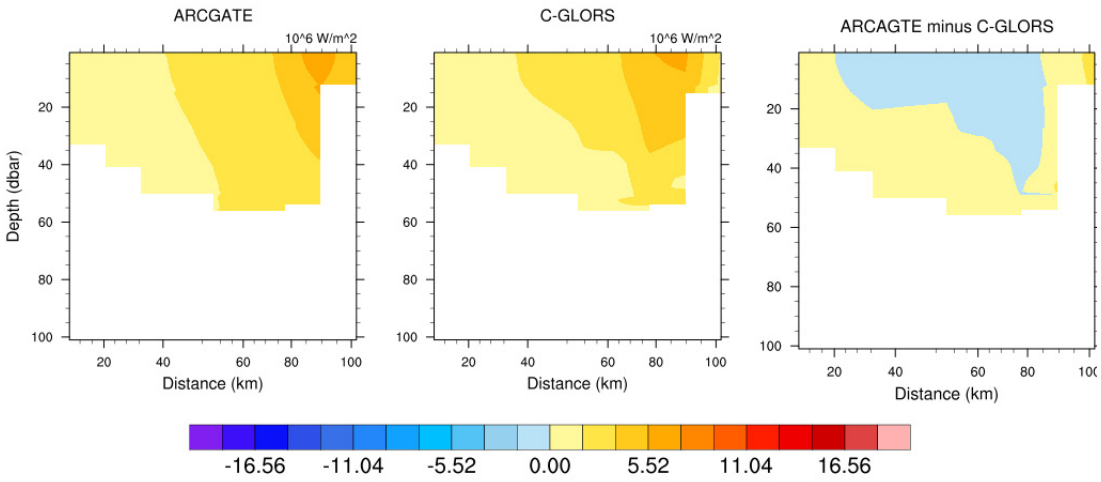

Figure 37: Bering Strait heat flux cross sections averaged over June 2006 “to“ November 2005 (Period 2).

C-GLORS cross section clearly shows strong northward transport on the eastern side of Bering Strait, a feature which is less obvious in the ARCGATE plot. Only during months of net volume export through Bering Strait (Nov. - Dec. for ARCGATE and only November for C-GLORS) the flow is dominated by southward transports on the western side of the strait. The overestimation of northward currents in C-GLORS may be explained by an underestimation of the influence of local winds - which drive southward flows - on the

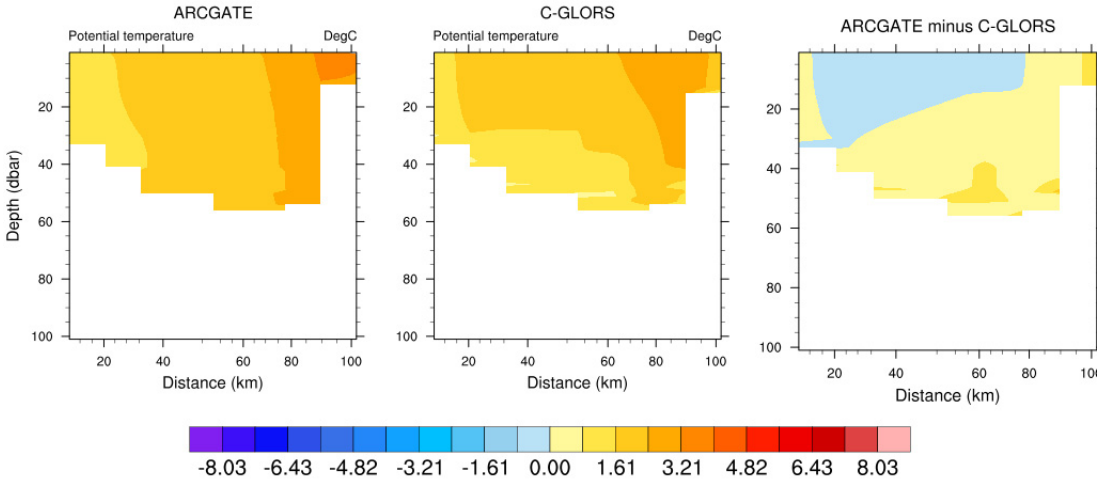

Figure 38: Bering Strait potential temperature cross sections averaged over period 2.

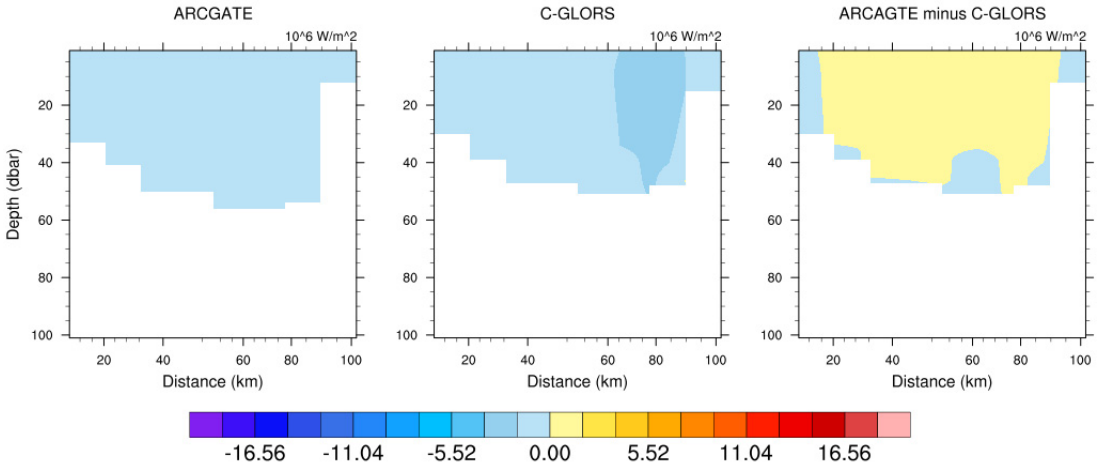

Figure 39: Bering Strait heat flux cross sections averaged over December 2005 to May 2006 (Period 3).

oceanic fluxes (see Ch. 1.2).

Looking at the ARCGATE heat fluxes in Fig. 41 the overall effect of Bering Strait transports from July to December is to heat the Arctic Ocean, mainly by importing warm water, but also by exporting cold water during December. From September 2005 to April 2006 the C-GLORS and ARCGATE heat fluxes are very similar, with the exception of December, when the C-GLORS volume flux is positive thus importing cold water while the ARCGATE volume flux is negative. Throughout most of the ARCGATE period, the volume and temperature discrepancies seem to balance each other, leading to a very good agreement between ARCGATE and C-GLORS heat fluxes. Towards the end of the

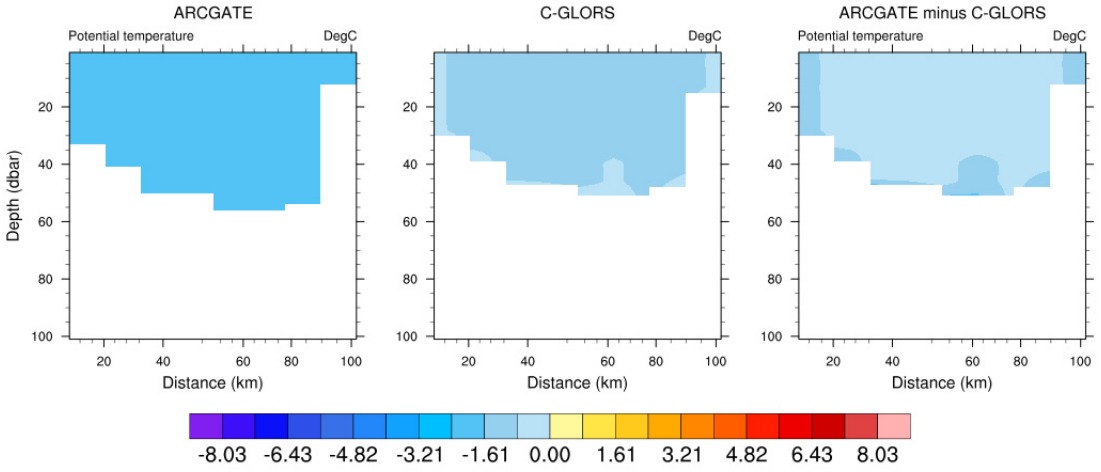

Figure 40: Bering Strait potential temperature cross sections averaged over period 3.

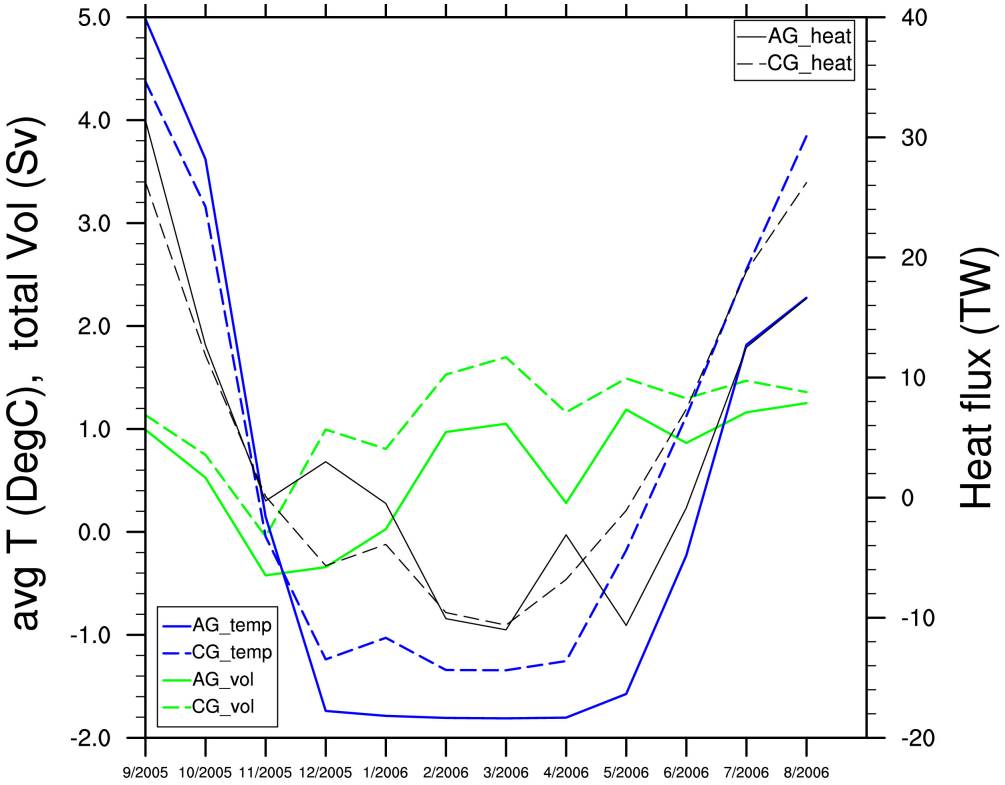

Figure 41: ARCGATE period averages of integrated volume (green) and heat (black) fluxes for Bering Strait for C-GLORS (dashed) and ARCGATE (solid). Cross-section averages of potential temperatures are shown in blue.

period (from May onward) the C-GLORS heat flux is greater than the ARCGATE flux since both velocity and temperature averages are positive and greater than those from ARCGATE.

	1) ARCGATE Period			RMSD		
	AG	**CG**	Pattern C.	**1)**	**2)**	**3)**
Heat (TW)	3 ± 13	4 ± 14	0.52 ± 0.20	6	6	6
Vol (Sv)	0.6 ± 0.6	1.1 ± 0.5	0.64 ± 0.09	0.6	0.3	0.8
T (°C)	0.2 ± 0.3 (2.4)	0.7 ± 0.5 (2.2)	0.44 ± 0.28	0.8	1.0	0.8
	2) Jun. - Nov.			**3) Dec. - May**		
	AG	**CG**	Pattern C.	**AG**	**CG**	Pattern C.
Heat (TW)	12 ± 12	15 ± 11	0.69 ± 0.09	- 5 ± 6	- 6 ± 4	0.36 ± 0.13
Vol (Sv)	0.7 ± 0.6	1.0 ± 0.6	0.69 ± 0.06	0.5 ± 0.6	1.3 ± 0.3	0.59 ± 0.09
T (°C)	2.1 ± 0.6	2.5 ± 1.2	0.64 ± 0.14	-1.75 ± 0.01	- 1.1 ± 0.3	- 0.08 ± 0.30
T var (°C)	(2.0)	(1.7)		(0.1)	(0.1)	

Table 6: Bering Strait heat and volume fluxes as well as cross-section averages of temperature are given for the averages over 1) ARCGATE period, 2) June - Nov. and 3) Dec. - May. See Tab. 3 for more detail on quantities and uncertainty ranges.

Figure 41 clearly shows that average temperatures are very variable in Bering Strait, with ARCGATE cross section averages ranging from - 1.81 ± 0.01 °C in March to + 5.0 ± 1.6 °C in September. C-GLORS temperatures are higher than ARCGATE averages for all months except for Sep. - Nov., but show a similar temporal variability. The C-GLORS minimum temperature is also reached in March (-1.3 ± 0.4 °C) and the maximum in September (4.4 ± 1.7 °C). The low anomaly pattern correlation for the heat flux in Period 3 can be explained by the low temperature pattern correlation which is even negative because ARCGATE temperatures are uniform (which is also reflected in the extremely low spatial standard deviation of only 0.02) while C-GLORS temperatures do show some spatial structure.

The one-year cycle of the average temperature in Bering Strait is qualitatively in line with the seasonal cycle presented by Woodgate and Aagaard (2005) albeit C-GLORS temperatures start to rise already after April while in ARCGATE and the literature, the increase begins after May. The spatial structure of temperature is represented well both in C-GLORS and ARCGATE, with warmer temperatures towards the east of the strait during Period 2 and well mixed temperaturs during Period 3 (Woodgate and Aagaard, 2005). There is no vertical stratification in the ARCGATE cross sections between June

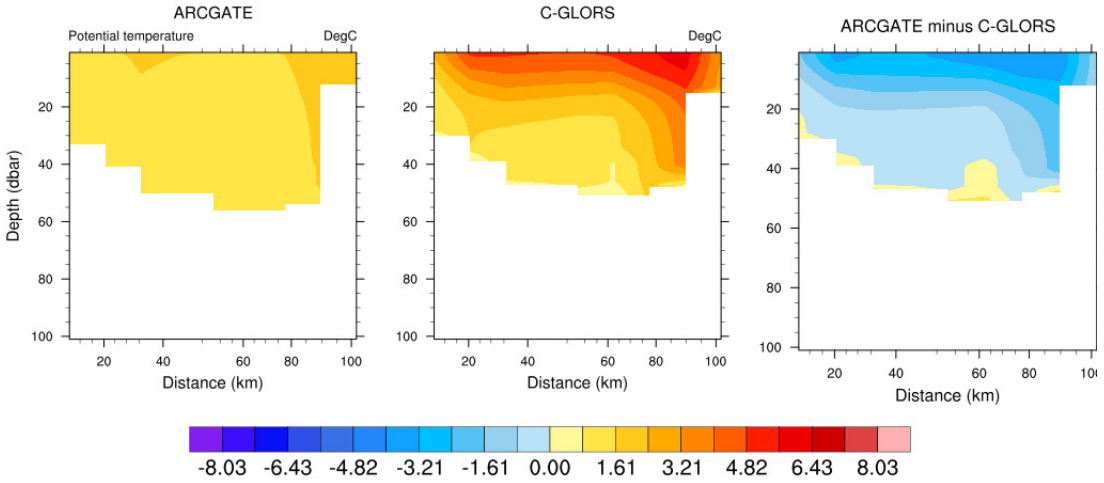

Figure 42: Bering Strait potential temperature cross sections averaged over June to August 2006.

and August, whereas the C-GLORS cross section shows a clear stratification in these months (see Fig. 42). As mentioned in Woodgate et al. (2010), near-bottom temperature measurements underestimate the average cross section temperature in summer due to the presence of a 10 - 20 m thick warm surface layer. Since there are no measurements in this layer in the ARCGATE mooring array, C-GLORS based summer temperature estimates in Bering Strait are likely more trustworthy than the observation based estimates.

The literature estimates of the ARCGATE volume flux through Bering Strait is 0.7 ± 0.7 Sv (Tsubouchi et al., 2016) which is in good agreement with the 0.6 ± 0.6 Sv estimate obtained from the cross sections.

4 Conclusion and Outlook

In the last chapter of this thesis the findings presented in Ch. 3 are synthesised to draw conclusions on the reliability of the C-GLORS Version 5 reanalysis in the framework of evaluating coupled Arctic mass, heat and freshwater budgets. Possibilities for further research on this subject are proposed *in italics*.

There is high confidence in the methods developed in this thesis first of all for choosing the correct points on the C-GLORS native grid and secondly for integrating along this irregular line to obtain the volume and heat flux timeseries. The methods were evaluated for one by comparing volume flux estimates obtained for each strait in this work with estimates for the same reanalysis product presented by Iovino et al. (2016) and Storto et al. (2016) (see Ch. 3.1). As discussed in Chapter 2.3.1, the fluxes derived from the velocity and temperature fields on the native grid and integrated along 70°N yield perfectly reasonable results. Therefore, these fields are prefered over the C-GLORS post-processed fields (both interpolated and on the native grid) which generate noisier timeseries and less accurate averages. Third, the cross section averages for each strait compare reasonably well (see Tab. 7), except for the ARCGATE volume transport in Fram Strait which has been explained above, to the timeseries averages so that it can be inferred that the cross-section plots in fact represent the appropriate fields.

The net volume flux averaged over the ARCGATE period from the C-GLORS reanalysis (- 0.05 ± 0.22 Sv) is in good agreement with the flux estimate based on the observations (- 0.14 ± 0.06 Sv). The net heat flux also compares reasonably well (131 ± 35 TW from C-GLORS versus 149 ± 43 TW from ARCGATE). However, based on the difference between ARCGATE and C-GLORS derived heat and volume fluxes, one may conclude that the reanalysis fields are not reliable enough for closing volume, heat and freshwater budgets in the Arctic region - at least not without incorporating those discrepancies into budget evaluations in the form of uncertainties in the oceanic flux terms. It should be pointed out that neither the observation-based estimates nor the reanalysis can be seen as "correct" since there are uncertainties in the measurement-derived fluxes as well, mainly due to uncertainties in the initial data but also due to temporal and spatial interpolations. The best option would be to *evaluate additional ocean reanalysis products (for example the upcoming ORAS5 or some of the products compared in the ORA-IP, see Ch. 1.4) using the methods developed in this work in order to estimate the robustness of*

Strait	Volume Flux (Sv)		Heat Flux (TW)	
	CG	**AG**	**CG**	**AG**
Davis 1)	- 3.9 ± 0.9	- 2.1 ± 0.7	5 ± 4	27 ± 10
Davis 2)	- 4.2 ± 1.0	- 2.2 ± 0.6	5 ± 5	31 ± 12
RMSD	0.3	0.2	2	4
Fram 1)	- 1.0 ± 1.1	- 1.1 ± 1.2	28 ± 10	56 ± 17
Fram 2)	- 1.0 ± 1.1	- 1.8 ± 1.2	26 ± 9	62 ± 19
RMSD	0.1	0.7	4	7
BSO 1)	3.7 ± 1.1	2.3 ± 1.2	95 ± 28	64 ± 33
BSO 2)	3.6 ± 1.1	2.3 ± 1.2	91 ± 26	67 ± 35
RMSD	0.1	0.0	5	4
Bering Strait 1)	1.2 ± 0.5	0.7 ± 0.7	4 ± 14	3 ± 10
Bering Strait 2)	1.1 ± 0.5	0.6 ± 0.6	4 ± 14	3 ± 13
RMSD	0.1	0.1	1	3
Net 1)	- 0.05 ± 0.22	- 0.14 ± 0.06	131 ± 35	149 ± 43
Net 2)	- 0.38 ± 0.31	- 1.06 ± 0.24	126 ± 32	163 ± 47
RMSD	0.39	1.0	8	15

Table 7: ARCGATE period average volume and heat fluxes for each strait 1) from the timeseries (integrated along the irregular line for C-GLORS and summed over all ARCGATE points in each strait) and 2) from the sums across the fields used for the cross section plots. RMSDs between 1) and 2) for C-GLORS and ARCGATE are given as well. This table is merely a compilation of the values already presented in the tables in Chapters 3.1 and 3.2 with exception of the cross-section derived net fluxes and the RMSDs. Uncertainties of the averages are temporal standard deviations of monthly values from the ARCGATE period average.

ocean flux estimates and to quantify uncertainties for oceanic budget terms.

Due to the cross section plots, areas of discrepancy could be identified, finding disagreements in the velocity patterns especially in Davis and **Fram Strait**: Velocities in the WSC and the EGC are both too small in C-GLORS compared to ARCGATE and the literature, but concerning the net flux those discrepancies partly balance each other, since velocities are positive in the WSC while they are negative in the EGC. Over Belgica

Bank, C-GLORS currents are northward almost everywhere whereas ARCGATE currents go southward in the majority of the shelf region except for the westernmost part where velocities are strongly northward. Again, the differences in those two areas partly compensate each other, so that the net volume transport obtained from the timeseries (Ch. 3.1) is very similar in C-GLORS and ARCGATE. Heat fluxes on the other hand are affected by those discrepancies due to the correlation with temperature. The temperature patterns are similar in C-GLORS and ARCGATE although C-GLORS temperatures are less extreme (both too cold in positive temperature areas and too warm in cold regions). Nonetheless, because the ARCGATE heat flux in the WSC (roughly 80 TW) is more than twice the C-GLORS heat flux (roughly 30 TW) and the heat flux contributions (both negative and positive) are much smaller in the other parts of Fram Strait (ranging from approx. - 4 TW to 2 TW), the resulting net heat flux in ARCGATE (56 TW) is twice that from C-GLORS (28 TW).

Davis Strait volume export is larger in C-GLORS than in ARCGATE, which is attributable both to too weak northward currents on the WGS and along the slope and negative transports in winter in the reanalysis, contrasting the continuous northward transport in ARCGATE all year in this region. Combined with the temperature distribution (which overall is quite similar in C-GLORS and ARCGATE), this leads to a positive heat flux in ARCGATE and a negative heat flux in C-GLORS during winter. Additionally, strong negative volume fluxes year-round are detected at 200 km distance (57°W), a feature which is much less pronounced in the winter period in ARCGATE and velocities are even positive here during summer. Together with the temperature distribution, this results in heat export during winter in C-GLORS in this area, opposed to heat import all year in ARCGATE in the same region. Those two discrepancies in the heat and velocity patterns and strengths are not compensated elsewhere in Davis Strait so that the overall heat flux is roughly six times greater in ARCGATE than in C-GLORS (27 TW vs. 5 TW, respectively) and the volume export in C-GLORS is roughly double the ARCGATE export (approx. - 4 Sv vs - 2 Sv).

Heat transports through the **Barents Sea Opening** are overestimated for almost all months in the reanalysis compared to ARCGATE. This difference is mainly attributable to an overestimation of volume fluxes and to temperatures being positive year round in most of the BSO. Temperature distributions and extremes are very similar in both datasets at

least south of Bear Island (at around 350 km distance in the plots). Velocity patterns are also similar, although Arctic inflow is generally stronger in C-GLORS than ARCGATE. The region of greatest discrepancy is the BIC between 360 and 470 km distance. Here, the volume transport is predominantly positive (especially until 450 km distance) all year in the reanalysis, in contrast to negative transports in the entire water column in ARCGATE between July and December and negative transports in the lower 200 m from January to June. The ARCGATE fluxes are therefore in accordance with the literature, stating that there is an average volume export in the BIC of about 1.2 Sv. Positive C-GLORS velocities versus negative ARCGATE currents result in approximately 0.8 Sv difference between the two in the BIC for the ARCGATE period. 16 TW of the overall 24 TW heat flux discrepancy (C-GLORS minus ARCGATE) are attributable to this region. The southern BSO contributes 10 TW difference and the part north of Bear Island - 2 TW.

Last but not least the agreement between C-GLORS and ARCGATE volume fluxes through **Bering Strait** is quite good and even better for the heat fluxes concerning both pattern distribution and variability throughout the year. Volume transports are overestimated all year by the reanalysis compared to ARCGATE, possibly due to an underrepresentation of the influence of local winds (driving the flow southward on an annual-mean basis) on oceanic transports in this strait. On the other hand, temperatures are lower in ARCGATE than in C-GLORS between December and August, possibly due to the absence of measurements in the warm ocean-surface layer. Stratification is clearly visible from June to August in C-GLORS but not in ARCGATE which supports the above hypothesis. ARCGATE temperatures are therefore likely underestimated compared to the true state, while C-GLORS velocities are overestimated. However, slightly more negative C-GLORS heat fluxes between December and May balance the overestimation of the heat flux from June to November, so that on an annual basis the heat flux estimates are very similar (3 and 4 TW from ARCGATE and C-GLORS, respectively).

In conclusion, the C-GLORS reanalysis yields quite good overall results, especially concerning the pattern distribution of temperature, velocity and heat fluxes. Nonetheless, some regions with clear differences between the C-GLORS and ARCGATE cross-section plots have been identified in this work which explain most of the discrepancy found in the annual averages and the time series. *There is definitely still room for interpretation of the results and finding explanations to where discrepancies between the two datasets*

originate from, possibly based on a more thorough understanding of the model physics and assimilation scheme employed in C-GLORS.

Besides using several different reanalysis products to evaluate the uncertainty in oceanic volume, heat and freshwater budget terms, *the study period can be prolonged from the 09/2005 - 08/2006 period (termed the "ARCGATE period" in this work) to the full 2004 to 2010 period once the data become available from the ARCGATE project. This thesis can therefore be seen as a pilot study which provides the foundation for this more comprehensive comparison.* As a small "peek into the future", Figures 43 and 44 show the volume and heat transports through each gateway calculated from C-GLORS for this seven-year period (dashed) and the ARCGATE fluxes for the ARCGATE period (solid).

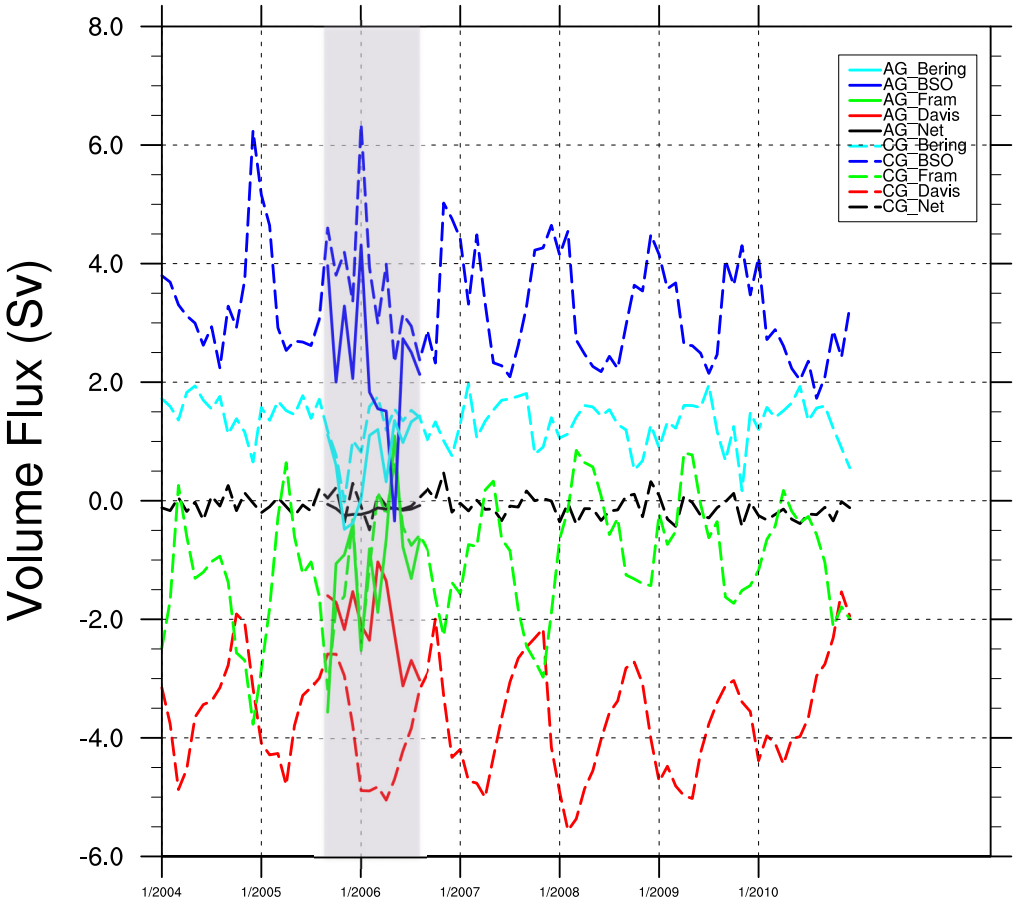

Figure 43: Volume Flux in Sv through Davis, Fram, Bering Strait, the BSO and net flux into the Arctic for C-GLORS between 2004 and 2010 (dashed line) and ARCGATE for the ARCGATE period (solid line).

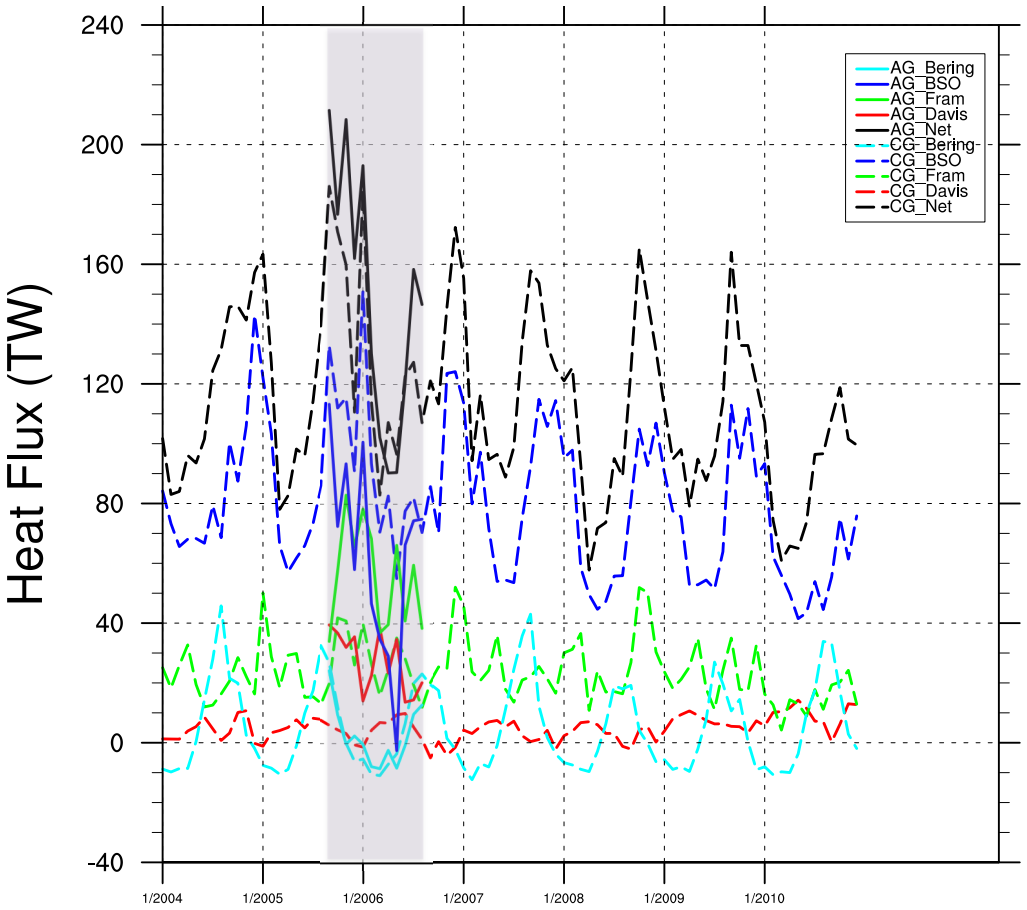

Figure 44: Heat Flux in TW through Davis, Fram, Bering Strait, the BSO and net flux into the Arctic for C-GLORS (2004 - 2010, dashed line) and ARCGATE (ARCGATE period, solid line).

Acknowledgements

My gratitude is due to Prof. Leopold Haimberger and Dr. Michael Mayer who provided their scientific expertise in numerous discussions and guided me towards interesting investigations throughout this thesis. I appreciate being given the opportunity to work in such a supportive environment, an experience which has certainly contributed to my motivation to continue my scientific path with a PhD. On a personal level I am truly thankful for my partner Stefan, who always manages to cheer me up when I encounter a problem, be it an academic or personal challenge, and who enriches my life in so many different ways. Special mention is also due of my friend Sabine who is always a pleasure to be around and is there when I need her with helpful advice, and also of my friends whom I have known since high-school. I am more than grateful to have such a wonderful sister who lightens my mood whenever we see each other and to my parents who are always there for me.

References

Årthun, M., Eldevik, T., Smedsrud, L. H., Skagseth, Ø., and Ingvaldsen, R. B. (2012). Quantifying the Influence of Atlantic Heat on Barents Sea Ice Variability and Retreat. *J. Climate*, 25:4736 – 4743. doi: 10.1175/JCLI-D-11-00466.1.

Årthun, M. and Schrum, C. (2010). Ocean surface heat flux variability in the Barents Sea. *J. Mar. Syst.*, 83:88 – 98. doi: 10.1016/j.jmarsys.2010.07.003.

AWI (2016). Maximizing the potential of Arctic Ocean Gateway array. `https://www.awi.de/en/science/climate-sciences/physical-oceanography/projects/arcgate.html`. Accessed on: 29 August 2016.

Bacon, S., Aksenov, Y., Fawcett, S., and Madec, G. (2015). Arctic mass, freshwater and heat fluxes: methods and modelled seasonal variability. *Phil. Trans. R. Soc. A*, 373. `http://dx.doi.org/10.1098/rsta.2014.0169`.

Balmaseda, M. A. and coauthors (2014). The Ocean Reaalysis Intercomparison Project ORA–IP. `https://www.researchgate.net/publication/266374001_The_Ocean_Reanalyses_Intercomparison_Project_ORA-IP`. Accessed on: 1 November 2016.

Balmaseda, M. A., Mogensen, K., and Weaver, A. T. (2013). Evaluation of the ECMWF ocean reanalysis system ORAS4. *Q. J. R. Meteorol. Soc.*, 139:1132–1161. doi: 10.1002/qj.2063.

Barnier, B., Madec, G., Penduff, T., Molines, J., Treguier, A., Le Sommer, J., Beckmann, A., Biastoch, A., Böning, C., Dengg, J., Derval, C., Durand, E., Gulev, S., Remy, E., Talandier, C., Theetten, S., Maltrud, M., McClean, J., and De Cuevas, B. (2006). Impact of partial steps and momentum advection schemes in a global ocean circulation model at eddy permitting resolution. *Ocean dynamics*, 56:543–567. http://dx.doi.org/10.1007/s10236-006-0082-1.

Beszczynska-Möller, A., Fahrbach, E., Schauer, U., and Hansen, E. (2012). Variability in Atlantic water temperature and transport at the entrance to the Arctic Ocean, 1997–2010. *ICES J. Mar. Sci.*, 69:852–863. doi: 10.1093/icesjms/fss056.

Beszczynska-Möller, A., Woodgate, R. A., Lee, C., Melling, H., and Karcher, M. (2011). A synthesis of exchanges through the main oceanic gateways to the Arctic Ocean. *Oceanography*, 24:82–99. http://dx.doi.org/10.5670/oceanog.2011.59.

Blindheim, J. (1989). Cascading of Barents Sea bottom water into the Norwegian Sea. *Rapp. P.-v. Réun. Cons. int. Explor. Mer.*, 188:49 – 58. doi: 10.1126/science.1122593.

Bouillon, S., Morales Maqueda, M. A., Legat, V., and Fichefet, T. (2009). An elastic-viscous-plastic sea ice model formulated on Arakawa B and C grids. *Oc. Mod.*, 27:174 – 184. doi: 10.1016/j.ocemod.2009.01.004.

Boyin, H., Xue, Y., Zhang, D., Kumar, A., and McPhaden, M. J. (2010). The NCEP GODAS ocean analysis of the tropical pacific mixed layer heat budget on seasonal to interannual time scales. *J. Climate*, 23:4901–1925. doi: 10.1175/2010JCLI3373.1.

Businger, J. A. (2014). The Fluxes of Specific Enthalpy, Sensible Heat and Latent Heat near the Earth's Surface. *J. Atmosph. Sci.*, 39:1889 – 1892. doi: 10.1175/1520-0469(1982)039<1889:TFOSES>2.0.CO;2.

Collins, S. N., James, R. S., Ray, P., Chen, K., Lassman, A., and Brownlee, J. (2013). Grids in Numerical Weather and Climate Models, Climate Change and Regional/Local Responses. `http://www.intechopen.com/books/climate-change-and-regional-local-responses/grids-in-numerical-weather-and-climate-models`. Dr Pallav Ray (Ed.), InTech. doi: 10.5772/55922. Accessed on: 28 September 2016.

Comiso, J. C., Parkinson, C. L., Gersten, R., and Stock, L. (2008). Accelerated decline in the Arctic sea ice cover. *Geophys. Res. Lett.*, 35:L01703. doi: 10.1029/2007GL031972.

Curry, B., Lee, M. C., and Petrie, B. (2011). Volume, Freshwater, and Heat Fluxes through Davis Strait, 2004–05. *J. Phys. Oc.*, 41:429 – 436. doi: 10.1175/2010JPO4536.1.

Curry, R. and Mauritzen, C. (2005). Dilution of the northern North Atlantic Ocean in recent decades. *Science*, 208:1772 – 1774.

de Steur, L., Hansen, E., Mauritzen, C., Beszczynska-Möller, A., and Fahrbach, E. (2014). Impact of recirculation on the East Greenland Current in Fram Strait: Results from

moored current meter measurements between 1997 and 2009. *Deep-Sea Res. I*, 92:26 – 40. doi: 10.1016/j.jmarsys.2010.07.003.

Dee, D. and coauthors (2011). The ERA Interim reanalysis: Configuration and performance of the data assimilation system. *Q. J. R. Meteorol. Soc.*, 137.656:553–597.

Dickson, R. R. (2007). The integrated Arctic Ocean Observing System (iAOOS) in 2007. `https://www.arcus.org/files/page/documents/19695/iaoos_document.pdf`. Accessed on: 11 October 2016.

ECMWF (2016a). ERA-CLIM2: Ongoing research project 2014–2017. `http://www.ecmwf.int/en/research/projects/era-clim2`. Accessed on: 14 September 2016.

ECMWF (2016b). Ocean Reanalysis. `https://reanalyses.org/ocean/overview-current-reanalyses`. Accessed on: 28 September 2016.

Fahrbach, E., Meincke, J., Østerhus, S., Rohardt, G., Schauer, U., Tverberg, V., and Verduin, J. (2001). Direct measurements of volume transports through Fram Strait. *Polar Res.*, 20:217 – 224.

Fichefet, T. and Morales Maqueda, M. A. (1997). Sensitivity of a global sea ice model to the treatment of ice thermodynamics and dynamics. *J. Geophys. Res.*, 102:609 – 646. doi: 10.1029/97JC00480.

Fieg, K., Gerdes, R., Fahrbach, E., Beszczynska-Möller, A., and Schauer, U. (2010). Simulation of oceanic volume tranports through Fram Strait 1995–2005. *Ocean Dyn.*, 60:491–502. doi: 10.1007/s10236-010-0263-9.

Forget, G., Campin, J., Heimbach, P., Hill, C. N., Ponte, R. M., and Wunsch, C. (2016). ECCO Version 4: Second Release. `http://hdl.handle.net/1721.1/102062`.

Good, S. A., Martin, M. J., and Ryner, N. A. (2013). EN4: quality controlled ocean temperature and salinity profiles and monthly objective analyses with uncertainty estimates. *J. Geophys. Res.:Oceans*, 118:6704 – 6716. doi: 10.1002/2013JC009067.

Haimberger, L. (2015). Variability of change of arctic energy and freshwater budgets. Research Proposal to FWF Vienna.

Ingleby, B. and Huddleston, M. (2007). Quality control of ocean temperature and salinity profiles – historical and real-time data. *J. Mar. Syst.*, 65:158–175. 10.1016/j.jmarsys.2005.11.019.

Iovino, D., Masina, S., Storto, A., and Haid, V. (2016). The CMCC ocean reanalysis in polar regions. Presentation slides.

Kalnay, E., Kanamitsu, M., Kistler, R., Collins, W., Deaven, D., Gandin, L., Iredell, M., Saha, S., White, G., Woollen, J., Zhu, Y., Chelliah, M., Ebisuzaki, W., Higgins, W., Janowiak, J., Mo, K. C., Ropelewski, C., Wang, J., Leetmaa, A., Reynolds, R., Jenne, R., and Joseph, D. (1996). The NCEP/NCAR 40-year Reanalysis Project. *Bulletin of the American Meteorological Society*, 77(3):437–471. `http://dx.doi.org/10.1175/1520-0477(1996)077<0437:TNYRP>2.0.CO;2`.

Kobayashi, S., Ota, Y., Harada, Y., Ebita, A., Moriya, M., Onoda, H., Onogi, K., Kamahori, H., Kobayashi, C., Endo, H., Miyakoda, K., and Takahashi, K. (2015). The JRA-55 reanalysis: General specifications and basic characteristics. *J. Meteorol. Soc. of Japan*, 94:5–48. 10.2151/jmsj.2015-001.

Köhl, A. and Stammer, D. (2008). Variability of the Meridional Overturning in the North Atlantic from the 50 years GECCO State Estimation. *J. Phys. Oc.*, 38:1913–1930.

Kundu, P., Cohen, I. M., and Dowling, D. R. (2012). *Fluid Mechanics*. Waltham: Elsevier, Inc. ISBN 978-0-12-382100-3, fifth edition.

Kwok, R. (2009). Outflow of Arctic Ocean Sea Ice into the Greenland and Barents Seas: 1979–2007. *J. Climate*, 22:2438 – 2457. doi: 10.1175/2008JCLI2819.1.

Kwok, R. and Rothrock, D. A. (2009). Decline in Arctic sea ice thickness from submarine and icesat records: 1958–2008. *Geophys. Res. Lett.*, 36:L15501. doi: 10.1029/2009GL039035.

Laloyaux, P., Balmaseda, M., Dee, D., Mogensen, K., and Janssen, P. (2016). A coupled data assimilation system for climate reanalysis. *Q. J. R. Meteorol. Soc.*, 142:65–78. doi: 10.1002/qj.2629.

Laloyaux, P., de Boisseson, E., Balmaseda, M. A., Dee, D. P., Janssen, P., Mogensen, K., and Thepaut, J. (2014). The Coupled Earth Reanalysis system (CERA). Accessed on: 11 November 2016.

Madec, G. (2016). *NEMO Ocean Engine Handbook*. Institut Pierre-Simon Laplace (IPSL), France, 3.6 (stable) edition.

Madec, G. and Imbard, M. (1996). A global ocean mesh to overcome the North Pole singularity. *Climate Dynamics*, 12:381–388.

Masina, S., Di Pierluigi, P., Storto, A., and Navarra, A. (2011). Global ocean re-analyses for climate applications. *Dynamics of Atmospheres and Oceans*, 52:341–366. doi: 10.1016/j.dynatmoce.2011.03.006.

Mayer, M. and Haimberger, L. (2012). Poleward Atmospheric Energy Transports and Their Variability as Evaluated from ECMWF Reanalysis Data. *J. Climate*, 25(2):734–752.

Mayer, M., Haimberger, L., and Balmaseda, M. (2014). On the energy exchange between tropical ocean basins related to ENSO. *J. Climate*, 27:6393–6403. http://dx.doi.org/10.1175/JCLI-D-12-00681.1.

Mayer, M., Haimberger, L., Pietschnig, M., and Storto, A. (2016). Facets of Arctic energy accumulation based on observations 2000–2015. *Geophys. Res. Letters*, 43:10,420 – 10,429. doi: 10.1002/2016GL070557.

Murray, R. J. (1996). Explicit Generation of Orthogonal Grids for Ocean Models. *Journal of Computational Physics*, 126:251–273.

NAS (2005). The International Geophysical Year. `http://www.nas.edu/history/igy/`. National Academy of Sciences. Accessed on: 11 October 2016.

NSIDC (2016). National Snow & Ice Data Center: State of the Cryosphere. `https://nsidc.org/cryosphere/sotc/sea_ice.html`. Accessed on: 28 October 2016.

Parkinson, C. L. and Comiso, J. C. (2013). On the 2012 record low Arctic sea ice cover: Combined impact of preconditioning and an August storm. *Geophys. Res. Lett.*, 40(7):1356–1361. doi: 10.1002/grl.50349.

Peixoto, J. P. and Oort, A. H. (1992). *Physics of Climate*. New York: American Institute of Physics. ISBN 0-88318-712-4.

Peterson, B. J., McClelland, J., Curry, R., Holmes, R. M., Walsh, J. E., and Aagaard, K. (2006). Trajectory shifts in the Arctic and subarctic freshwater cycle. *Science*, 313:1061 – 1066. doi: 10.1126/science.1122593.

PHC (2005). University of Washington Polar Science Center Hydrographic Climatology. `http://psc.apl.washington.edu/Climatology.html`. Accessed on: 23 September 2016.

Rayner, D., Hirschi, J. J., Kanzow, T., Johns, W. E., Wrights, P. G., Frajka–Williams, E., Bryden, H. L., Meinen, C. S., Brainger, M. O., Marotzke, J., Beal, L. M., and Cunningham, A. (2011). Monitoring the Atlantic meridional overturning circulation. *Deep Sea Res., Part II*, 58:1744 – 1753. doi: 10.1016/j.dsr2.2010.10.056.

Rhein, M., Rintoul, S. R., Aoki, S., Campos, E., Chambers, D., Feely, R. A., Gulev, S., Johnson, G. C., Josey, S. A., Kostianoy, A., Mauritzen, C., Roemmich, D., Talley, L. D., and Wang, F. (2013). *Observations: Ocean. In: Climate Change 2013: The Physical Science Basis. Contribution of Working Group I to the Fifth Assessment Report of the Intergovernmental Panel on Climate Change. [Stocker, T.F., D. Qin, G.-K. Plattner, M. Tignor, S.K. Allen, J. Boschung, A. Nauels, Y. Xia, V. Bex and P.M. Midgley (eds.)].* Cambridge University Press, Cambridge, United Kingdom and New York, NY, USA.

Schauer, U. and Beszczynska–Möller (2009). Problems with estimation and interpretation of oceanic heat transport: Conceptual remarks for the case of Fram Strait in the Arctic Ocean. *Ocean Sci.*, 5:487–494. http://dx.doi.org/10.5194/os-5-487-2009.

Schauer, U., Beszczynska–Möller, A., Walczowski, W., Fahrbach, E., Piechura, J., and Hansen, E. (2008). Variation of measured heat flow through the Fram Strait between 1997 and 2006. in: Arctic-subarctic ocean fluxes. r.r. dickson, j. meincke, and p. rhines, eds. Springer, Dodrecht.

Schrum, C. and Backhaus, J. O. (1999). Sensitivity of atmosphere–ocean heat exchange and heat content in the North Sea and the Baltic Sea. *Tellus*, 51:526 – 549. doi: 10.1034/j.1600-0870.1992.00006.x.

Serreze, M. C., Barrett, A. P., Slater, A. G., Steele, M., Zhang, J., and Trenberth, K. (2007). The large-scale energy budget of the Arctic. *J. Geophys. Res.*, 112. D11122. doi: 10.1029/2006JD008230.

Serreze, M. C., Barrett, A. P., Slater, A. G., Woodgate, R. A., Aagaard, K., Lammers, R. B., Steele, M., Moritz, R., Meredith, M., and Lee, C. M. (2006). The large-scale freshwater cycle of the Arctic. *J. Geophys. Res.*, 111. C11010. doi: 10.1029/2005JC003424.

Serreze, M. C., Barrett, A. P., Stroeve, J. C., Kindig, D. N., and Holland, M. M. (2009). The emergence of surface-based arctic amplification. *The Cryosphere*, 3(1):11–19. doi: 10.5194/tc-3-11-2009.

Serreze, M. C. and Barry, R. G. (2014). *The Arctic Climate System*. Cambridge: Cambridge University Press. Cambridge Atmospheric and Space Science Series. ISBN 978-1-107-03717-5, second edition.

Skagseth, Ø. (2008). Recirculation of Atlantic Water in the western Barents Sea. *Geophys. Res. Lett.*, 35. doi: 10.1029/2008GL033785.

Smedsrud, L. H., Ingvaldsen, R., Nilsen, J. E. Ø., and Skagseth, Ø. (2010). Heat in the Barents Sea: Transport, storage and surface fluxes. *Ocean Sci.*, 6:219–234. doi: 10.5194/os-6-219-2010.

Storto, A. and Masina, S. (2016a). C-GLORSv5: an improved multi-purpose global ocean eddy-permitting physical reanalysis. *Earth System Science Data Discussions*, 2016:1–29.

Storto, A. and Masina, S. (2016b). The CMCC Eddy-permitting Global Ocean Physical Reanalysis (C-GLORS v5, 1980–2014). Bologna, Italy: Centro Euro-Mediterraneo sui Cambiamenti Climatici. doi: 10.1594/PANGAEA.857995.

Storto, A., Masina, S., and A., N. (2016). Evaluation of the CMCC eddy-permitting global ocean physical reanalysis system (C-GLORS, 1982–2012) and its assimilation components. *Q. J. R. Meteorol. Soc.*, 142:738–758. doi: 10.1002/qj.2673.

Stroeve, J. C., Kattsov, V., Barrett, A., Serreze, M., Pavlova, T., Holland, M., and Meier, W. N. (2012). Trends in Arctic sea ice extent from CMIP5, CMIP3 and observations. *Geophys. Res. Lett.*, 39:L16502. doi: 10.1029/2012GL052676.

Trenberth, K. E. (1997). Using Atmospheric Budgets as a Constraint on Surface Fluxes. *J. Climate*, 10:2796–2809.

Trenberth, K. E. and Fasullo, J. T. (2008). An Observational Estimate of Inferred Ocean Energy Divergence. *J. Phys. Oceanogr.*, 38:984–999. doi: 10.1175/2007JPO3833.1.

Tsubouchi, T. (2014). ARCGATE: Maximizing the potential of Arctic Ocean Gateway array. Project proposal MARIE SKLODOWSKA-CURIE ACTIONS Individual Fellowships (IF) Call: H2020-MSCA-IF-2014.

Tsubouchi, T., Bacon, S., Naveira Garabato, A., Aksenov, Y., ASchauer, U., Beszczynska-Möller, A., Hansen, E., de Steur, L., Lee, C., Curry, B., and Ingvaldsen, R. (2016). The Arctic Ocean seasonal cycle: an observation-based inverse estimate. *To be submitted to JGR-Ocean*.

Tsubouchi, T., Bacon, S., Naveira Garabato, A., Aksenov, Y., Laxon, S., Fahrbach, E., Beszczynska-Möller, A., Hansen, E., Lee, C., and Ingvaldsen, R. (2012). The arctic ocean in summer: A quasi-synoptic inverse estimate of boundary fluxes and water mass transformation. *J. of Geophys. Res.*, 117. doi: 10.1029/2011JC007174.

Uppala, S. M. and coauthors (2005). The ERA–40 Re–Analysis. *Q. J. R. Meteorol. Soc.*, 131:2961 – 3012.

Uttal, T. and coauthors (2016). International Arctic Systems for observing the atmosphere: An International Polar Yar legacy consortium. *Bull. Amer. Meteor. Soc.*, 97:1033 – 1056. doi: 10.1175/BAMS-D-14-00145.1.

Valdivieso, M., Haines, K., Zuo, H., and Lea, D. (2014). Freshwater and heat transports from global ocean synthesis. *J. Geophys. Res.*, 119:394 – 409. doi:10.1002/2013JC009357.

Vinje, T., Nordlund, N., and Kvarnbekk, A. (1998). Monitoring ice thickness in Fram Strait. *J. Geophys. Res.*, 103. doi: 10.1029/97JC03360.

Wadley, R. and Bigg, G. R. (2002). Impact of flow through the Canadian Archipelago and Bering Strait on the North Atlantic and Arctic circulation: An ocean modelling study. *Q. J. R. Meteorol. Soc.*, 128(585):2187–2203. doi: 10.1256/qj.00.35.

Wentz, F. J., Hilburn, K. A., and Smith, D. K. (2012). Remote Sensing System DMSP SSMIS Environmental Suite on 0.25 deg grid, Version 7. Remote Sensing Systems, Santa Rosa, CA. Available online at www.remss.com/missions/ssmi. Accessed on 12 Nov. 2016.

Wielicki, B. A., Barkstrom, B. R., Harrison, E. F., Lee, R. B., Smith, G. L., and Cooper, J. E. (1996). Clouds and the Earth's Radiant Energy System (CERES): An Earth observing system experiment. *Bull. Amer. Meteor. Soc.*, 77:853–868.

Wood, K. R. and Overland, J. E. (2016). The First International Polar Year. `http://www.pmel.noaa.gov/arctic-zone/ipy-1/Data-P1.htm`. Accessed on: 11 October 2016.

Woodgate, R. A. and Aagaard, K. (2005). The temperature, salinity, and transport variability of the Bering Strait through flow. *Geophys. Res. Letters*, 32. doi: 10.1029/2004GL021880.

Woodgate, R. A., Aagaard, K., and Weingartner, T. J. (2005). A year in the physical oceanography of Chukchi Sea: Moored measurements from autumn 1990–1991. *Deep Sea Res., Part II*, 52:3116 – 3149. doi: 10.1016/j.dsr2.2005.10.016.

Woodgate, R. A., Weingartner, T., and Lindsay, R. (2010). The 2007 Bering Strait oceanic heat flux and anomalous Arctic sea-ice retreat. *Geophys. Res. Letters*, 37. doi: 10.1029/2009GL041621.

Zhang, J. and Rothrock, D. A. (2003). Modeling global sea ice with a thickness and enthalpy distribution model in generalized curvilinear coordinates. *Mon. Weather Rev.*, 131:681–697.

Zuo, H., Valdivieso, M., Lea, D., and Haines, K. (2013). Numerical data from the Global Ocean Physics Reanalysis UR025.4 (1989–2010) as part of the VALue of the RAPID–WATCH Climate Change programme array (VALOR) project. NCAS British Atmospheric Data Centre. doi: 10.5285/4bcfa3a4-c7ec-4414-863d-caeceb21f16f.